Search for Charginos Nearly Mass-Degenerate with the Lightest Neutralino Based on a Disappearing-Track Signature in pp Collisions at $\sqrt{s} = 8$ TeV

Ph. D. thesis

Shingo Kazama

Department of Physics
Faculty of Science, The University of Tokyo

December 2013

Abstract

A search is presented for direct chargino production based on a disappearing-track signature using 20.3 fb^{-1} of proton–proton collisions at $\sqrt{s} = 8$ TeV collected with the ATLAS experiment at the Large Hadron Collider. In anomaly-mediated supersymmetry breaking (AMSB) models, the lightest chargino is nearly mass-degenerate with the lightest neutralino and its lifetime is long enough to be detected in the tracking detectors by identifying decays that result in tracks with no associated hits in the outer region of the tracking system. Other supersymmetric models with the pure neutral wino being the lightest supersymmetric particle also predict the same signature. This analysis attains sensitivity for charginos with a lifetime between 0.1 and 10 ns, and significantly surpasses the reach of the LEP experiments due to an enhanced track reconstruction efficiency for charginos having short decay length and a dedicated topological trigger to attain a higher signal efficiency. No significant excess above the background expectation is observed for candidate tracks with large transverse momentum, and constraints on chargino properties are obtained. In the AMSB scenarios, a chargino mass below 270 GeV is excluded at 95% confidence level, which also directly constrains the mass of wino dark matter.

Contents

v

Chapter 1

Introduction

The Standard Model (SM) represents currently the most accurate and predictive description of nature, at least up to the scale of the weak interaction. It provides an almost complete picture of the interactions of matter through three out of four fundamental interactions in nature: the electromagnetic, the weak, and the strong interactions. Numerous precision measurements have validated its accuracy. However, there are still many outstanding issues that the SM does not provide the answers. This indicates that it is a low-energy approximation of a fundamental theory, and new physics beyond the SM does exist.

Supersymmetry (SUSY) is one of the most promising theories providing a solution to the problems in the SM. The SUSY is a symmetry between bosons and fermions: it transforms bosons into fermions, and vice versa. The fact that none of these particles are yet discovered indicates that the SUSY must be a broken symmetry, making the supersymmetric particles heavier than their SM partners. The SUSY breaking is assumed to occur in the hidden sector, which consists of particles that are completely neutral with respect to the SM gauge group, and its effects are mediated to the visible sector by some mechanisms.

Anomaly-mediated supersymmetry breaking (AMSB) model [1, 2], where the SUSY breaking is caused by loop effects, provides a constrained mass spectrum of SUSY particles. One prominent feature of this model is that the lightest supersymmetric particle (LSP) is the nearly pure neutral wino that is mass-degenerate with the charged wino. The lightest chargino ($\tilde{\chi}_1^\pm$) is slightly heavier than the lightest neutralino ($\tilde{\chi}_1^0$) due to radiative corrections involving electroweak gauge bosons. The typical mass splitting between $\tilde{\chi}_1^\pm$ and $\tilde{\chi}_1^0$ ($\Delta m_{\tilde{\chi}_1}$) is ~ 160 MeV, which implies that $\tilde{\chi}_1^\pm$ has a considerable lifetime and predominantly decays into $\tilde{\chi}_1^0$ plus a low-momentum $\pi^\pm$. The mean lifetime of $\tilde{\chi}_1^\pm$ ($\tau_{\tilde{\chi}_1^\pm}$) is expected to be typically a fraction of a nanosecond. Therefore, some charginos could have decay length exceeding a few tens of centimeters at the Large Hadron Collider (LHC). When decaying in the sensitive volume, they are expected to be observed as "disappearing tracks" that have no more than a few associated hits in the outer region of the tracking system, and the softly emitted $\pi^\pm$ is not reconstructed.

This dissertation explores the AMSB model by searching for charginos with their subsequent decays that result in such disappearing tracks using 20.3 fb^{-1} of proton–proton (pp) collisions at $\sqrt{s} = 8$ TeV collected with the ATLAS experiment at the LHC. Several theoretical and experimental indications motivate this search:

- The large mass of Higgs boson ∼ 126 GeV can be easily realized due to large sfermion masses [3,4,5,6].

- The neutral wino can be a plausible candidate for dark matter. The appropriate relic abundance can be obtained either through thermal freeze-out [7] or a non-thermal history with a late-decaying modulus [8].

- The problems of flavor-changing neutral currents (FCNCs) and CP violation are not serious due to the large sfermion masses and a flavor-blind mediation of SUSY breaking.

Previously, ATLAS explored charginos that have significant lifetimes via the gluino-pair production process [9, 10, 11], which sets a limit of > 800 GeV on the gluino mass. Furthermore, inclusive searches for colored supersymmetric particles [12] give a stringent limit of > 1.4 TeV on the gluino mass. Given these facts and the mass of gluino being much larger than that of wino ($m_{\tilde{g}}/m_{\tilde{\chi}_1^0} \sim 8$ in the AMSB model), a chargino with a mass of a few hundred GeV cannot be addressed via strong productions at the current LHC energy. However, the electroweak production of charginos has a sizable cross-section in pp collisions at $\sqrt{s} = 8$ TeV, and a large amount of data allows to explore the AMSB model via the electroweak production.

Chargino-pair and chargino–neutralino associated production processes dominate in the electroweak production, and they are experimentally collected and identified based on the existence of a jet with large transverse momentum (p_T) from initial-state radiation (ISR). The signal topology is then characterized by a high-p_T jet, large missing transverse momentum due to LSPs escaping the detector, and a high-p_T disappearing track. The search presented in this dissertation increases the sensitivity compared to the previous ATLAS searches [13] due to various analysis improvements. The most significant improvements are achieved by enhancing **the track reconstruction efficiency for charginos having short decay length** and **the trigger efficiency by adopting a dedicated topological trigger**.

This dissertation is organized as follows:

- Chapter 2
  An overview of the SUSY models with the pure neutral wino being the LSP and their theoretical motivations.

- Chapter 3
  The experimental setup of the LHC and the ATLAS experiment.

- Chapter 4
  The data and the simulated samples used in this dissertation.

- Chapter 5
  Various reconstruction algorithms to identify tracks, jets, electrons, muons, and missing transverse momentum.

- Chapter 6
  Tracking performances especially for short-length tracks.

- Chapter 7
  A strategy of finding chargino tracks and their properties.

- Chapter 8
  Signal selection criteria and studies on the trigger efficiency.

- Chapter 9
  Details on the background estimation.

- Chapter 10
  Systematic uncertainties on signal and background events.

- Chapter 11
  Details of the signal extraction and results.

- Chapter 12
  Interpretations of the results in the context of several SUSY models and wino dark matter scenarios.

- Chapter 13
  Concluding remarks.

Chapter 2

Theoretical Framework and Motivation

The Standard Model is currently the most precise theoretical framework to describe the sub-atomic particles and their behavior, and a large number of precision measurements have validated its accuracy. However, there are still many problems that the SM leaves unsolved. This indicates that it is a low-energy approximation of a more general underlying theory, and new physics beyond the SM does exist. Supersymmetry, which is a symmetry that relates bosons and fermions, is one of the most promising theories providing a solution to the problems in the SM. This chapter gives an overview of the SUSY models explored in this dissertation and their theoretical motivations.

2.1   The Standard Model

The SM is a relativistic quantum field theory that incorporates the basic principles of quantum mechanics and special relativity. The SM incorporates successfully three out of four fundamental interactions in nature: the electromagnetic, the weak and the strong interactions. The SM Lagrangian describes a non-Abelian gauge symmetry that refers to the group $SU(3)_C \otimes SU(2)_L \otimes U(1)_Y$, where the $SU(3)_C$ group refers to the quantum chromodynamics (QCD), the theory describing the interactions of quark and gluons by the color charge, while the $SU(2)_L \otimes U(1)_Y$ group refers to the electroweak interactions. The interactions are mediated by gauge bosons: gluons (strong interactions), photons (electromagnetic interaction), and the W and Z bosons (weak interactions).

All matter in nature is made up of elementary particles, called fermions. Figure 2.1 summarizes the elementary particles that appear in the SM. Their internal quantum numbers are also shown in the figure. The fermions can be subdivided by the interactions in which they participate. Quarks take part in the strong, electromagnetic and weak interactions, while leptons do not take part in strong

interactions. Leptons and quarks are arranged in three families, each family containing one charged lepton, one neutrino, and one up- and one down-type quark.

The masses of all elementary particles are given by the interaction with the Higgs field [14, 15]. The last piece of the SM, the Higgs boson, had been searched for at many research facilities around the world, but it was not discovered until 2012. In 2012, the ATLAS and CMS collaborations reported the strong evidence of a SM-like Higgs boson with a mass of ~ 126 GeV [16, 17]. So far, the measured couplings of the boson to the SM particles are consistent with those of the SM Higgs boson.

Figure 2.1: List of elementary particles in the Standard Model [18].

2.1.1   Outstanding issues in the Standard Model

The SM has succeeded in explaining the wide experimental results. In spite of its success, it cannot be the ultimate description of the universe. As previously mentioned, the SM only describes three out of four fundamental interactions in nature. The SM is therefore not a theory of everything. In addition to this, the SM raises three fundamental problems without providing the answers: the hierarchy problem, the grand unification and the existence of dark matter.

Hierarchy problem

One of the most problematic aspects of the SM is the numerical value of the Higgs boson mass. The Higgs boson receives large radiative corrections to its mass, which comes from loop diagrams. For example, given a Dirac fermion f that receives its

mass from the Higgs boson, the mass squared of the Higgs boson (m_h^2) is given by

$$m_h^2 \quad \approx \quad m_{h,bare}^2 + m_{h,1-loop}^2 \tag{2.1}$$

$$= \quad m_{h,bare}^2 - \frac{\lambda_f^2}{8\pi^2} N_c^f \int^{\Lambda} \frac{d^4p}{p^2} \tag{2.2}$$

$$\approx \quad m_{h,bare}^2 + \frac{\lambda_f^2}{8\pi^2} N_c^f \Lambda^2, \tag{2.3}$$

where m_h is the physical Higgs boson mass that is measured to be ~ 126 GeV, $m_{h,bare}$ is the bare Higgs boson mass, λ_f is the Yukawa coupling constant, N_c^f is the number of colors of fermion f and Λ is the largest energy scale where the standard model is valid. For large Λ, the bare mass and the 1-loop correction must cancel to a large degree to give the physical Higgs boson mass. If Λ is close to the Planck scale $\approx 10^{19}$ GeV, Eq. 2.3 implies $N^0 \equiv m_{h,bare}^2/m_h^2 \sim 10^{30}$, i.e., a *fine-tuning* of 1 part in 10^{30}.

SUSY moderates this fine-tuning [19]. If SUSY is exact and an unbroken symmetry, the Higgs boson mass receives no perturbative corrections. Due to SUSY breaking, the Higgs boson mass becomes

$$m_h^2 \approx m_{h,bare}^2 + \frac{\lambda_f^2}{8\pi^2} N_c^f (m_{\tilde{f}}^2 - m_f^2) \ln(\Lambda^2/m_{\tilde{f}}^2), \tag{2.4}$$

where $\tilde{f}$ is the superpartner of fermion f. The quadratic dependence on Λ is reduced to a logarithmic one, and the Higgs boson mass is natural if $m_{\tilde{f}}$ is not too far above m_f. The upper bound on sfermion masses is given by

$$m_{\tilde{f}} \lessapprox 800 \text{ GeV} \frac{1}{\lambda_f} \left(\frac{3}{N_c^f} \right)^{\frac{1}{2}} \left(\frac{70}{\ln(\Lambda^2/m_{\tilde{f}}^2)} \right)^{\frac{1}{2}} \left(\frac{N^0}{100} \right)^{\frac{1}{2}}, \tag{2.5}$$

where λ_f and N_c^f are normalized to values for toq quark and the logarithm term (N^0) is normalized to the value for $\Lambda \sim 10^{19}$ GeV (1 % fine-tuning), respectively.

Grand unification

In the SM, the strong, weak, and electromagnetic gauge couplings do not unify at any scale. However, in the minimal supersymmetric standard model (MSSM) [20], which is described later, the gauge coupling renormalization group equations are modified above the superpartner mass scale. If the superpartners are roughly at the weak scale, the gauge couplings unify at $\sim 10^{16}$ GeV as shown in Fig. 2.2 [20]. This fact further motivates both the grand unification and weak-scale supersymmetry.
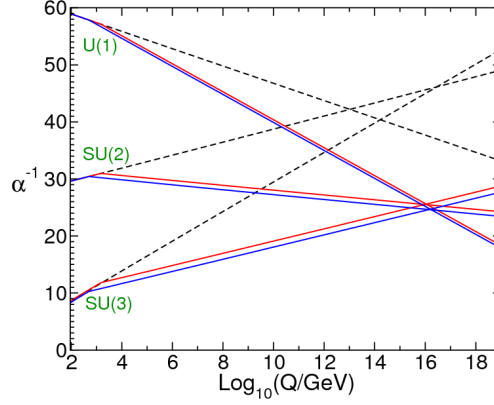
Figure 2.2: Predictions for the running of the inverse gauge couplings by the renormalization group equations. The evolution of coupling constants is shown by the dashed lines for the SM and by the solid lines for the MSSM [20]. The difference between the blue and red lines originates from changing the supersymmetric particle masses between 500 GeV and 1.5 TeV and from changing $\alpha(M_Z)$ between 0.117 and 0.121.

Dark matter

The bulk of observable matter in the universe is constituted by baryons and electrons. However, predictions on the total mass of baryonic matter in the universe from cosmic ray measurements are in contrast to those of gravitational effects. Therefore, the matter described by the SM makes up only approximately 5 % of the universe from cosmological observations, and a large part (~22 %) is considered to consist of neutral, only weakly interacting, dark matter. The SM gives no explanation for the amount of dark matter present in the universe. There are various hypotheses on dark matter depending on the mass and velocity of the particles: hot, warm, and cold dark matter. Since the velocity of warm, hot dark matter is quite high, they cannot explain the the structure of the universe, and are not regarded as the main composition of dark matter. The most popular choice is cold dark matter. According to the latest measurements of the anisotropy of the cosmic microwave background and of the spatial distribution of galaxies [21], the density of cold, non-baryonic matter is calculated to be $\Omega_{\mathrm{nbm}} h^2 = 0.112 \pm 0.006$, where h is the Hubble constant in units of 100 km/(s·Mpc). SUSY provides an excellent dark matter candidate when the neutralino is the LSP.

Gravity

The SM does not include any description of gravity. Any attempts to incorporate the theory of general relativity into the SM have not been successful so far. While gravitational effects at the electroweak scale are negligible, they become significant at the Planck scale and are of equal strength as the other forces. Since two successive supersymmetric transformations give rise to a translation in space-time, gravity would automatically be a part of supersymmetric models.

2.2 Supersymmetry

As described in the previous section, the SM is not a complete theory, and new physics beyond the SM exists. Supersymmetry is one of the most promising theories providing a solution to the problems in the SM. It establishes a symmetry between fermions and bosons. The SUSY must be a broken symmetry since no supersymmetric particles with the same mass as their SM partners have been observed. Therefore, the masses of the superpartners must be heavier than those of their SM partners.

2.2.1 Minimal Supersymmetric Standard Model

The MSSM is the simplest supersymmetric extension of the SM. Its particle content is summarized in Table 2.2.1

As the left- and right-handed states transform differently under the gauge group, individual sparticles are introduced for left- and right-handed fermions. These left- and right-handed supersymmetric states refer to not their own helicity but that of their SM partner. The superpartners of fermions are called squarks and sleptons while the superpartners of gauge bosons are called gluino, wino, and photino. The gravitino is the only particle having a spin of 3/2. The gauge interactions and couplings of the sparticles are the same as those of their SM partners.

In the SM, the electroweak symmetry is broken by introducing the Higgs mechanism, and one Higgs doublet gives masses to all particles. In the MSSM, the electroweak gauge symmetry suffers from a gauge anomaly, therefore, a Higgs field must be a weak isodoublet. One of the two Higgs supermultiplets has the Yukawa coupling that gives masses to the up-type quarks with the hypercharge $Y = 1/2$, and the Yukawa coupling of the other doublet ($Y = -1/2$) gives masses to the down-type quarks and the charged leptons. They are denoted by H_u and H_d, respectively, and the vacuum expectation values (VEVs) of H_u^0 and H_d^0 are written as

$$v_u = \langle H_u^0 \rangle, \qquad v_d = \langle H_d^0 \rangle. \qquad (2.6)$$

These VEVs are related to the SM parameters by

$$v_u^2 + v_d^2 = v^2 = \frac{2m_Z^2}{g_1^2 + g_2^2},$$ (2.7)

where v, g_1 and g_2 are VEVs of the SM Higgs boson, the gauge coupling constants of $U(1)_Y$ and $SU(2)_L$ gauge groups, respectively. The ratio of the VEVs is an important parameter and set to be free in the theory, and it is traditionally written as

$$\tan\beta \equiv \frac{v_u}{v_d}.$$ (2.8)

These two doublets have eight degrees of freedom. Three are absorbed by the gauge bosons of the weak interaction as in the SM, leaving five physical Higgs bosons. These five Higgs scalar mass eigenstates consist of two CP-even neutral scalars h^0 and H^0, one CP-odd neutral scalar A^0, and charged scalars $H^\pm$.

The superpartners of the Higgs bosons are called Higgsinos, denoted by $\tilde{H}_u$ and $\tilde{H}_d$ for the $SU(2)_L$-doublet left-handed spinor fields, with weak isospin components $(\tilde{H}_u^+, \tilde{H}_u^0)$ and $(\tilde{H}_d^0, \tilde{H}_d^-)$. The mass of Higgsinos is given by μ_H.

The superpartners of the SM gauge bosons, arranged in gauge supermultiplets, are not the mass eigenstates of the MSSM. The Higgsinos and electroweak gauginos mix with each other due to the effects of the electroweak symmetry breaking. The neutral Higgsinos ($\tilde{H}_u^0$ and $\tilde{H}_d^0$) and the neutral gauginos ($\tilde{B}^0$ and $\tilde{W}^0$) combine to form four mass eigenstates called neutralinos $\tilde{\chi}_i^0$ (i = 1,2,3,4). The charged Higgsinos ($\tilde{H}_u^+$ and $\tilde{H}_d^-$) and winos ($\tilde{W}^+$ and $\tilde{W}^-$) mix to form two mass eigenstates with charge ± 1 called charginos $\tilde{\chi}_i^\pm$ (i = 1, 2). The neutralinos are Majorana fermions in the MSSM.

Name	Spin	Gauge eigenstates	Mass eigenstates
Squarks	0	$\tilde{u}_L, \tilde{u}_R, \tilde{d}_L, \tilde{d}_R$ $\tilde{c}_L, \tilde{c}_R, \tilde{s}_L, \tilde{s}_R$ $\tilde{t}_L, \tilde{t}_R, \tilde{b}_L, \tilde{b}_R$	$\tilde{t}_1, \tilde{t}_2, \tilde{b}_1, \tilde{b}_2$
Sleptons	0	$\tilde{e}_L, \tilde{e}_R, \tilde{\nu}_e$ $\tilde{\mu}_L, \tilde{\mu}_R, \tilde{\nu}_\mu$ $\tilde{\tau}_L, \tilde{\tau}_R, \tilde{\nu}_\tau$	$\tilde{\tau}_1, \tilde{\tau}_2, \tilde{\nu}_\tau$
Higgs bosons	0	$H_u^0, H_d^0, H_u^+, H_d^-$	$h^0, H^0, A^0, H^\pm$
Neutralinos	1/2	$\tilde{B}^0, \tilde{W}^0, \tilde{H}_u^0, \tilde{H}_d^0$	$\tilde{\chi}_1^0, \tilde{\chi}_2^0, \tilde{\chi}_3^0, \tilde{\chi}_4^0$
Charginos	1/2	$\tilde{W}^\pm, \tilde{H}_u^+, \tilde{H}_d^-$	$\tilde{\chi}_1^\pm, \tilde{\chi}_2^\pm$
Gluino	1/2	$\tilde{g}$	
Gravitino	3/2	$\tilde{G}$	

Table 2.1: Supersymmetric particles in the MSSM.

2.2.2 R-parity

In the SM, the baryon number and lepton number are conserved since no possible renormalizable Lagrangian terms can introduce the violation of such numbers. In the MSSM, the most general gauge-invariant renormalizable superpotential contains the terms that violate the conservation of the baryon number and lepton number, inducing the rapid proton decay. Since this decay has not been confirmed experimentally, these terms need to be suppressed. Therefore, an additional quantum number called R-parity, is defined as

$$R = (-1)^{2S+3(B-L)}, \qquad (2.9)$$

where S, B and L is the spin, the baryon number, and the lepton number, respectively. Employing this definition results in $R = 1$ ($R = 1$) for all SM particles (SUSY particles). Assuming exact R-parity conservation indicates several significant consequences:

- SUSY particles can only be produced in pairs, resulting in two decay chains.

- Eventually, every sparticle decays into the LSP.

- The LSP is stable. It behaves like neutrinos and escapes from detection, resulting in a noticeable amount of missing transverse momentum (and its magnitude $E_{\mathrm{T}}^{\mathrm{miss}}$) in collider experiments. If the LSP is neutral and has no color, it can be considered as a viable dark matter candidate.

The phenomenology of R-parity violating models is quite different because the LSP decays into SM particles. Throughout this dissertation, R-parity is assumed to be conserved.

2.2.3 SUSY breaking model

Since it is difficult to construct a realistic model of spontaneous SUSY breaking from the interaction between the particles in the MSSM, a hidden sector is introduced, which consists of particles that are completely neutral with respect to the SM gauge group. The SUSY breaking is assumed to occur in the hidden sector, and its effects are mediated to the visible sector by some mechanisms. In the general MSSM, 105 free parameters are added to the 19 of the SM. Assuming a specific breaking mechanism reduces the number of free parameters that determine the masses of all SUSY particles and their mixing.

2.3 Wino LSP scenarios and their phenomenology

In this analysis, one of the most prominent models called Anomaly-Mediated Supersymmetry Breaking is explored.

2.3.1 Anomaly-Mediated Supersymmetry Breaking model

Anomaly-Mediated Supersymmetry Breaking Model has no direct tree level coupling that mediates the SUSY breaking in the hidden sector to the observable sector. A conformal anomaly in the auxiliary field of the supergravity multiplet mediates the SUSY breaking to the observable sector, and the AMSB model does not require any singlet SUSY breaking fields (i.e. the Polonyi fields), and hence, are free from the cosmological Polonyi problem [22, 23].

In the AMSB model, the masses of gauginos are generated at one-loop, while those of the scalar bosons are generated at two-loop level, because of the conformal anomaly that breaks scale invariance. The bino, wino, and gluino masses (M_1, M_2 and M_3) have a special property that they are proportional to the coefficients of the renormalization group equations for their corresponding gauge groups:

$$M_1 = \frac{g_1^2}{16\pi^2}\left(\frac{33}{5}m_{3/2}\right), \tag{2.10}$$

$$M_2 = \frac{g_2^2}{16\pi^2}(m_{3/2}), \tag{2.11}$$

$$M_3 = \frac{g_3^2}{16\pi^2}(-3m_{3/2}), \tag{2.12}$$

where g_3 and $m_{3/2}$ are the gauge coupling constants of $SU(3)_C$ gauge groups and the gravitino mass, respectively. The mass relation between the gauginos becomes $M_1 : M_2 : M_3 \approx 3 : 1 : 8$. The masses of squarks and sleptons [24] are obtained as

$$M_{\tilde{u}_L}^2 = m_0^2 + \left(\frac{1}{2} - \frac{2}{3}\sin^2\theta_W\right)M_Z^2\cos2\beta + \left(-\frac{11}{50}g_1^4 - \frac{3}{2}g_2^4 + 8g_3^4\right)\frac{m_{3/2}^2}{(16\pi^2)^2}, \tag{2.13}$$

$$M_{\tilde{d}_L}^2 = m_0^2 + \left(-\frac{1}{2} + \frac{1}{3}\sin^2\theta_W\right)M_Z^2\cos2\beta + \left(-\frac{11}{50}g_1^4 - \frac{3}{2}g_2^4 + 8g_3^4\right)\frac{m_{3/2}^2}{(16\pi^2)^2} \tag{2.14}$$

$$M_{\tilde{u}_R}^2 = m_0^2 + \frac{2}{3}\sin^2\theta_W M_Z^2\cos2\beta + \left(-\frac{88}{25}g_1^4 + 8g_3^4\right)\frac{m_{3/2}^2}{(16\pi^2)^2}, \tag{2.15}$$

$$M_{\tilde{d}_R}^2 = m_0^2 - \frac{1}{3}\sin^2\theta_W M_Z^2\cos2\beta + \left(-\frac{22}{25}g_1^4 + 8g_3^4\right)\frac{m_{3/2}^2}{(16\pi^2)^2}, \tag{2.16}$$

$$M_{\tilde{e}_L}^2 = m_0^2 + \left(-\frac{1}{2} + \sin^2\theta_W\right)M_Z^2\cos2\beta + \left(-\frac{99}{50}g_1^4 - \frac{3}{2}g_2^4\right)\frac{m_{3/2}^2}{(16\pi^2)^2}, \tag{2.17}$$

$$M_{\tilde{\nu}_e}^2 = m_0^2 + \frac{1}{2}M_Z^2\cos2\beta + \left(-\frac{99}{50}g_1^4 - \frac{3}{2}g_2^4\right)\frac{m_{3/2}^2}{(16\pi^2)^2}, \tag{2.18}$$

$$M_{\tilde{e}_R}^2 = m_0^2 - \sin^2\theta_W M_Z^2\cos2\beta + \left(-\frac{198}{25}g_1^4\right)\frac{m_{3/2}^2}{(16\pi^2)^2}, \tag{2.19}$$

where m_0 and θ_W are the universal scalar mass at the grand unification scale and the Weinberg angle, respectively.

In the AMSB model, m_0 must be large otherwise the scalar leptons become tachyons. Then all sfermions become too heavy to be produced in hadron collider experiments. Figure 2.3 shows a sparticle mass spectrum for a certain parameter set of the AMSB model.
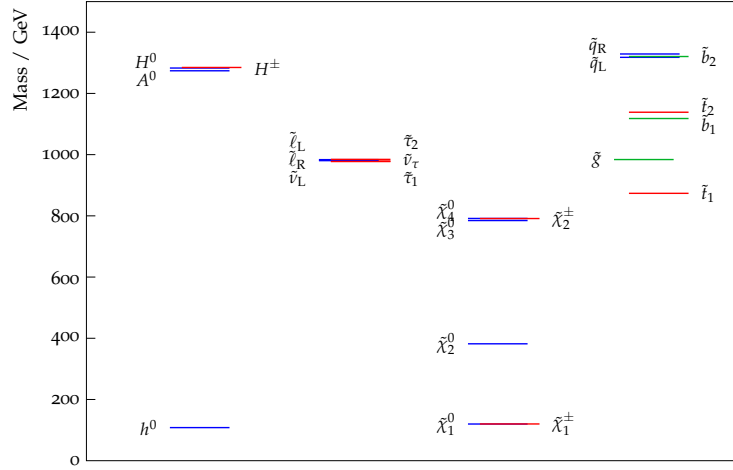
Figure 2.3: Sparticle mass spectrum for $m_{3/2} = 32$ TeV, $m_0 = 1000$ GeV, $\tan\beta = 5$ and $\mu_H > 0$.

2.3.2 Pure Gravity Mediation model

There is another well-motivated SUSY model that predicts the sparticle mass spectrum similar to that in the AMSB model, called Pure Gravity Mediation (PGM) model [3]. In this model, the gauginos obtain their masses by one-loop contributions in supergravity as in the AMSB model. The difference between the AMSB and PGM models is that the gauginos in the PGM model obtain their masses from additional contributions from threshold effects of the heavy Higgsinos. The gaugino masses are given by

$$M_1 = \frac{g_1^2}{16\pi^2}\frac{33}{5}(m_{3/2} + \frac{1}{11}L), \qquad (2.20)$$

$$M_2 = \frac{g_2^2}{16\pi^2}(m_{3/2} + L), \qquad (2.21)$$

$$M_3 = \frac{g_3^2}{16\pi^2}(-3m_{3/2}), \qquad (2.22)$$

where L denotes the Higgsino threshold contribution given by

$$L \equiv \mu_H \sin2\beta \frac{m_A^2}{|\mu_H|^2 - m_A^2} \ln \frac{|\mu_H|^2}{m_A^2}. \tag{2.23}$$

The size of the L parameter is expected to be of the order of the gravitino mass. In the limit for the L parameter to zero, the gaugino masses become the same ones in the AMSB model. The gluino mass is about eight times higher than the wino mass for L = 0 as in the AMSB model, while the gluino-to-wino mass ratio gets smaller for positive values of L.

2.3.3   Phenomenology

One prominent feature of these models is that the LSP is the pure neutral wino that is mass-degenerate with the charged wino. The lightest chargino $\tilde{\chi}_1^{\pm}$ is slightly heavier than the lightest neutralino $\tilde{\chi}_1^0$ due to radiative corrections involving electroweak gauge bosons. The typical mass splitting between $\tilde{\chi}_1^{\pm}$ and $\tilde{\chi}_1^0$ is ~ 160 MeV as shown in Fig. 2.4, which implies that $\tilde{\chi}_1^{\pm}$ has a considerable lifetime and predominantly decays into $\tilde{\chi}_1^0$ plus a low-momentum (~ 100 MeV) $\pi^{\pm}$. Figure 2.5 shows $\tau_{\tilde{\chi}_1^{\pm}}$ as a function of $\Delta m_{\tilde{\chi}_1}$ on the assumption that $\tilde{\chi}_1^{\pm}$ decays into $\tilde{\chi}_1^0 + \pi^{\pm}$. The decay width for this process is given as

$$\Gamma\left(\tilde{\chi}_1^{\pm} \to \tilde{\chi}_1^0 \pi^{\pm}\right) = \frac{2G_F^2}{\pi} \cos^2\theta_c f_{\pi}^2 \Delta m_{\tilde{\chi}_1}^3 \left(1 - \frac{m_{\pi}^2}{\Delta m_{\tilde{\chi}_1}^2}\right)^{\frac{1}{2}}, \tag{2.24}$$

where G_F, θ_c, f_{π} and m_{π} are the Fermi coupling constant, the Cabbibo angle, the pion decay constant ($\simeq$ 130 MeV), and the pion mass, respectively, resulting in a considerably long lifetime of the chargino:

$$c\tau_{\tilde{\chi}_1^{\pm}} \sim O(\text{cm}) \ (\tau_{\tilde{\chi}_1^{\pm}} \sim 0.2\text{ns}). \tag{2.25}$$

Therefore, a fraction of decaying charginos could be reconstructed as tracks in the collider experiments. The $\tilde{\chi}_1^0$ escapes from detection and the softly emitted $\pi^{\pm}$ is not reconstructed due to its low momentum as shown in Fig. 2.6 . A track arising from a $\tilde{\chi}_1^{\pm}$ with these characteristics is classified as a *disappearing track* that has few associated hits in the outer part of the tracking volume.

2.3.4   Theoretical and experimental indications

There are several theoretical and experimental indications that motivate exploring wino LSP scenarios.
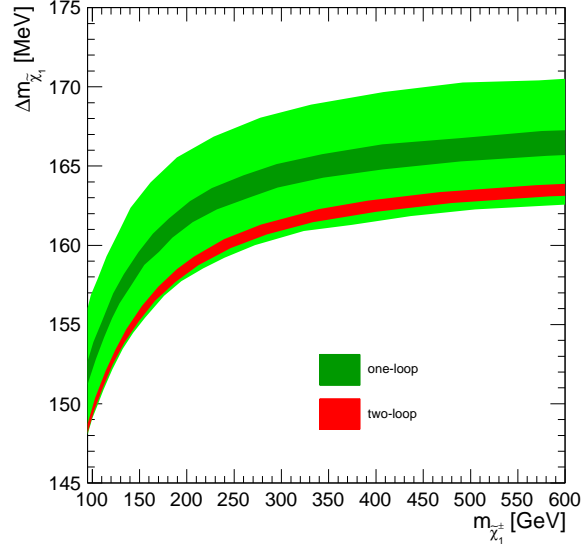
Figure 2.4: Wino mass splitting $\Delta m_{\tilde{\chi}_1}$ as a function of the chargino mass ($m_{\tilde{\chi}_1^\pm}$) [25]. The dark green band shows $\Delta m_{\tilde{\chi}_1}$ at the one-loop level with the uncertainty induced by the renormalization scale dependence and the red band shows $\Delta m_{\tilde{\chi}_1}$ at two-loop.
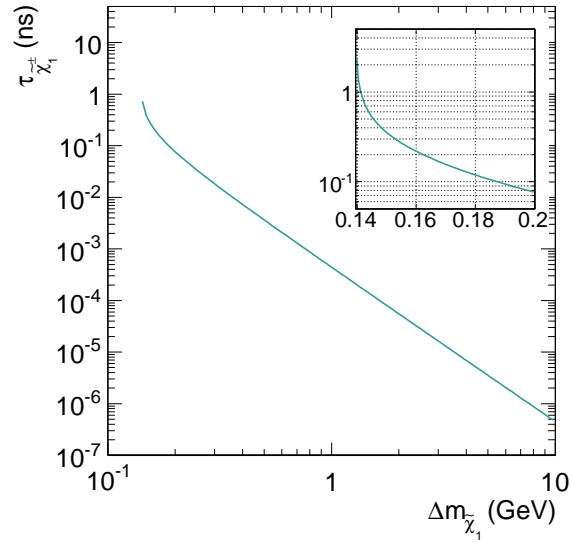
Figure 2.5: The $\tau_{\tilde{\chi}_1^\pm}$ as a function of $\Delta m_{\tilde{\chi}_1}$.
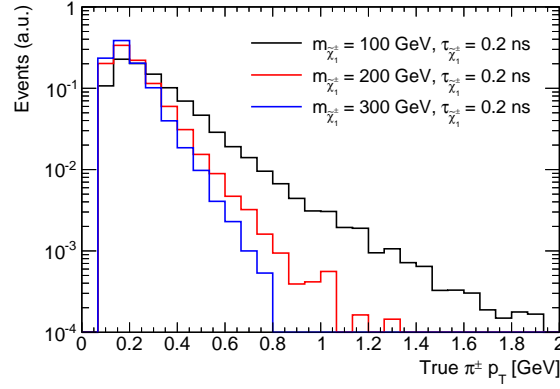
Figure 2.6: The p_T spectrum of $\pi^\pm$ in the charagino decays.

Higgs mass

The mass of the lightest Higgs boson (h^0) in the MSSM [26] is obtained by

$$\text{m}_{\text{h}^0}^2 \leq \text{m}_\text{Z}^2\cos^2 2\beta + \frac{3}{4\pi^2}\text{y}_\text{t}^2\text{m}_\text{t}^2\sin^2\beta(\log\frac{\text{m}_{\tilde{\text{t}}}^2}{\text{m}_\text{t}^2} + \frac{\text{A}_\text{t}^2}{\text{m}_{\tilde{\text{t}}}^2} - \frac{\text{A}_\text{t}^4}{12\text{m}_{\tilde{\text{t}}}^4}). \qquad (2.26)$$

The Higgs mass is required to be less than the Z boson mass at tree level. While loop corrections increase this upper bound, the logarithmic term implies that the stop mass should be at least $\mathcal{O}$(10-100) TeV to realize the Higgs boson mass ~ 126 GeV [16,17]. Figure 2.7 shows a contour plot of the Higgs boson mass as a function of $\tilde{m}$ and $\tan\beta$, where $\tilde{m}$ is a typical sfermion mass [4]. This figure also indicates that the Higgs boson mass of ~ 126 GeV is realized if $\tilde{m}$ is ~ $\mathcal{O}$(10-100) TeV and the $\tan\beta$ is ~ $\mathcal{O}$(1). These features are consistent with the fact that any sfermions have not yet been observed at the LHC. The masses of sferimons in the AMSB model are generally large as stated before, therefore, the observed Higgs boson mass can be easily explained in the AMSB model.

Flavor Changing Neutral Current

The SUSY breaking terms for squark and slepton masses can induce too large FCNCs [27] since squark and slepton mass matrices can be new sources of flavor mixings and CP violation that are not related to the Cabibbo-Kobayashi-Maskawa matrix. With generic mass matrices and $\mathcal{O}$(1) CP violating phases, K^0-$\bar{K}^0$ mixing requires the squark masses to be greater than 1000 TeV. However, the problems of FCNCs and CP violation is not serious in the AMSB model since the soft SUSY breaking parameters are given by flavor-blind radiative corrections and the masses of squarks and sleptons are large.
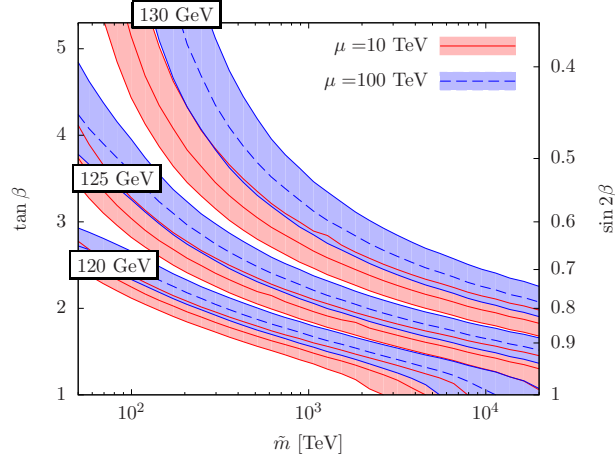
Figure 2.7: Values of the Higgs boson mass in the $\tilde{m}$–$\tan\beta$ plane, where $\tilde{m}$ is sfermion mass [4]. The solid (red) curves represent ones with $\mu_{\rm H}$ = 10 TeV, while the dashed (blue) curves $\mu_{\rm H}$ = 100 TeV. The shaded region around each curve shows uncertainty from the top quark mass.

Wino dark matter scenario

The neutral wino can be the most natural candidate for dark matter. The thermal relic density of neutral wino can be the present mass density of dark matter if its mass is about 3.0 TeV [7]. For light winos with masses about a few hundred GeV, the measured relic abundance requires a non-thermal history with a late-decaying modulus [8] due to their large tree-level annihilation rate to W bosons. It has been argued that moduli with a mass of $\mathcal{O}(100)$ TeV are consistent with Big Bang nucleosynthesis (BBN) and lead to the right relic abundance for light winos with masses about a few hundred GeV.

2.3.5 Previous searches and constraints

There are several constraints on wino LSP scenarios from collider experiments and indirect dark matter searches. Collider experiments can explore wino LSP scenarios and provide results that are largely independent of the model parameters. Indirect dark matter searches can provide complementary results and set limits on the wino dark matter especially in the non-thermal scenario, although they have a large uncertainty due to ambiguities of the dark matter profile, magnetic fields, and interstellar radiation density.

LEP2 experiment

Searches for the charginos nearly mass-degenerate with the lightest neutralino were performed by experiments at LEP2 [28, 29, 30]. These analyzes are based on the events with a photon from ISR and the missing energy due to LSPs escaping the detector. Figure 2.8 shows the constraint on the $\Delta m_{\tilde{\chi}_1}$–$m_{\tilde{\chi}_1^{\pm}}$ space of the AMSB model by combining the LEP2 results, excluding the chargino having a mass up to 92 GeV [31].
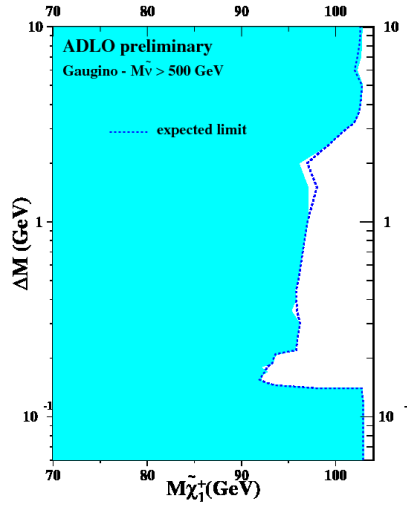
Figure 2.8: Constraint on the $\Delta m_{\tilde{\chi}_1}$–$m_{\tilde{\chi}_1^{\pm}}$ space derived by the results of the LEP2 experiments [31].

ATLAS experiment

Prior to the search described in this dissertation, a search for charginos nearly mass-degenerate with the lightest neutralino was also performed in pp collisions at $\sqrt{s} = 7$ TeV with the ATLAS detector [13]. The analysis is dedicated to the direct chargino production process and is based on the disappearing track signature. Figure 2.9 and 2.10 show the constraint on the $\tau_{\tilde{\chi}_1^{\pm}}$–$m_{\tilde{\chi}_1^{\pm}}$ space and $\Delta m_{\tilde{\chi}_1}$–$m_{\tilde{\chi}_1^{\pm}}$ of the AMSB model, respectively. The previous result excludes the chargino having a mass up to 130 GeV.

Indirect dark matter searches

There are a number of constraints on wino dark matter [32, 33] from indirect detection experiments of Fermi Gamma-Ray Space Telescope (Fermi) experiment [34] and High Energy Spectroscopic System (H.E.S.S.) experiment [35].
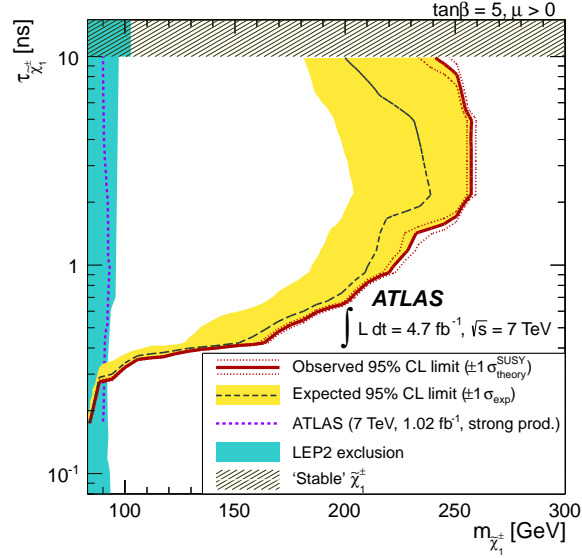
Figure 2.9: Constraint on the $\tau_{\tilde{\chi}_1^\pm}$–$m_{\tilde{\chi}_1^\pm}$ space in *pp* collisions at $\sqrt{s} = 7$ TeV with the ATLAS detector [13].
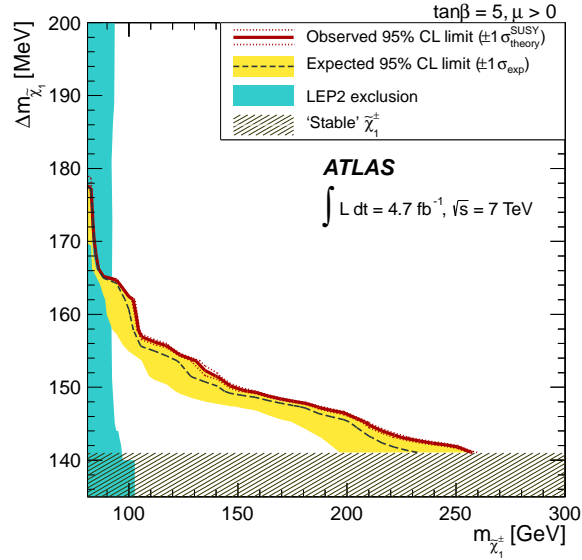
Figure 2.10: Constraint on the $\Delta m_{\tilde{\chi}_1}$–$m_{\tilde{\chi}_1^\pm}$ space in *pp* collisions at $\sqrt{s} = 7$ TeV with the ATLAS detector [13].

The Fermi result is derived by 24 months of data for ten satellite galaxies, and sets the limits on the annihilation cross-section of the wino dark matter by a search for the continuum photons generated mostly from the fragmentation of hadronic

final states in the tree-level processes $\tilde{\chi}_1^0 \tilde{\chi}_1^0 \rightarrow W^+ W^-$. This is roughly comparable to that obtained from the antiproton flux measurement by PAMELA [36]. The antiproton measurement is subjected to uncertainties related to their propagation models and dark matter profiles, therefore, PAMELA results are not shown in this dissertation.

The H.E.S.S. collaboration investigated gamma-ray lines expected to arise from the one-loop processes $\tilde{\chi}_1^0 \tilde{\chi}_1^0 \rightarrow \gamma \gamma$ and $\tilde{\chi}_1^0 \tilde{\chi}_1^0 \rightarrow Z \gamma$ in a $1°$ radius circle at the Galactic Center, in which the Galactic plane is excluded by restricting the Galactic latitude to $|b| > 0.3°$.

Figure 2.11 and 2.12 show the theoretical calculations of annihilation cross-section into $W^+ W^-$, $\gamma \gamma$ and γZ final states and the constraints on the wino annihilation cross-section as a function of wino mass [32]. The wino relic density is assumed to equal to its thermal abundance in Fig. 2.11, while it is assumed to equal to the measured value due to a non-thermal history with a late-decaying modulus in Fig. 2.12. In the thermal scenario, the data from H.E.S.S. rules out wino dark matter in the mass range 1.6 TeV – 3.1 TeV. In the non-thermal scenario, the data from Fermi and H.E.S.S. exclude wino dark matter in the ranges 100 GeV – 500 GeV and 500 GeV – 3.0 TeV, respectively.

Direct dark matter searches

The direct detection of dark matter can take place through their interaction with nuclei inside a detector. However, couplings of neutral wino to a Higgs boson or a Z boson are highly suppressed at the tree-level, therefore, there has been no direct detection limits on wino LSP scenarios. The elastic scattering of a wino off a nucleon occurs at one-loop where wino couples to quarks and two-loop where wino couples to gluons in the nucleon. The associated spin-independent cross-section is $O(10^{-47})$ cm^2 for winos [37,38] having masses 50 GeV – 3 TeV, which is well below the strongest direct detection limits from the Xenon100 experiment [39].
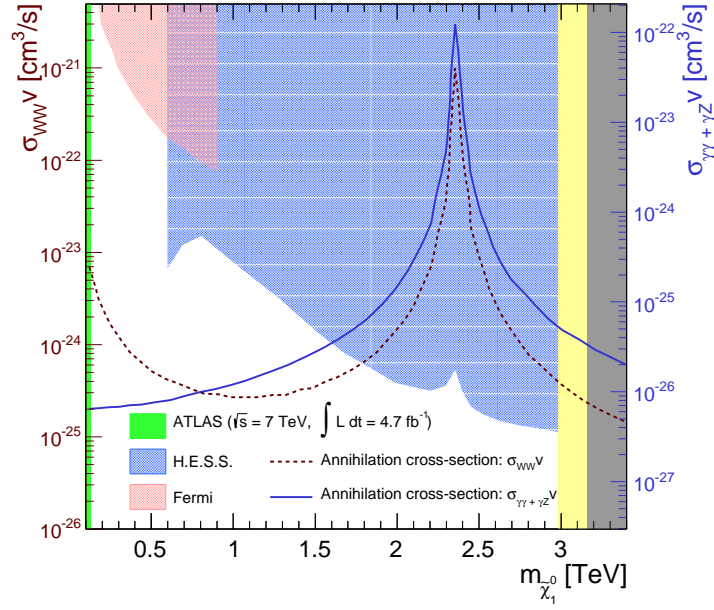
Figure 2.11: Constraints on the annihilation cross-section as a function of the wino mass [32]. The theoretical cross-section of annihilation into $W^+ W^-$, $\gamma\,\gamma$ and $\gamma\,Z$ final states are also indicated by the dashed red line and the solid blue line, respectively. The excluded regions by the Fermi and H.E.S.S. experiments are indicated by the shaded red region and the shaded blue region, respectively. These exclusion contours are obtained on the assumption that the wino abundance is set by thermal freeze-out. The shaded yellow region between the dotted lines corresponds to $\Omega h^2 = 0.12 \pm 0.06$. In the black shaded region, a thermal wino exceeds the observed relic density.
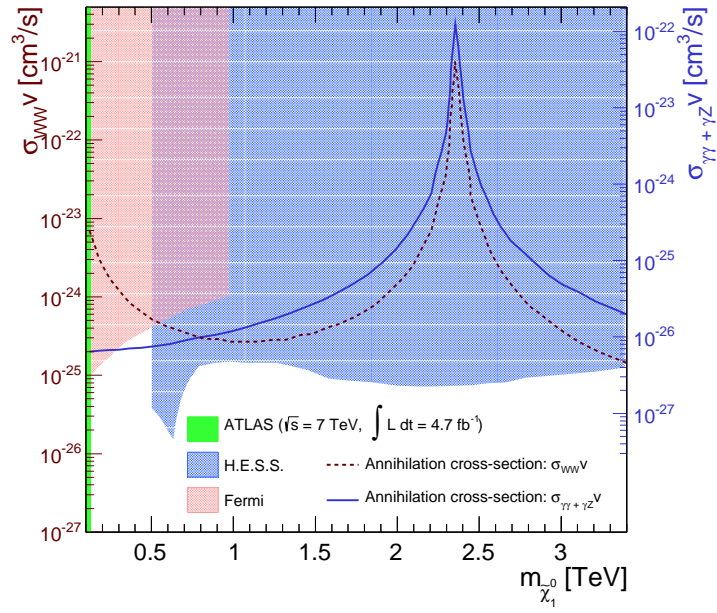
Figure 2.12: Constraints on the annihilation cross-section as a function of the wino mass [32]. The theoretical cross-section of annihilation into $W^+ W^-$, γ γ and γ Z final states are also indicated by the dashed red line and the solid blue line, respectively. The excluded regions by the Fermi and H.E.S.S. experiments are indicated by the shaded red region and the shaded blue region, respectively. These exclusion contours are obtained on the assumption that the wino comprises all dark matter due to a non-thermal history.

Chapter 3

LHC and ATLAS Detector

3.1 Large Hadron Collider

The LHC is a two-ring-superconducting-hadron accelerator and collider built by the european organization for nuclear research (CERN). It lies between 45 m and 170 m below the surface on a plane inclined at 1.4 %. It was installed in the existing 26.7 km tunnel that was built for the LEP experiment. The LHC has been designed to collide proton beams with a center-of-mass energy of 14 TeV and an instantaneous luminosity of 10^{34}cm^{-2}s^{-1}. It can also collide heavy lead (Pb) ions with an energy of 2.8 TeV per nucleon and a peak luminosity of 10^{27}cm^{-2}s^{-1}.

The protons are obtained from a duoplasmatron source. It ionizes hydrogen atoms and uses electric fields to accelerate the protons away from the electrons, resulting in a 92 keV proton beam. The protons are then formed into bunches and injected into the linear particle accelerator (LINAC) where they are accelerated to 50 MeV before being fed into the first circular accelerator in the chain, the proton synchrotron booster (PSB). The PSB accelerates the protons to 1.4 GeV and injects them into the proton synchrotron (PS), which accelerates the protons to 25 GeV before being injected into the super proton synchrotron (SPS), which accelerates the protons to 450 GeV. These protons are finally injected into the LHC, which accelerated each beam of protons to 4 TeV in 2012, resulting in a center-of-mass energy of 8 TeV. The proton beam parameters of the LHC and CERN accelerator complex are shown in Table 3.1 and Fig. 3.1, respectively.

Four main experiments have been installed in four of the eight interaction points (IPs) of the LHC ring: ATLAS [40,41,42] and CMS [43] are general-purpose detectors for studying *pp* collisions at the highest luminosity and at the maximum center-of-mass energy. The LHCb [44] experiment is dedicated to heavy flavor physics. It is designed to search for indirect evidences of new physics in CP violation and rare decays of beauty and charm hadrons, which can help to explain the matter-antimatter asymmetry of the universe. ALICE [45] is an experiment focused on the study of heavy ion collisions at the LHC. It is designed to study the physics of strongly interacting matter and the quark-gluon plasma at an extreme

	Design	2012 Run
Proton energy [GeV]	7000	4000
Bunch spacing [ns]	25	50
Number of bunches	2808	1380
Number of particles per bunch	1.15×10^{11}	$\sim 1.7 \times 10^{11}$
Peak luminosity [cm^{-2}s^{-1}]	1.0×10^{34}	7.7×10^{33}
Magnetic field on the dipoles [T]	8.33	4.76
Beam current [A]	0.582	0.369
Bunch length [cm]	7.55	≥ 9
Transverse beam size at IP [μm]	16.7	19
Crossing angle at IP [μrad]	285	290

Table 3.1: The LHC proton beam parameters.
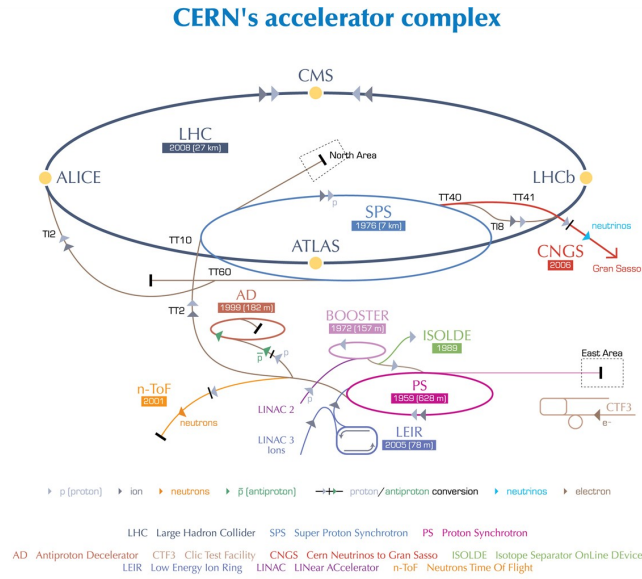
Figure 3.1: The LHC accelerator complex. The protons are accelerated by the LINAC, the PSB, the PS, and the SPS accelerators prior to injection into the LHC.

energy density and temperature.

3.2   ATLAS detector

The ATLAS (A Toroidal LHC ApparatuS) detector is a general purpose detector at the LHC. The ATLAS detector covers nearly 4π around the collision point and is 45 m long, 25 m in diameter, and weighs about 7000 tons. It is designed to accommodate a wide spectrum of possible physics signatures such as the discovery of Higgs boson and beyond the SM.

The ATLAS detector consists of an ensemble of sub-detectors with a cylindrical shape placed around the IP: the inner detector (ID), which is used for tracking of charged particles, the calorimeters, which are used for measuring the energies of the particles interacting with them, and the muon spectrometer, which is used for identifying muons and measuring their momenta. A magnet system is used to bend the charged particles to measure their momenta. The layout of the ATLAS detector is shown in Fig. 3.2. A trigger system is also implemented, which is used to decide which events should be recorded in a very short time.
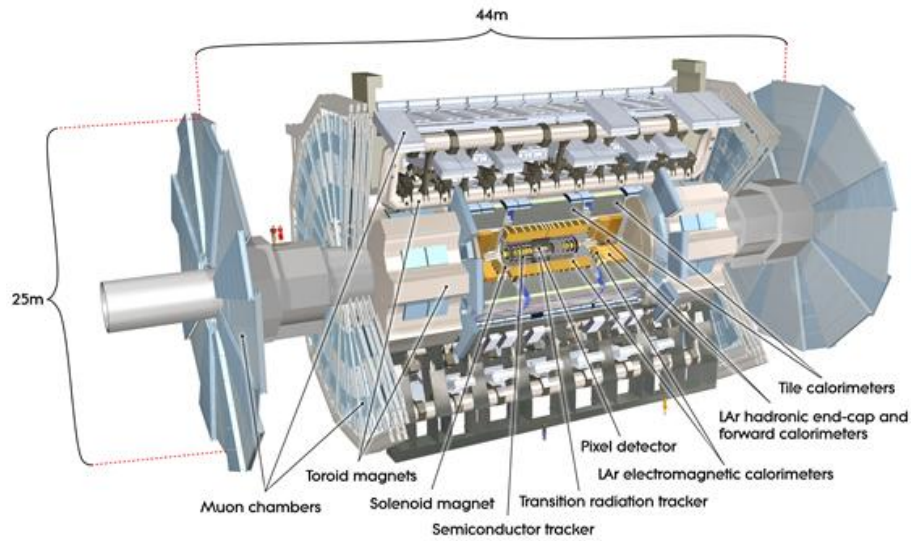
Figure 3.2: Three dimensional view of the ATLAS detector.

3.2.1   ATLAS coordinate

ATLAS uses a right-handed Cartesian coordinate system (x,y,z) with its origin at the nominal IP in the center of the detector and the z-axis coinciding with the axis

of the beam pipe. The *x*-axis points from the IP to the center of the LHC ring, and the *y*-axis points upward. A cylindrical coordinate system (r, ϕ, z) and a polar coordinate system (r, θ, ϕ) are defined in the transverse plane as

$$r = \sqrt{x^2 + y^2}, \tag{3.1}$$

$$\phi = \arctan\left(\frac{y}{x}\right), \tag{3.2}$$

$$\theta = \arctan\left(\frac{r}{z}\right). \tag{3.3}$$

The rapidity (y_{rap}) is defined as

$$y_{rap} = \frac{1}{2} \ln\left(\frac{E + p_z}{E - p_z}\right), \tag{3.4}$$

where E and p_z are the energy and the momentum along the beam direction, respectively. The pseudo-rapidity (η), which is equal to the rapidity in the ultra-relativistic approximation, is also often used in collider physics. It is defined in terms of the polar angle θ as

$$\eta = -\ln\tan\left(\frac{\theta}{2}\right). \tag{3.5}$$

The distance in the pseudorapidity-azimuthal angle space (ΔR) is defined as

$$\Delta R = \sqrt{(\Delta\eta)^2 + (\Delta\phi)^2}, \tag{3.6}$$

where $\Delta\eta$ and $\Delta\phi$ are the distance in the pseudorapidity and azimuthal angle space, respectively.

3.2.2 Magnet system

The ATLAS magnet system consists of four superconducting magnets. A central solenoid aligned on the beam axis provides the ID with an axial magnetic field, and three large air-core toroids located outside the calorimeters provide the muon spectrometer with a toroidal magnetic field. This configuration is shown in Fig. 3.3.

The solenoid magnet system

The central solenoid [46] is aligned on the beam axis and designed to provide the ID with a 2 T axial magnetic field. The solenoid is a layer coil made of a Al-stabilized NbTi conductor. It has an inner (outer) diameter of 2.46 (2.56) m with an axial length of 5.8 m. The flux of magnetic field is returned by the steel of the hadronic calorimeter.

Since the solenoid magnet lies in front of the calorimeter system, its presence must have a small impact on the energy measurement in the calorimeters. Therefore, it is designed to keep the material thickness as low as possible, contributing with a total of $\sim$ 0.66 radiation length (X_0). For this requirement, the solenoid windings and the electromagnetic calorimeter share a common vacuum vessel to eliminate two vacuum walls.

The toroidal magnet system

The toroidal magnet system [47] consists of one barrel and two endcap magnets. It provides a toroidal magnetic field of 0.5 T and 1 T for the muon spectrometer in the central and endcap regions, respectively. It lies outside the calorimeters and within the muon system. The conductor and coil-winding technology is based on winding a pure Al-stabilized Nb/Ti/Cu conductor.

The barrel toroid consists of eight coils encased in individual racetrack-shaped stainless-steel vacuum vessels. It provides a peak magnetic field of 3.9 T. The coils are assembled radially and symmetrically around the beam axis. It has an inner (outer) diameter of 9.4 (20.1) m with a length of 25.3 m.

The endcap toroids are placed inside the barrel toroid at both ends of the central solenoid. They have an inner (outer) diameter of 1.65 (10.7) m with an axial length of 5 m. Each endcap is rotated by 22.5° with respect to the barrel toroid in order to provide the radial overlap and optimize the bending power. Each endcap toroid consists of a single cold mass built from eight coils in an aluminum alloy housing. The endcap toroids provide a peak magnetic field of 4.1 T.

3.2.3   Inner detector

The inner detector [48, 49] is designed to reconstruct the trajectories of charged particles in the region $|\eta| < 2.5$. Figure 3.4 (a) and (b) show an overview and a layout of the ID, respectively. The ID is contained within a cylindrical envelope of length ±3512 mm and of radius 1150 mm. The ID is surrounded by the solenoid magnet with the 2 T axial magnetic field in order to measure the momentum of charged particles.

The ID consists of pixel and silicon microstrip (SCT) detectors inside a straw-tube transition radiation tracker (TRT). The pixel detector consists of three barrel layers and four endcap disks on each side, providing an average three measurement points for charged tracks. The SCT is composed of four cylindrical layers of double-sided silicon microstrip modules, with nine disk layers in each endcap region; eight silicon microstrip sensors are typically crossed by each track. The TRT, of particular importance to this search, covers $|\eta| < 1.0$ with its barrel detector, $0.8 < |\eta| < 2.0$ with the endcaps, and the radial range 563–1066 mm. The average number of TRT hits on a track traversing the ID in the central region is about 32. The first two sub-detectors use semiconductor technology and provide a small number of hits on a track, while the TRT uses straw tubes providing a continuous
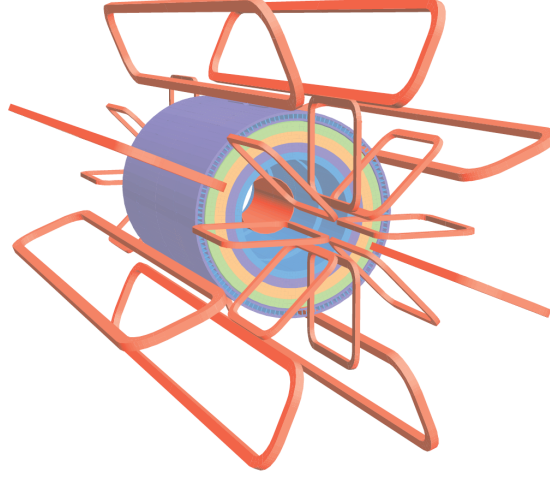
Figure 3.3: The ATLAS magnet system. The solenoid lies at the innermost radius of the calorimeter system, and the steel of the hadronic calorimeter act as a return yoke for the solenoids field. The eight barrel toroid coils are interleaved with the two endcap toroid coils.

tracking up to large radii. Each of the sub-detectors is divided in a barrel region, where they are arranged in concentric cylinders around the beam line, and an endcap region, where the detecting elements are mounted on disks orthogonal to the beam axis.

Since all material between the IP and the calorimeters degrade the resolution of the measured energy, the three sub-detectors must be designed so that they minimize the quantity of matter to be crossed by the particles, and also to support the high-radiation conditions.

Pixel detector

The innermost tracking subsystem of the ID is the semiconductor pixel detector [50]. The layout of the pixel detector and an assembly view of a pixel module are shown in Fig. 3.5. The detector is designed to provide at least three precise measurement points for tracks with $|\eta| < 2.5$. The pixel detector consists of three concentric barrel layers placed at radii of 50.5, 88.5, and 122.5 mm around the beam axis covering the central region up to $|\eta| = 1.9$ and three endcap disks placed at $|z|$ positions of 495, 580, and 650 mm in each direction along the beam axis from the IP, extending the total coverage up to $|\eta| = 2.5$.

Each module has an active region with an area of 16.4 mm $\times$ 60.8 mm and 250 μm thickness. The sensor is composed of an oxygen-rich n-type bulk segmented into 47232 n$^+$-in-n pixels whose typical size is 50 μm $\times$ 400 μm. The direction
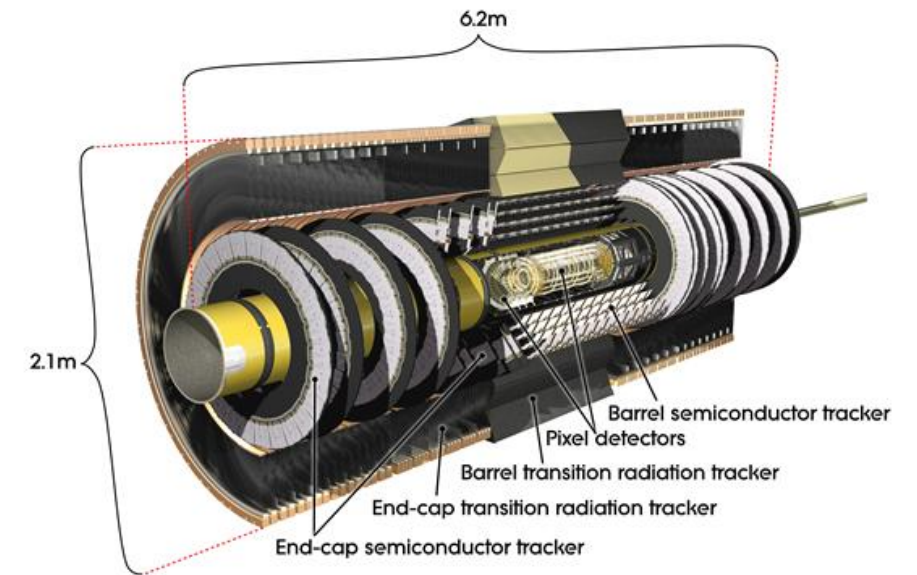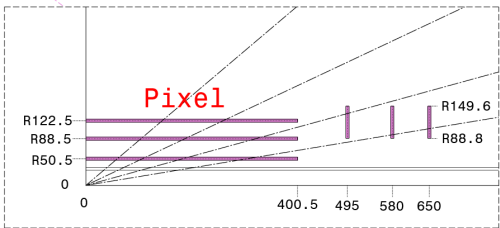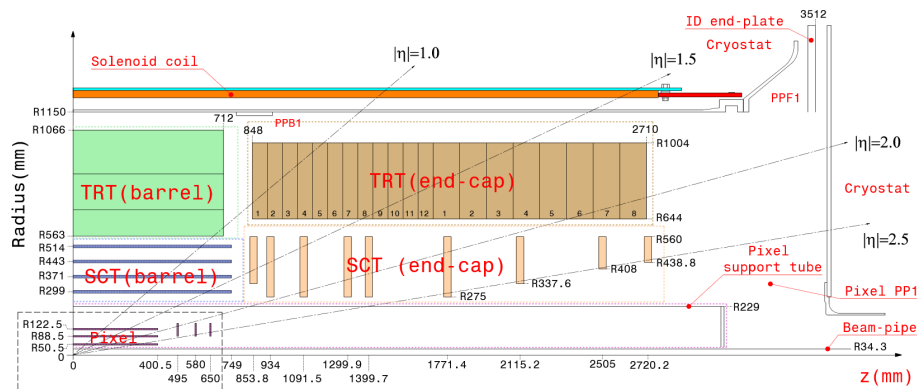
(a)

(b)

Figure 3.4: Overview (a) and a layout (b) of the ATLAS inner detector.

defined by the shorter pitch is the local x-coordinate on the module and corre-
sponds to the high precision measurement in the r$-\phi$ plane. The longer pitch is
oriented approximately along the z direction in the barrel and radially in the end-
caps. A module is read out by 16 radiation-hard front-end chips bump-bonded to
the sensor. In order to cover the clearance region between front-ends, some pixels
have a longer size of 600 μm or are ganged in pairs to a single read-out channel.
The charge collected in each pixel is measured with 8-bit dynamic range using
the Time over Threshold (ToT) technique: the width of the discriminator output is
measured by counting the number of 25 ns clock cycles during which the signal
is above a threshold. Since the ToT is a sub-linear function of the charge, it gives
precise information about the ionization losses of charged particles crossing pixel
modules.

The pixel detector is the most important detector used for the identification and
reconstruction of secondary vertices. Moreover, it provides an excellent spatial
resolution for reconstructing primary vertices even in the presence of multiple
interactions in *pp* collisions. Its intrinsic spatial resolution is 10 μm (r-ϕ) and 115
μm (z) in the barrel, and 10 μm (r-ϕ) and 115 μm (r) in the disks.
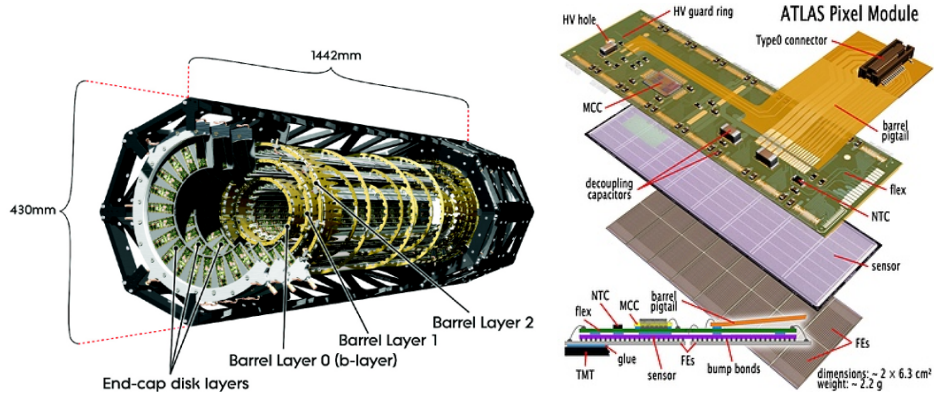
Figure 3.5: Schematic view of the active region of the ATLAS pixel detector (left)
and an assembly view of a pixel module (right)

Semiconductor tracker

The SCT [51,52,53] is composed of a barrel and two endcap sections. The barrel has
four coaxial cylindrical layers at radii 299, 371, 443, and 514 mm around the beam
axis in the radial direction, covering the central region up to |η| = 1.1. Each endcap
region has nine disks of different sizes located between 854 and 2720 mm from the
IP along the beam axis, providing a total coverage up to |η| = 2.5. The detector is
segmented in 4088 modules: there are 2112 (1976) rectangular (trapezoidal) shaped
modules in the barrel (endcap) region, covering a total surface of 63 m^2. Figure 3.6
shows a photograph of the SCT barrel detector and an assembly view of an SCT
module.

The modules are made of silicon-strip devices that arrange the strips parallel to the beam axis in the barrel and radially in the endcap, providing a precise measurement in the r-ϕ plane. The modules consist of one or two pairs of single-sided p-in-n microstrip sensors. The sensors are divided into 768 AC-coupled strips with a constant pitch of 80 μm in the barrel, while in the endcap it varies from 56.9 to 94.2 μm due to the trapezoidal shape. Two layers of sensors are rotated with respect to one another by a 40 milliradian stereo angle. This ensures that a charged particle coming from the IP typically crosses eight strip sensors, contributing to the precise measurement of momentum, impact parameter and vertex position. The position resolution is $\sim$ 17 μm in lateral plane (r-ϕ) and $\sim$ 580 μm in longitudinal direction.

A hit is registered only if the pulse height exceeds a preset threshold, which normally corresponds to a charge of 1 fC. The charge measured in the strip is stored for a period of $\sim$ 3.2 μs and used for tracking if the trigger indicates that the event should be considered in more detail. Each module is read out by 12 identical 128-channel front-end ASICs, resulting approximately in 6.3 million readout channels.
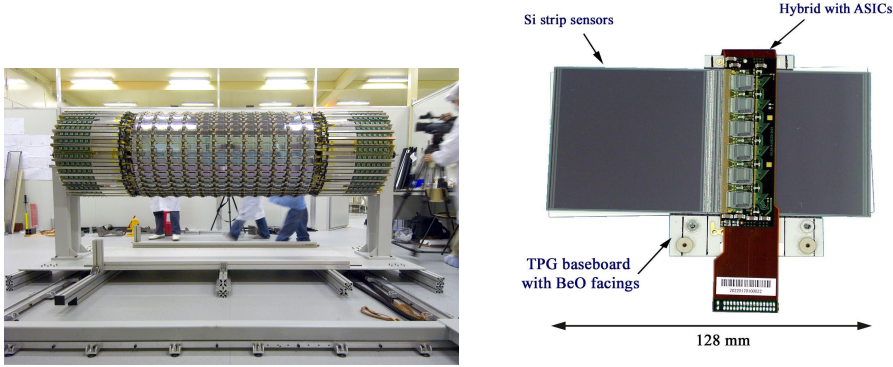
Figure 3.6: Photograph of the SCT barrel detector (left) and an assembly view of an SCT module (right).

Transition radiation tracker

The TRT [54, 55, 56] is a straw-tube tracker. Figure 3.7 shows photographs of the TRT barrel and endcap modules.

Transition radiation is a phenomenon that a relativistic particle emits photons when it crosses a boundary between two media with different dielectric constants. When a relativistic particle passes through the boundary between vacuum and the medium, it emits photons with the energy (W_{TR}),

$$W_{TR} = \frac{1}{3}\alpha\omega_p\gamma, \tag{3.7}$$

where α, γ and ω_p are the fine structure constant, the Lorentz boost factor of the particle and a plasma frequency, respectively. The plasma frequency ω_p is defined
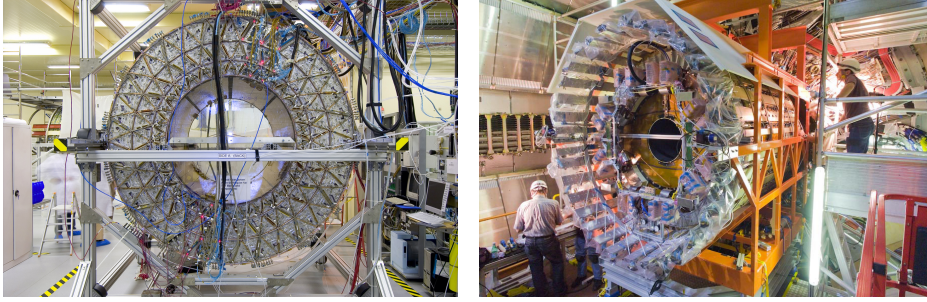
Figure 3.7: Photographs of the TRT barrel (left) and endcap (right) modules.

by

$$\omega_p = \sqrt{\frac{N_e e^2}{\epsilon_0 m_e}}, \tag{3.8}$$

where N_e, ϵ_0 and m_e are the electron density of the medium, the dielectric constant, and the electron mass, respectively. As shown in Eq. 3.7, an emitted energy is proportional to a Lorentz boost factor of a charged particle. Therefore, the transition radiation is used for the identification of electrons to distinguish them from heavier charged particles.

The diameter of drift tube is 4 mm, and it is made from wound Kapton and reinforced with thin carbon fibers. The anode wire is formed by a gold-plated tungsten whose diameter is 31μm diameter. The cathode is a tube made form carbon, aluminum and Kapton, and it has an approximately 60 μm thickness. The tubes are filled with $Xe/CO_2/O_2$ gases in the proportions of 70/27/3 %. The xenon gas is used for a good X-ray absorption, and CO_2 and O_2 are used to increase the electron drift velocity and for a photon-quenching.

When a charged particle traverses the TRT, it ionizes the gas inside the tubes. The electrons generated by the ionization drift towards the wire, where they are amplified and read out. The front-end electronics samples the incoming signal in 24 time bins of 3.12 ns and compare it against a threshold corresponding to 300 eV as shown in Fig. 3.8. The TRT is designed so that charged particles with $p_T >$ 0.5 GeV and $|\eta| < 2.0$ cross at least 32 straws, except in the transition region (0.8 $< |\eta| < 1.2$) where this number decreases to at least 22 straws [1]. This large number of tracking points allows almost continuous tracking that improves the precision of the momentum measurement.

The spaces between the straws are filled with polymer fibers (barrel) and foils (endcaps) to create transition radiations. Typical photon energies are 5–30 keV. These soft X-rays can be absorbed by the xenon gas, depositing additional energy in the gas and leading to significantly higher readout signals. Such signals are

---

[1]See Fig. 8.10.

detected by comparing them against an additional high threshold of 6 keV that is sampled in three 25 ns time bins alongside the pattern described above.
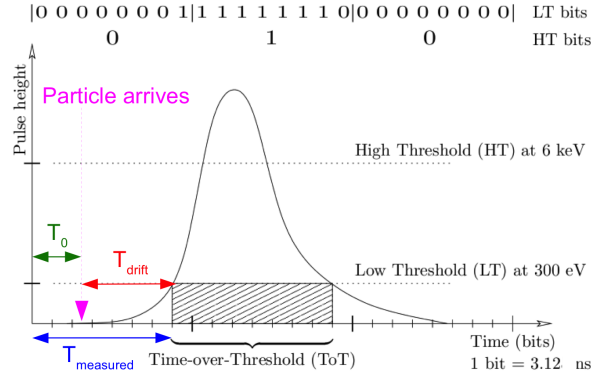
Figure 3.8: Signal pulse generated by ionized electrons and transition radiation photons.

The TRT detector is composed of a barrel and two endcap sections. The TRT barrel consists of three layers (Type-1, Type-2 and Type-3) of 32 modules each. The straws are parallel to the beam axis, and they occupy the region between $563 < r < 1066$ mm and $|z| < 712$ mm, corresponding to a coverage of $|\eta| < 0.7$. The innermost nine layers in $|z| < 400$ mm of the Type-1 module are not active to reduce the occupancy. The wires are electrically split in the center and are read out at both ends, thus reducing the occupancy but doubling the number of electronic channels. There are two types of detectors for the endcap TRT, called Type-A and Type-B. There are total 160 layers of straws in each TRT endcap along the z-axis, and each layer contains 768 radially oriented straws of 37 cm length with uniform azimuthal spacing but stepped, layer to layer, in ϕ.

3.2.4 Calorimeter system

The ATLAS calorimeter system [57] is placed outside the solenoid magnet. It consists of several non-compensating sampling calorimeters. It has a ϕ-symmetric coverage around the beam axis spanning the region $|\eta| < 4.9$ with a varying granularity in $\eta \times \phi$. The electromagnetic (EM) calorimeter has a high granularity that is necessary for precise measurements of the energy of electrons and photons. It also

contributes to measure the energy of hadrons in jets. The hadronic calorimeter has a coarser granularity, but it is sufficient to reconstruct hadronic jets and missing transverse momentum.

There are four calorimeters in ATLAS detector: the liquid argon (LAr) EM calorimeter [58] ($|\eta| < 3.2$), the tile hadronic calorimeter [59] ($|\eta| < 1.7$), the LAr hadronic endcap calorimeters [60] ($1.5 < |\eta| < 3.2$), and the LAr forward calorimeter [61] ($3.1 < |\eta| < 4.9$). The overall system is illustrated in Fig. 3.9.
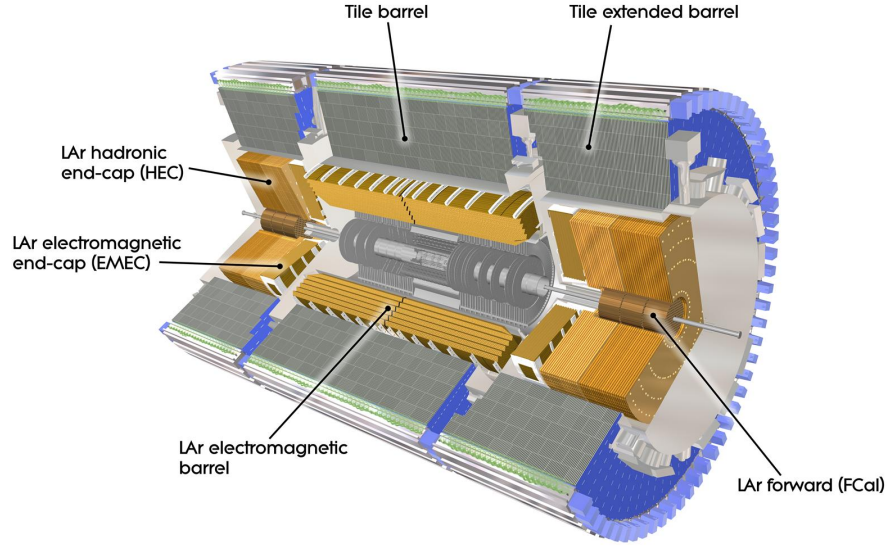
Figure 3.9: Cut-away view of the ATLAS calorimeter system.

3.2.5 The electromagnetic calorimeter

Figure 3.10 shows a cross-section of the EM calorimeter. It is a lead-LAr detector with accordion-shaped Kapton electrodes and lead absorber plates. The accordion geometry provides a full coverage in the ϕ direction without azimuthal cracks and a fast extraction of the signal at the rear or at the front of the electrodes.

The accordion geometry allows it to have several active layers. The EM calorimeter is therefore segmented into three longitudinal layers in the region $|\eta| < 2.5$. Figure 3.11 shows a schematic view of a barrel module of the EM calorimeter. The first layer is equipped with narrow strips in η with a pitch of ~ 4 mm, and has a depth of $\sim 6\ X_0$ including dead material and the pre-sampler described below. It works as a pre-shower detector, helping to identify particles and providing a precise position measurement in η. The second layer is transversely segmented into square towers with a total depth of $\sim 24\ X_0$. The last layer has a

coarser granularity in η with a depth between 2 X_0 and 12 X_0. For the region $|\eta| > 2.5$, the EM calorimeter is segmented into two longitudinal layers with a coarse lateral granularity. For the region $|\eta| < 1.8$, the EM calorimeter is preceded by a pre-sampler detector with a depth of $\sim 2X_0$ installed behind the cryostat. The pre-sampler consists of an active LAr layer of depth 1.1 (0.5) cm in the barrel (end-cap) region. The pre-sampler is designed to estimate and correct energy losses by the interaction with material upstream of the EM calorimeter. A large amount of material is situated in front of the EM calorimeter in the region $1.37 < |\eta| < 1.52$, resulting in reduced energy and degraded position resolutions for electrons and photons. Table 3.2 summarizes the parameters of the EM calorimeter and Fig. 3.12 shows the cumulative amounts of material in units of X_0 and as a function of $|\eta|$ in front of and in the EM calorimeters.

The energy resolution of the EM calorimeter (ΔE) is given by

$$\frac{\Delta E}{E} = \frac{11\%}{\sqrt{E \text{ GeV}}} \oplus 0.4\%, \tag{3.9}$$

where E is an energy measured in the EM calorimeter. The first term describes the statistical fluctuations in the sampling material and the constant second term describes systematic uncertainties from an inhomogeneous material distribution.
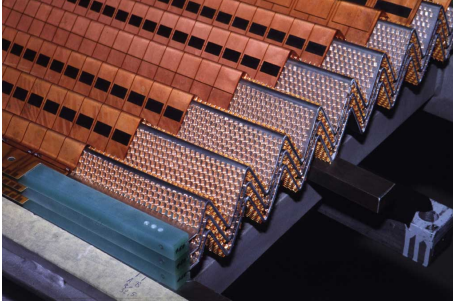
Figure 3.10: Cross-section of the LAr electromagnetic calorimeter.
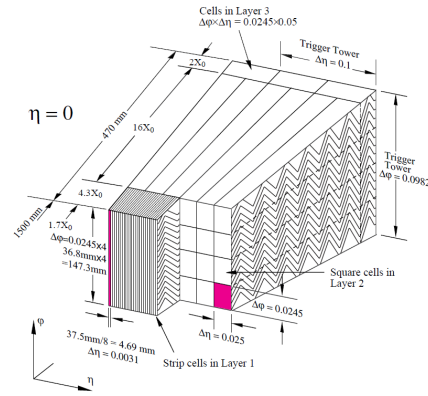
Figure 3.11: Schematic view of a barrel module of the LAr EM calorimeter.

3.2.6 Hadronic calorimeter

The hadronic calorimeter mainly contributes to reconstruct jets and missing transverse momentum. The ATLAS hadronic calorimeter consists of three types of detectors: the tile calorimeter (TileCal), the LAr hadronic endcap (HEC), and the forward calorimeter (FCal). They cover different η ranges and have granularity

|	**Barrel**		**End-cap**	
Number of layers and $|\eta|$ coverage				
EM pre-sampler	1	$|\eta| < 1.52$	1	$1.5 < |\eta| < 1.8$
EM calorimeter	3	$|\eta| < 1.35$	2	$1.375 < |\eta| < 1.5$
	2	$1.35 < |\eta| < 1.475$	3	$1.5 < |\eta| < 2.5$
			2	$2.5 < |\eta| < 3.2$
LAr hadronic end-cap calorimeter			4	$1.5 < |\eta| < 3.2$
LAr forward calorimeter			3	$3.1 < |\eta| < 4.9$
Tile calorimeter	3	$|\eta| < 1.0$	3	$0.8 < |\eta| < 1.7$
Granularity $\Delta\eta \times \Delta\phi$ in η range				
EM pre-sampler	0.025×0.1	$|\eta| < 1.52$	0.025×0.1	$1.5 < |\eta| < 1.8$
EM calorimeter 1st layer	$0.025/8 \times 0.1$	$|\eta| < 1.40$	0.050×0.1	$1.375 < |\eta| < 1.425$
	0.025×0.025	$1.40 < |\eta| < 1.475$	0.025×0.1	$1.425 < |\eta| < 1.5$
			$0.025/8 \times 0.1$	$1.5 < |\eta| < 1.8$
			$0.025/6 \times 0.1$	$1.8 < |\eta| < 2.0$
			$0.025/4 \times 0.1$	$2.0 < |\eta| < 2.4$
			0.025×0.1	$2.4 < |\eta| < 2.5$
			0.1×0.1	$2.5 < |\eta| < 3.2$
EM calorimeter 2nd layer	0.025×0.025	$|\eta| < 1.40$	0.050×0.025	$1.375 < |\eta| < 1.425$
	0.075×0.025	$1.40 < |\eta| < 1.475$	0.025×0.025	$1.425 < |\eta| < 2.5$
			0.1×0.1	$2.5 < |\eta| < 3.2$
EM calorimeter 3rd layer	0.050×0.025	$|\eta| < 1.35$	0.050×0.025	$1.5 < |\eta| < 2.5$
LAr hadronic end-cap calorimeter			0.1×0.1	$1.5 < |\eta| < 2.5$
			0.2×0.2	$2.5 < |\eta| < 3.2$
LAr forward calorimeter 1st layer			3.0×2.6	$3.15 < |\eta| < 4.30$
			0.75×0.65	$3.10 < |\eta| < 3.15$
			0.75×0.65	$4.30 < |\eta| < 4.83$
LAr forward calorimeter 2nd layer			3.3×4.2	$3.24 < |\eta| < 4.50$
			0.825×1.05	$3.20 < |\eta| < 3.24$
			0.825×1.05	$4.50 < |\eta| < 4.81$
LAr forward calorimeter 3rd layer			5.4×4.7	$3.32 < |\eta| < 4.60$
			1.35×1.175	$3.29 < |\eta| < 3.32$
			1.35×1.175	$4.60 < |\eta| < 4.75$
Tile calorimeter 1st, 2nd layer	0.1×0.1	$|\eta| < 1.0$	0.1×0.1	$0.8 < |\eta| < 1.7$
Tile calorimeter 3rd layer	0.2×0.1	$|\eta| < 1.0$	0.2×0.1	$0.8 < |\eta| < 1.7$

Table 3.2: Main parameters of the ATLAS calorimeter system.
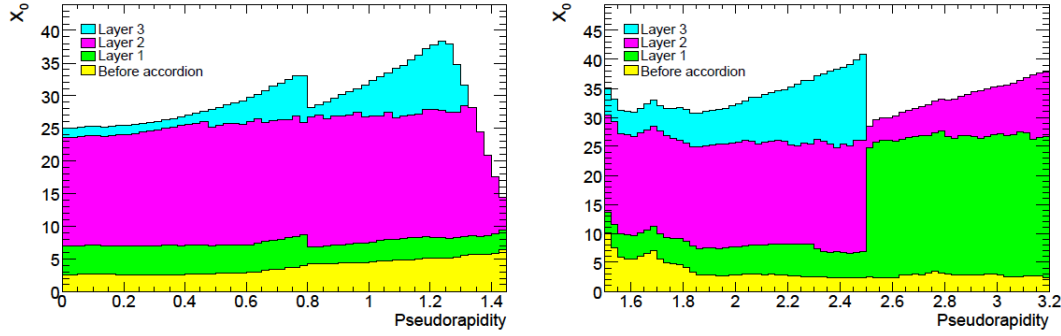
Figure 3.12: Cumulative amounts of material in units of X_0 as a function of $|\eta|$ in front of and in the EM calorimeters. The left (right) figure shows the cumulative amounts of material in the barrel (endcap) region.

suited to each regions. The granularity and coverage of the hadronic calorimeters are shown in Table 3.2. Figure 3.13 shows the cumulative amount of material in units of interaction length as a function of $|\eta|$ in front of and in the electromagnetic (hadronic) calorimeters.
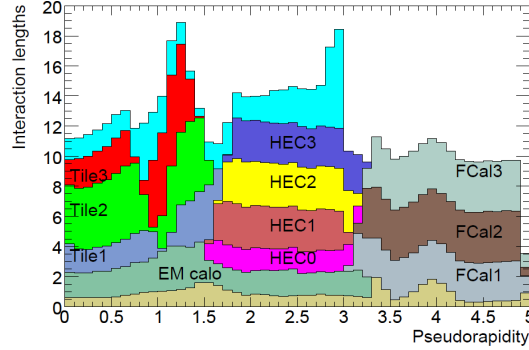
Figure 3.13: Cumulative amounts of material in units of interaction length as a function of $|\eta|$ in front of and in the electromagnetic (hadronic) calorimeters. The total amount of material in front of the first active layer of the muon spectrometer is also shown by a light-blue filled area.

Tile calorimeter

The TileCal is a sampling calorimeter that uses 14 mm thick steel plates as absorber material and 3 mm thick plastic scintillators as active medium. It is placed directly outside of the EM calorimeter in the central barrel region. Figure 3.14 and

3.15 show a schematic view of the TileCal and a photograph of scintillating tiles, respectively. The central barrel part covers the region $|\eta| < 1.0$ and two extended barrels cover the region $0.8 < |\eta| < 1.7$. It is longitudinally segmented in three layers with approximately 1.5, 4.1, and 1.8 interaction length for the barrel and 1.5, 2.6, and 3.3 interaction length for the extended barrel. Two sides of the scintillating tiles are read out by wavelength shifting fibers into two separate photomultiplier tubes (PMTs). This provides a very fast signal and is used in the trigger system.
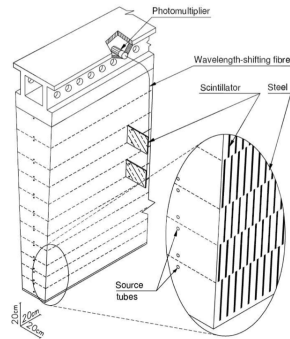
Figure 3.14: Schematic view of the Tile-Cal.

Figure 3.15: Photograph of scintillating tiles.

LAr hadronic end-cap calorimeter

The hadronic calorimeter is extended in the region $1.5 < |\eta| < 3.2$ by the HEC that is a copper/LAr sampling calorimeter with a flat-plate design. The copper-plate acts as absorber, while the LAr works as active medium. The LAr is used due to its high radiation tolerance, which is needed in the forward regions.

The HEC consists of two wheels in each end-cap: a front wheel (HEC1) and a rear wheel (HEC2). The wheels are cylindrical with an outer radius of 2030 mm. Each of four HEC wheels consists of 32 identical modules. Figure 3.16 shows a schematic view of a module of the HEC. The modules of the front wheels are made of 24 copper plates of 25 mm thick. In the rear wheels, the module consists of 16 copper plates of 50 mm thick. The gap between the plates is 8.5 mm thickness.

LAr forward calorimeter

The FCal is integrated into the end-cap cryostats covering the region $3.1 < |\eta| < 4.9$. The FCal has approximately ten interaction length and consists of three modules in each endcap: the electromagnetic calorimeter with copper as its absorbing material (FCal1) and the hadronic calorimeters with tungsten as their absorbing
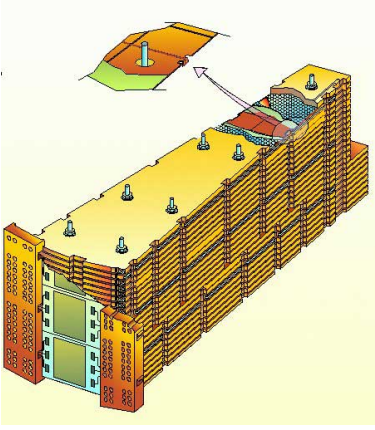
Figure 3.16: Schematic view of the HEC.
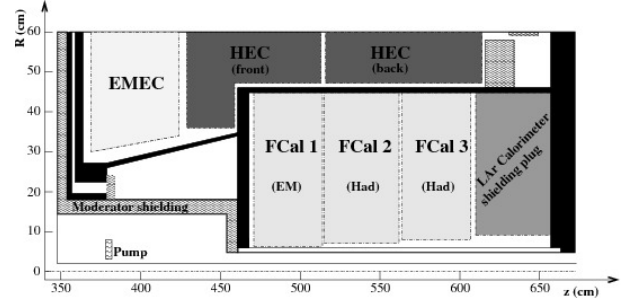
Figure 3.17: Schematic view of the FCal.

material (FCal2 and FCal3). Figure 3.17 shows a schematic view of the FCal. In each module, the calorimeter consists of a metal matrix with regularly spaced longitudinal channels filled with the electrode structure. The gaps between the rod and matrix are filled with LAr, resulting in a faster signal with a drift time of 60 ns, while for the hadronic ones it scales with the gap size.

3.2.7   Muon spectrometer

The muon spectrometer (MS) [62] is the outermost part of the ATLAS detector. It is designed to detect charged particles that traverse the calorimeters and to measure their momenta in the region $|\eta| < 2.7$. The MS can identify muons with momenta > 3 GeV, and the momentum resolution ranges between 3 and 4 % for $10 < p_T < 500$ GeV and 10 % for $p_T \sim 1$ TeV. The measurement is based on the magnetic deflection of muon tracks in the large superconducting air-core toroid magnets. The chambers are arranged such that particles emerging from the IP can traverse three stations of chambers. The magnetic field in the region $|\eta| < 1.0$ is generated solely by the barrel toroids, while it is served by the endcap magnets in the region $1.4 < |\eta| < 2.7$. The MS is also designed to trigger on events with muons traversing the calorimeters in the region $|\eta| < 2.4$. The region $1.0 < |\eta| < 1.4$ is referred to as transition region where the magnetic field is a combination of the fields from both the barrel and endcap toroids.

The MS is formed by a barrel and two endcap regions. The barrel chambers form three cylinders concentric with the beam direction, placed at radii of approxi-

mately 5, 7.5, and 10 m away from the beam axis, covering the region $|\eta| < 1$. In the two endcap regions, the chambers are arranged in four disks located at $|z| \sim 7.4$, 10.8, 14, and 21.5 m from the IP and concentric with the beam axis, covering the region $1 < |\eta| < 2.7$. The MS provides a nearly full coverage except in the region $\eta \sim 0$ where a gap is left open for the passage of cables and services of the ID, central solenoid and the calorimeters.

The MS is equipped with four different kind of chambers: monitored drift tube chambers (MDT), cathode strip chambers (CSC), resistive plate chambers (RPC), and thin gap chambers (TGC). The first two are used for precise measurements of muon tracks, while the other two are used for the trigger and data acquisition system. They are illustrated in Fig. 3.18.

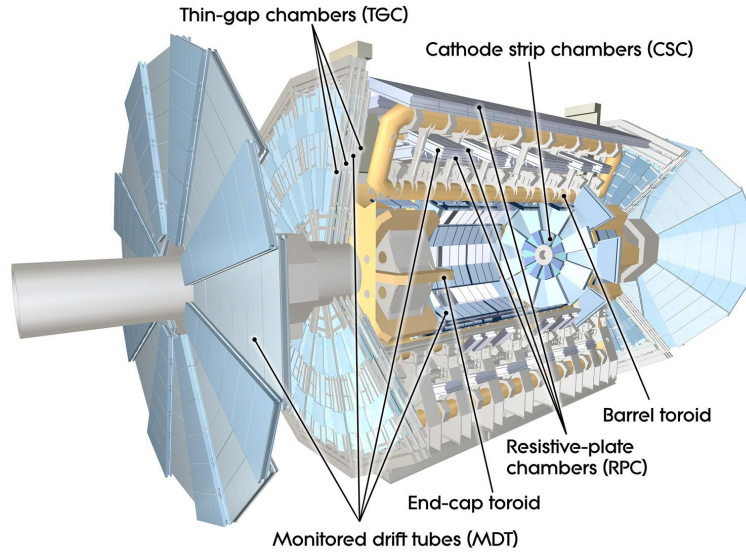Figure 3.18: Cut-away view of the ATLAS muon system.

The high-precision tracking chambers

The high-precision tracking chambers are built out of two kinds of detectors: MDT and CSC. The MDT chambers cover the region $|\eta| < 2.0$, while the CSC chambers cover the region $2.0 < |\eta| < 2.7$. The precise measurement of the muon tracks is made in the r-z projection. The z coordinate is measured in the barrel,

while the radial coordinate is measured in the transition and endcap regions. A measurement of ϕ is also obtained by the CSC in the forward region.

The MDT chambers are made of aluminum drift tubes of 30 mm diameter filled with Ar/CO_2 gases in the proportions of 93/7 % at a pressure of 3 bar. A 50 μm diameter tungsten-rhenium (W-Re) wire is used as an anode. The wire is kept at 3080 V, and the maximum drift time from the wall to the wire in the tube is about 700 ns. There are 1150 MDT chambers; 592 of them are located in the barrel and 558 at the endcap regions. The chambers consist of two groups of tube layers (multilayers) that are separated by a mechanical spacer. In the innermost layer, each multilayer consists of 4 tube layers, while in the middle and outer layer, it consists of three tube layers. The mechanical structure of a MDT chamber is shown in Fig. 3.19. The average resolution in the z direction is about 80 μm per tube, or $\sim$ 35 μm per chamber.

The CSC system is formed by two disks with eight chambers each, segmented in ϕ into large and small chambers as shown in Fig. 3.20. It has 32 chambers with a total area of 65 m^2. The chambers are operated at 900 V and take up the radial space between 881 mm and 2081 mm. The CSC is a multiwire proportional chamber filled with Ar/CO_2 gases in the proportions of 80/20 %. The anode wires are made of gold-plated tungsten with 3 % rhenium and have a diameter of 30 μm. The cathode planes are segmented into strips in orthogonal directions, which allows both coordinates to be measured: the cathode with the strips perpendicular to the wires provides the precise coordinate, while the one parallel to the wires provides the transverse coordinate. The resolution of a chamber is 40 μm in the bending plane and about 5 mm in the transverse plane. Each chamber has a similar configuration to the multilayer of the MDT system with four wire planes but with a finer granularity, resulting in four independent measurements in η and ϕ along each track. A four layer chamber consists of five flat rigid panels, each made of sheet of polyurethane foam and two 0.82 mm thick copper-clad laminates, where the 17 μm thick copper cladding forms the cathodes. The electron drift times are less than 40 ns, which results in a timing resolution of about 7 ns per plane.

The trigger chambers

The trigger chambers are constructed out of two kinds of detectors: RPC in the barrel and TGC in the endcap region. They complement the high-precision tracking chambers with a system of fast trigger providing information within a few tens of nanoseconds on muon tracks traversing the detector. Three layers of trigger chambers are arranged in the barrel, while a fourth layer is added in the endcap region. In the barrel, the middle layer of the MDT is sandwiched by two layers of RPC, while the third RPC layer is placed close to the outer MDT layer. In the endcap region, one TGC layer is in front of the second MDT wheel, while two layers are behind it. The fourth TGC layer of the endcap region is placed in front of the innermost tracking layer. The whole system is illustrated in Fig. 3.21.

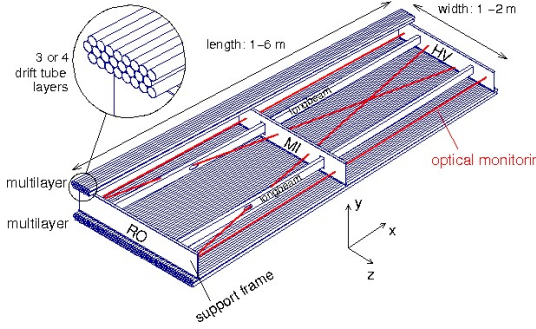The RPC is a gaseous parallel electrode-plate detector covering the region

Figure 3.19: Mechanical structure of a MDT chamber showing the multi-layers and the alignment system.
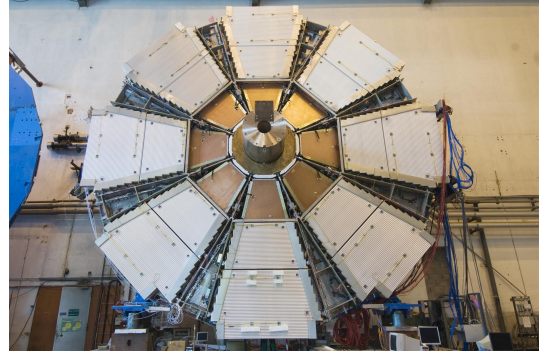
Figure 3.20: Photograph of a CSC endcap showing the eight small and eight large chambers.

$|\eta| < 1.05$. A RPC chamber is formed by two rectangular units contiguous to each other. Each unit is composed of two independent detector layers filled with $C_2H_2F_4$/Iso-C_4H_{10}/SF_6 gases in the proportions of 94.7/5/0.3 %, and is readout by two orthogonal sets of pick-out strips. A detector consists of two resistive plates made of phenolic-melaminic plastic laminate, kept at a distance of 2 mm by insulating spacers. The electric field between the plates is 4.9 kV/mm. The signal is read out by two metallic strips that provide a measurement in both the z and ϕ coordinates, with a spatial resolution of 10 mm and a timing resolution of 1.5 ns.

The TGC is a multiwire proportional chamber covering the region $1.05 < |\eta| < 2.4$. Seven layers of TGC arranged in one triplet and two doublets complement the middle layer of the MDT in the endcap region, while only two layers complement the inner layer. A chamber is formed by a detector layer containing a wire plane and two cathodes, and it is filled with CO_2/n-pentane gases in the proportions of 55/45 %. The wire and the cathode are separated at a distance of 1.4 mm, while the distance between wires is 1.8 mm. The wires have a diameter of 50 μm and are kept at 2900 V, while the cathode planes consist of 1.6 mm thick FR4 plates, grafite coated on the inside and copper cladding on the other side. The wires are placed parallel to the MDT tubes, while the cathode strips are arranged radially. The spatial resolution of the TGC is 2 to 6 mm in the radial direction, and 3 to 7 mm in the ϕ direction, and the timing resolution is $\sim$ 4 ns.
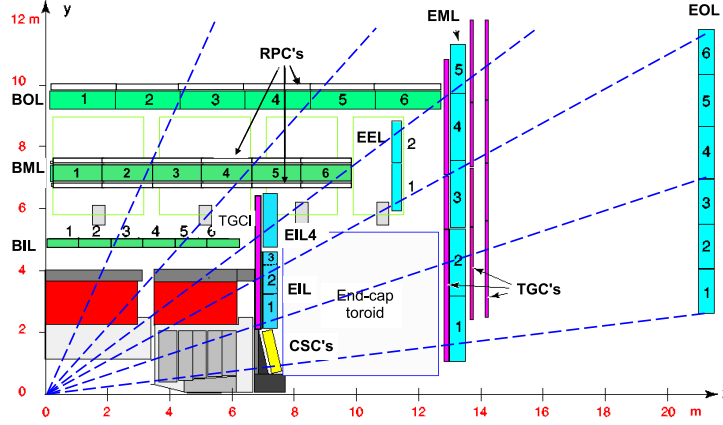
Figure 3.21: Schematic view of the muon trigger system showing the positions of the RPC layers in the barrel and the TGC layers in the endcap region.

3.2.8 Luminosity detector

Figure 3.22 shows a schematic view of the ATLAS luminosity detectors. There are two primary detectors to measure the luminosity [63]: the luminosity measurement using Cerenkov integrating detector (LUCID) and the beam conditions monitor (BCM). Both LUCID and BCM can measure the bunch-by-bunch luminosity.

The LUCID detector

The LUCID detector is a Cerenkov detector, located at a distance of $|z| = 17$ m from the IP and at a radial distance of 10 cm from the beam line, covering the range $5.61 < |\eta| < 5.93$. The LUCID detector measures the integrated luminosity and provides online monitoring of the instantaneous luminosity and beam conditions by detecting inelastic pp scattering. In order to determine the luminosity, the number of interactions per beam-crossing has to be well known, therefore, the LUCID is designed so that the number of interactions in a bunch-crossing can be proportional to the number of particles detected.

The LUCID detector is composed of twenty aluminum tubes filled with C_4F_{10} gas. The tubes are 1.5 m long and 15 mm in diameter. They surround the beam-pipe and point toward the IP. When a particle traversing the tube emits Cerenkov light, it is reflected in the tube walls and measured by the PMTs. The charge from the PMTs is used to measure the number of particle per tube, while the timing response provides a measurement of each bunch crossing.

The BCM detector

The BCM comprises one detector station on either side of the ATLAS detector at $|\eta| = 4.2$. The stations are located 1.84 m away from the IP and are made of four modules, which are arranged in a cross pattern around the beam axis at a radius of about 55 mm. The BCM is designed for bunch-by-bunch luminosity measurements and monitoring the beam background conditions within the ID and to protect the ATLAS detector from damage due to severe beam losses. The BCM can distinguish particles created in *pp* collisions from beam-background particles based on their detection time. The BCM modules are made of diamond sensors that are placed between two electrodes. The sensor material was chosen due to its radiation hardness and its fast signal rise time. A charged particle traversing the sensor ionizes the diamond and generates a signal that is amplified on the module and then transmitted for digitization to the readout electronics.
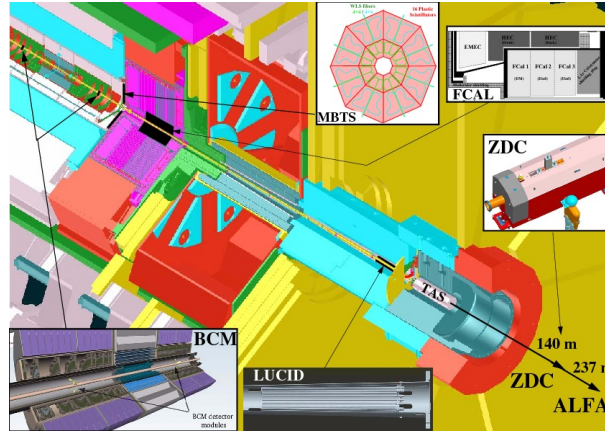
Figure 3.22: Schematic view of the ATLAS luminosity detectors.

3.2.9   Trigger system

The ATLAS experiment is designed to receive data at a rate of ~ 40 MHz, but the data acquisition system can only commit data to a permanent storage at a rate of a few hundreds Hz. In order to select interesting data from a large number of incoming events, the ATLAS trigger system is divided into three levels: level−1 (L1), level−2 (L2) and event filter (EF). The last two are also called as high-level triggers (HLT). The L1 trigger is implemented in the detector and works with the

hardware, and the HLT use computers and network hardwares. Figure 3.23 shows the three-level trigger and data acquisition systems of the ATLAS experiment.

The L1 trigger is required to make a decision within a fixed time of less than 2.5 μs and to lessen the trigger rate to $\sim$ 75 kHz. The L2 trigger uses the L1 information as a seed. The L2 trigger is required to reduce the trigger rate to $\sim$ 3.5 kHz within $\sim$ 40 ms. Finally, the information is passed to the EF trigger. The EF trigger uses offline analysis procedures to further select events down to a rate that can be recorded for subsequent offline analysis. It reduces the event rate to $\sim$ 200 Hz with an average event processing time of $\sim$ 4 s.

The HLT algorithms use the full granularity and precision of the data from the calorimeter, the MS and the ID to refine the trigger selection. The track information by the ID significantly improves the particle identification. The event selection at both L1 and L2 primarily uses inclusive criteria such as high$-p_\mathrm{T}$ objects above defined thresholds.

Figure 3.23: Three-level trigger and data acquisition systems of the ATLAS experiment.

Level-1 trigger

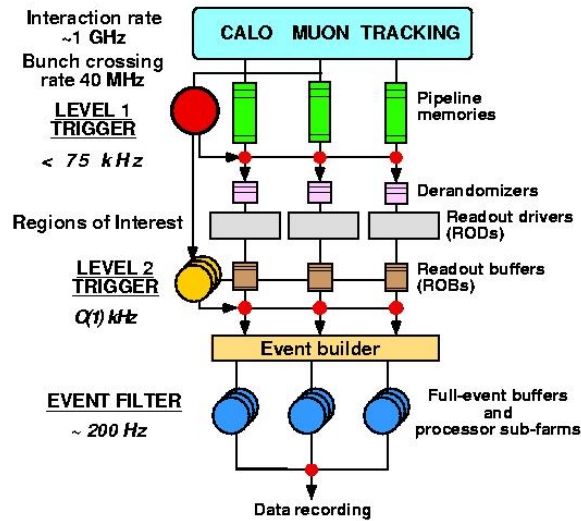The L1 trigger [64] mainly searches for isolated high$-p_\mathrm{T}$ electrons, photons, muons, and $\tau-$leptons decaying into hadrons to separate the desired rare processes from the dominant QCD multi-jet events. It also selects events with high$-p_\mathrm{T}$ jets, large missing transverse momentum.

As summarized in Fig. 3.24, the L1 trigger performs the initial event selection based on the information from the calorimeters and muon detectors. The level-1 muon trigger (L1Muon) is based on signals in the muon trigger chambers: RPC in the barrel and TGC in the end-caps. The trigger searches for patterns of hits consistent with high$-p_T$ muons originating from the IP. The level-1 calorimeter trigger (L1Calo) uses the information of energy deposition in the calorimeter to identify various types of high$-E_T$ objects. The L1Calo is a pipelined digital system designed to work with about 7000 analogue trigger towers of reduced granularities (0.1×0.1 in $\Delta\eta \times \Delta\phi$ in most regions, and larger at higher η regions). Results from both systems are processed by the central trigger processor (CTP). The CTP implements a trigger menu based on logical combinations of results from L1Calo and L1Muon. When an event is passed in the L1 trigger, the information for the geographical coordinate in η and ϕ of trigger objects (Region of Interest, RoI) are sent to the L2 trigger.
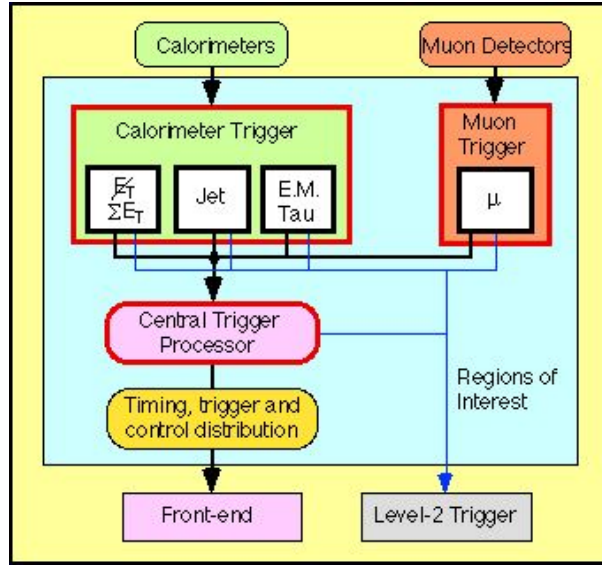
Figure 3.24: Block diagram of the L1 Trigger.

Leve$-$2 trigger

The L2 trigger [65] is a software-based system running on ~ 500 computing nodes, and can refine the event selection using the full granularity of the ATLAS detector. This refinement can be done for a restricted amount of data due to the limited processing speed and bandwidth. Therefore, the L2 trigger uses the L1 RoI as a seed. The L2 trigger can treat the full granularity of data from the calorimeter and muon systems around the RoI. In addition, the L2 trigger can include data from

the ID in its trigger decision. The L2 trigger can reduce the event rate from $\sim$ 75 kHz to $\sim$ 3.5 kHz by requiring isolation from surrounding environments to the trigger objects and tighter requirements on the p_T thresholds.

Event filter

The EF trigger [65] is an entirely software-based system running on $\sim$ 1800 computing nodes, reducing the event rate from $\sim$ 3.5 kHz to $\sim$ 200 Hz. It uses the the full granularity of the data from all sub-detectors, and it can reconstruct physics objects and analyze events with algorithms similar to those used in an offline analysis.

Chapter 4

Data and Monte Carlo Simulation

4.1 Data sample

The analysis presented is based on the *pp* collision data at $\sqrt{s} = 8$ TeV collected with the ATLAS detector at the LHC between March and December 2012.

4.1.1 Trigger

The data in the signal search sample were collected by a dedicated topological trigger named `EF_j80_a4tchad_xe70_tclcw_dphi2j45xe10`. The data collected by unprescaled single electron or muon triggers are also used for the study of background events. Table 4.1 shows the summary of triggers used in this analysis. The values in the name of each trigger stands for the cut-threshold.

Luminosity	Signal search sample	Electron	Muon
	`EF_j80_a4tchad_`	`EF_e24vhi_medium1`	`EF_mu24i_tight`
20.3 ± 0.6 fb^{-1}	`xe70_tclcw_dphi2j45xe10`	or	or
		`EF_e60_medium1`	`EF_mu36_tight`

Table 4.1: Summary of triggers used in this analysis

The trigger for the signal search sample requires:

- At least one jet with $p_{\mathrm{T}} > 80$ GeV.

- $E_{\mathrm{T}}^{\mathrm{miss}} > 70$ GeV.

- $\Delta\phi_{\mathrm{min}}^{\mathrm{jet}-E_{\mathrm{T}}^{\mathrm{miss}}} > 1$, where $\Delta\phi_{\mathrm{min}}^{\mathrm{jet}-E_{\mathrm{T}}^{\mathrm{miss}}}$ indicates the smallest azimuthal separation between the missing transverse momentum and either of the two highest-p_{T} jets with $p_{\mathrm{T}} > 45$ GeV.

The application of these requirements significantly suppresses the SM background processes, especially QCD multi-jet events, without loosing the signal acceptance

for the direct chargino production with a jet from ISR. Details on the signal trigger are described in Sec 8.1.1.

4.1.2   Luminosity and pile-up

The peak instantaneous luminosity reached 7.73×10^{33} cm^{-2}s^{-1} with a mean number of interactions per bunch crossing of 20.7 in the 8 TeV run. The cumulative luminosity recorded by the ATLAS detector and delivered by the LHC is shown in Fig. 4.1. The raw recorded data corresponds to an integrated luminosity of 21.3 fb^{-1}, falling to 20.3 fb^{-1} after application of basic data quality requirements. The 6% loss in term of integrated luminosity is a consequence of requiring all sub-detectors systems to be in good quality. For the 8 TeV data, the uncertainty on the integrated luminosity is ± 2.8 % based on the calibration procedure described in Ref [66,67].
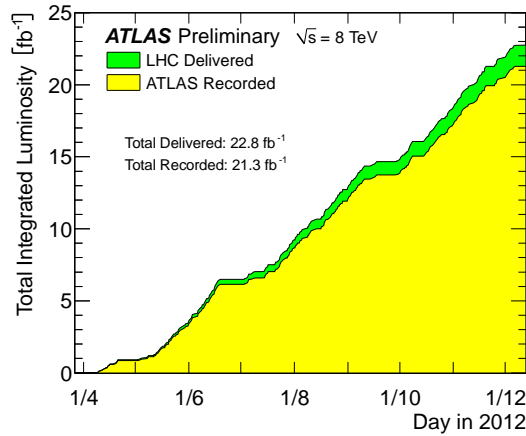
Figure 4.1: Cumulative luminosity versus time delivered by LHC (green), and recorded by ATLAS (yellow) during stable beams and for pp collisions at $\sqrt{s} = 8$ TeV.

When the luminosity gets increased, the detector performances and physics analyses are affected by the following pile-up effects:

- **In-time pileup :** Additional pp interactions occurring in the same bunch crossing, which contributes to distributing energy uniformly throughout the detector.

- **Outof-time pileup :** Additional pp interactions from other bunch crossings.

Figure 4.2 shows the luminosity-weighted distribution of the mean number of interactions per crossing for the 2011 and 2012 data. During 2011, the number of pp collisions per bunch crossing increased from 5 to 15, and during 2012 the number increased from 10 to almost 35.
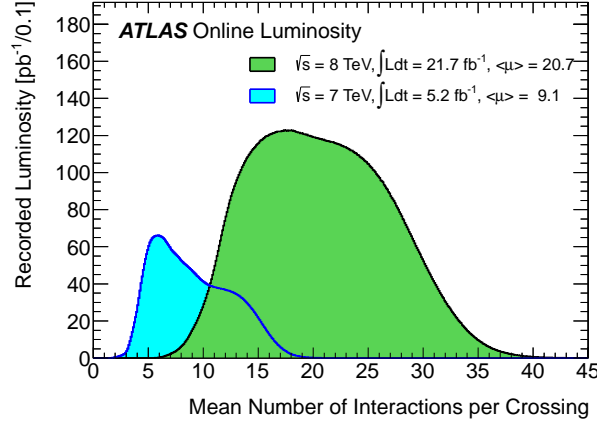
Figure 4.2: Luminosity-weighted distribution of the mean number of interactions per crossing for the 2011 and 2012 data.

4.2 Simulated sample

In order to develop and validate the analysis, Monte Carlo (MC) simulation samples have been used. The simulated samples were generated either with `CTEQ6L1` [68], `MSTW2008LO` [69] or `CT10` [70] parton distribution functions (PDF). The generation of the simulated samples includes the effect of multiple pp interactions per bunch crossing, and also the effect of the detector response to collisions from bunch crossings before and after the one containing the hard interaction. Minimum bias events are generated with `PYTHIA8` [71] configured with the AM2 tune [72] and the leading-order PDF set (`MSTW2008LO`). Events are reweighted so that the distribution of the number of pp collisions occurring in addition to the hard scatter process matches that observed in data. The detector response is modeled using the GEANT4 [73,74] simulation These samples are then reconstructed with the same algorithms used as for data. The simulated response is corrected for the small differences in efficiencies, momentum scales, and momentum resolutions between data and simulation, using scale factors and smearing techniques.

4.2.1 Signal Monte Carlo sample

Several benchmark signal points are prepared and used for this dissertation. The minimal AMSB model is characterized by four parameters: $m_{3/2}$, m_0, $\tan\beta$, and $\mu_{\rm H}$. A large value of 1 TeV is used for m_0 in order to prevent the appearance of a tachyonic slepton. The SUSY mass spectrum, the branching ratios and decay widths are calculated using the `Isasusy` Ver.7.80 [75]. The signal MC samples are produced using `HERWIG++` [76] with `CTEQ6L1` PDFs.

The mean lifetime of the chargino $\tau_{\tilde{\chi}_1^\pm}$ is set to a given value; charginos are forced to decay into $\tilde{\chi}_1^0 + \pi^\pm$ in the `Geant4` simulation by following the exponential

decay with $\tau_{\tilde{\chi}_1^\pm}$ in the rest frame. Two samples with $\tau_{\tilde{\chi}_1^\pm} = 0.3$ and 1.0 ns are generated for each signal point. Signal MC samples with different mean lifetimes are also obtained by applying event weights so that the distribution of the proper lifetime follows that for a given value of the mean lifetime. The event weight w is given by

$$w(\tau_{\tilde{\chi}_1^\pm}) = \prod_i^{n_{\tilde{\chi}_1^\pm}} \frac{\tau_0}{\tau_{\tilde{\chi}_1^\pm}} \exp\left[-t_i\left(\frac{1}{\tau_{\tilde{\chi}_1^\pm}} - \frac{1}{\tau_0}\right)\right], \tag{4.1}$$

where $n_{\tilde{\chi}_1^\pm}$, τ_0 and t_i are the number of charginos in the event, the chargino mean lifetime set in the simulation and the proper lifetime of i–th chargino, respectively. The signal samples with $\tau_{\tilde{\chi}_1^\pm} < (\geq)0.6$ ns are obtained by reweighting the sample of $\tau_{\tilde{\chi}_1^\pm} = 0.3(1.0)$ ns.

All the signal parameters and corresponding chargino masses $m_{\tilde{\chi}_1^\pm}$ and cross-sections are summarized in Table 4.2 and Fig. 4.3, respectively. Chargino–pair and chargino–neutralino associated production processes are identified using a jet with large transverse momentum from ISR. Corresponding diagrams are illustrated in Fig. 4.4. Signal samples are generated by requiring at least one truth–level jet with $p_T > 70$ GeV and $|\eta| < 5$. The selection efficiency after the application of this requirement is also shown in Table 4.2.

Signal cross-sections are calculated to next-to-leading order (NLO) in the strong coupling constant using `Prospino2` [77]. An envelope of cross-section predictions is defined using the 68% confidence level (CL) ranges of the `CTEQ6.6` [78] (including the α_S uncertainty) and `MSTW2008LO` PDF sets, together with variations of the factorization and renormalization scales by factors of two or one half. The nominal cross-section value is taken to be the midpoint of the envelope and the uncertainty assigned is half the full width of the envelope, closely following the PDF4LHC recommendations [79].

4.2.2   Background Monte Carlo sample

For the development of the analysis, MC samples of the SM background processes are also used. Table 4.3 and Fig. 4.5 shows the SM background processes with their cross-sections and their diagrams, respectively. The MC samples are generated as follows:

Z/W+jets production

A set of Z/W+jets MC samples has been produced with `ALPGEN` [80]. The `HERWIG` [81] is used for the parton shower (PS), fragmentation and hadronization, and `JIMMY` [82] is used to simulate the underlying events. The `ALPGEN` samples use the `CTEQ6L1` PDF set and the factorization and normalization scales are set to $\sqrt{M_{W/Z}^2 + \sum |p_T|^2}$, where $\sum |p_T|^2$ is the scalar sum of the p_T of the outgoing partons. W $(\to l\bar{\nu})$+jets and Z $(\to \nu\bar{\nu}, l^+l^-)$+jets samples are generated with up to six outgoing partons with LO

$m_{3/2}$[TeV]	$m_{\tilde{\chi}_1^\pm}$[GeV]	Cross-section [pb]	Filter efficiency
29.0	80.5	38.3	0.052
35.0	98.9	16.9	0.069
43.5	124.5	6.91	0.091
52.0	149.8	3.37	0.108
69.5	201.0	1.04	0.136
78.0	225.6	0.654	0.147
86.5	250.0	0.423	0.155
95.0	274.4	0.284	0.163
104.0	300.0	0.192	0.169
122.0	351.1	0.094	0.183
139.0	399.1	0.051	0.195
157.0	449.5	0.028	0.205
175.0	499.6	0.016	0.216

Table 4.2: Summary of AMSB signal parameters, chargino masses, and their NLO cross-sections with $m_0 = 1000$ GeV, $\tan\beta = 5$ and $\mu_H > 0$. The filter efficiencies for each sample are also shown.
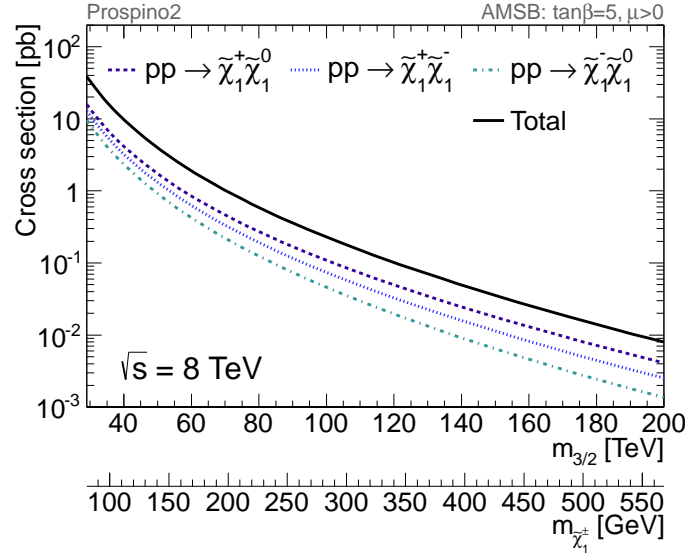
Figure 4.3: Cross-section of electroweak chargino production at $\sqrt{s} = 8$ TeV as a function of $m_{3/2}$.
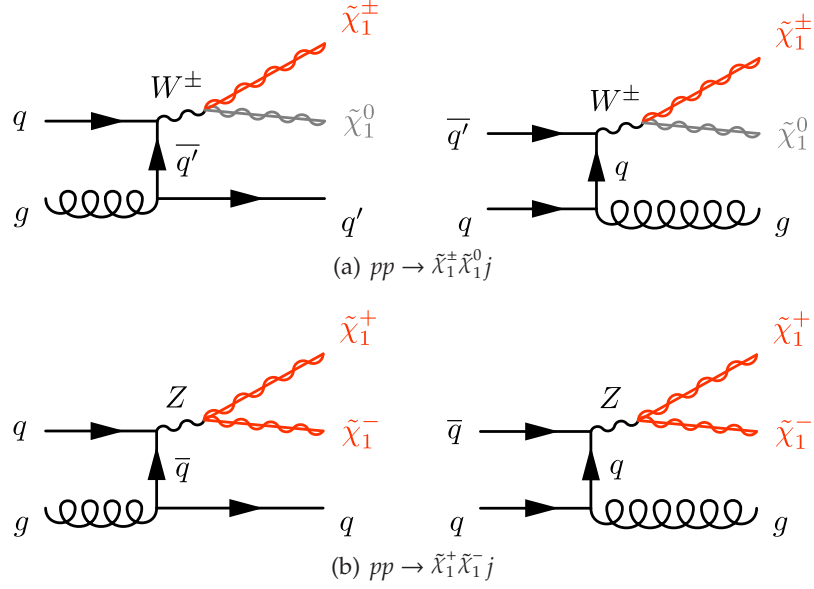
Figure 4.4: Diagrams of $\tilde{\chi}_1^{\pm}\tilde{\chi}_1^0$ (a) and $\tilde{\chi}_1^{+}\tilde{\chi}_1^{-}$ (b) production processes.

Production process	$\sigma\times$ Branching Ratio	Generator
QCD multi-jet events	73 mb	PYTHIA
$W(\rightarrow l\nu)$+jets	37 nb	ALPGEN
$Z(\rightarrow \nu\bar{\nu})$+jets	6.7 nb ($M_{\nu\bar{\nu}} > 40$ GeV)	ALPGEN
$Z/\gamma^*(\rightarrow l^+l^-)$+jets	3.7 nb ($M_{l^+l^-} > 40$ GeV)	ALPGEN
$t\bar{t}$	240 pb	POWHEG
single top	116 pb	AcerMC and MC@NLO

Table 4.3: The SM background processes with their cross-section times branching ratio. Generators used for each process are also shown.

(a) $Z \to \nu\bar{\nu} + j$

(b) $Z \to l^+l^- + j$

(c) $W \to l\bar{\nu} + j$

(d) $t\bar{t}$

(e) single top quark

(f) QCD multi-jet events

Figure 4.5: Diagrams of the SM background processes.

matrix elements. The MLM [83] matching scheme is adopted to remove overlap between the the n and $n+1$ parton samples from the matrix element (ME) and the PS.

Top quark production

Top quark pair ($t\bar{t}$) production process is simulated with POWHEG [84] interfaced to PYTHIA for the fragmentation and hadronization processes. The top quark mass is fixed at 172.5 GeV, and th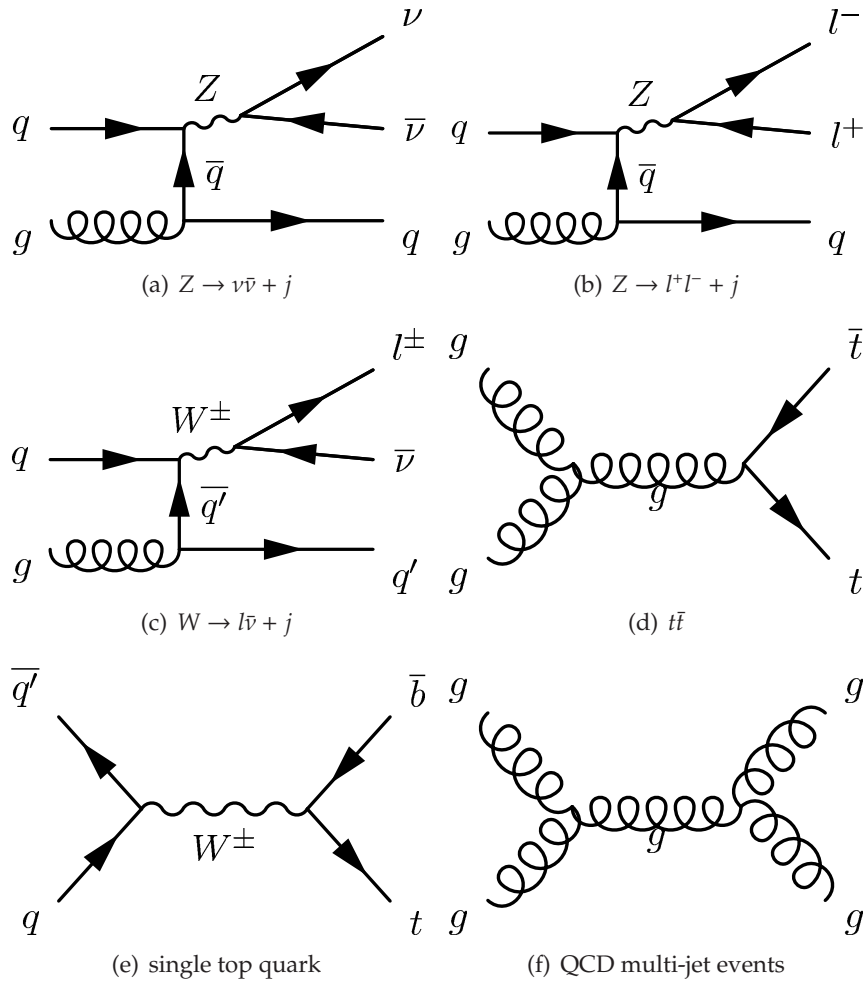e CT10 PDF set is used. Single top quark production process for the s-channel and Wt processes is simulated with MC@NLO [85] interfaced to Herwig and Jimmy, while the t-channel process is simulated with AcerMC [86] interfaced to PYTHIA and using the CTEQ6L1 PDF set.

QCD multi-jet events production

The events are generated with PYTHIA6 [87]. The samples are generated separately for different slices of the hard process momentum to ensure enough statistics in the large jet p_{T} region.

The background predictions are normalized to theoretical cross-sections, calculated including higher-order QCD corrections where available. The inclusive cross-sections for Z/W +jets processes are calculated with DYNNLO [88] with the MSTW2008LO PDF set. Approximate next-to-next-to-leading-logarithm cross-sections are used in the normalization of the $t\bar{t}$ and single top quark samples.

Chapter 5

Object Reconstruction

The analysis presented in this dissertation relies on the identification and reconstruction of tracks, jets, electrons, muons, and missing transverse momentum produced in the *pp* collisions and collected by the ATLAS detector. In this chapter, general reconstruction criteria and algorithms used in the ATLAS experiment are presented.

5.1 Track reconstruction

A large number of charged particles are produced in *pp* collisions at the LHC. When particles go through the detector, a lot of hits are generated. The aim of track reconstruction is to distinguish the hits originating from the different charged particles and determine trajectories that best matches the measurements.

Two algorithms are employed in the ATLAS experiment as the standard track reconstruction [89]: "inside-out" and "onside-in" reconstruction. The first algorithm is optimized to find primary tracks coming from the interaction point, while the second one is optimized for the reconstruction of electrons from photon conversions in the ID volume.

In addition to the standard track reconstruction, an extra extended-track reconstruction called "Re-tracking" has been adopted in this analysis in order to increase the acceptance of short-length tracks, which especially enhances the sensitivity for decaying charginos that have short proper lifetimes.

5.1.1 Track parametrization

A track is parametrized at the point of the closest approach with the global z-axis using five *perigee parameters* as summarized in Table 5.1 and Fig. 5.1. The sign of d_0 is defined as positive, if $\phi - \phi_0 = \frac{\pi}{2} + 2n\pi$, where n is an integer.

d_0	: Transverse impact parameter	$d_0 = \pm \sqrt{x_P^2 + y_P^2}$
z_0	: Longitudinal impact parameter	$z_0 = z_P$
ϕ_0	: Azimuthal angle at perigee	$\phi_0 = \arctan(\frac{p_y}{p_x})$
θ	: Polar angle at perigee	$\theta = \operatorname{arccot}(\frac{p_x}{\sqrt{p_x^2 + p_y^2}})$
$\frac{q}{p}$	: Charge of the particle divided by momentum	$\frac{q}{p} = \frac{Q}{|\mathbf{p}|}$

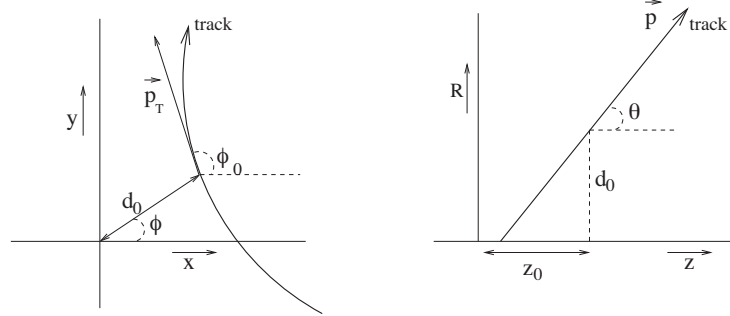Table 5.1: Track parameters at perigee

Figure 5.1: Illustration of the perigee parameters of a track in the transverse plane (left) and r-z plane (right).

5.1.2 Inside-out track reconstruction

The inside-out track reconstruction starts by finding track candidates in the silicon detectors and then extends the trajectories of successfully fitted tracks to the TRT detector to form full inner detector tracks.

1. **Space-Point Formation :** The first step in the inside-out track reconstruction is the creation of three-dimensional space-points of the silicon detector measurements. The pixel modules provide two-dimensional information, therefore the space-points are created in a simple way using the three-dimensional information from the surface representing the detector element. Single SCT clusters can not be transformed directly into space-points, since the precise measurement on an SCT module can only be given orthogonally to the silicon strip direction. However, two silicon microstrip detectors are constructed with a sandwich module structure that is rotated by a stereo angle with each other. Therefore, the three-dimensional space-point is formed by using two strip measurements together with a beam spot constraint. In contrast to the pixel detector, the SCT space-point formation leads to an intrinsic noise suppression at the very first pattern stage because it requires measurements from two different modules with separate readout for the creation of one single space-point object.

2. **Track Finding :** Space-points formed by the silicon detectors are collected to seed track candidates. This procedure is divided into two different tasks; one is the track seed finding and the other is the track candidate creation based on the seeds found in the first task.

   - **Track seed finding :** Space-point pairs from the pixel detector are found in the first step, and z vertices are built from these pairs. The primary vertex is used to further constrain the seeds with three or more space-points. Seeds are selected if they are in the tolerance region for predicted vertices.

   - **Track candidate creation :** The seeds provide directional information enough to construct roads of detector elements, and the track candidates are associated with extra hits. A Kalman fitter smoother formalism [90] is employed to follow trajectories and include successive hits simultaneously. The Kalman filter progressively updates the track information and predicts precisely the track representation on the next detector measurement.

3. **Ambiguity solving :** The seeded-track finding results in a large number of track candidates. Many of these track candidates share hits and are not originated from real particle trajectories. Therefore, tracks are ranked in their likelihood to describe the real trajectories of particles. The ambiguity solving process starts by refitting tracks using the refined reconstruction geometry

that has a detailed material description. However, this track fit only gives a reduced χ^2 and it is not appropriate to decide whether tracks are good or fake tracks that do not originate from real particle trajectory. The track scoring strategy is therefore adopted for the classification of tracks. For the classification of tracks, a different characteristics of a track is represented by a beneficial or penalty track score, which all together form an overall track score. The measurements of different sub-detectors are weighted with different scores by downgrading measurements from less precise detector parts. In general, each hit associated with a track leads to a higher score. On the other hand, holes, defined as absent hits on the passage of the track through a detector element, lower the track score. Track candidates remaining after the ambiguity solving process and having not more than six hits are neglected for further processing.

4. **TRT track extension :** Tracks reconstructed by the silicon detectors are extended to the TRT detector by associating extra hits in the TRT detector. Tracks are fitted again with the additional measurements in the TRT detector and compared with the original silicon-only tracks by the track scoring mechanism. In the case that the track score of a silicon track is higher than that of the extended track, the silicon track is kept and the extended track is neglected.

5.1.3   Outside-in track reconstruction

The inside-out track reconstruction sequence is complemented with an outside-in strategy. The outside-in strategy starts from unassigned TRT segments and looks for matching hits in the silicon detectors. This type of track reconstruction is mainly aimed at detecting late decays of neutral particles and photon conversions to $e^{\pm}$ pairs.

   The outside-in reconstruction starts with a TRT segment finding algorithm. This algorithm consists of two-step procedures: a global pattern recognition and a subsequent local pattern recognition. The TRT measurements do not provide the information about the coordinate along to the straw direction, therefore the space-points can not be formed. A global pattern recognition using the Hough transform technique [91] is thus performed in the projective plane: r-ϕ and r-z planes are adopted for the TRT in the barrel region and the end-cap region, respectively.

   The TRT track segments obtained by the global pattern recognition are further processed in a local pattern recognition algorithm. This algorithm uses the information of drift time, while the global pattern recognition employs only the straw center as the z-position. Eventually, the track segments are obtained via a Kalman filter-smoothing formalism. The track segments are extended inward in this algorithm. If the extended tracks have no associated hits in the silicon detector, tracks are categorized as the TRT-standalone tracks.
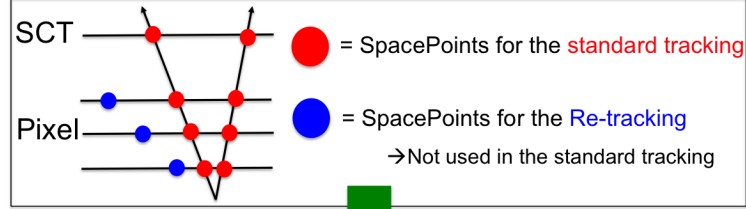
5.1.4 Re-tracking

The inside-out sequence is of particular interest for finding long-lived chargino trajectories, although it is optimized for the reconstruction of stable particles that leave long tracks in the ID, and in particular, only reconstructs tracks with a minimum of seven space points ($N_{min}^{clus} = 7$). An extended track reconstruction that provides pixel-seeded reconstructed tracks is developed, especially for this search, to make use of tracks having short length. In order to increase the acceptance of the track reconstruction and chargino track reconstruction efficiency at low radius, a third sequence (Re-tracking) is applied by following the standard track reconstruction algorithm. This sequence proceeds using leftover pixel and SCT hits from the two previous tracking sequences and reconstructs tracks with a minimum of three pixel hits ($N_{min}^{pixel} = 3$), while no SCT or TRT hits are required. The outward extension then follows; SCT and TRT hits are attached if they lie along the track trajectory. Figure 5.2 and Table 5.2 show a flowchart of the Re-tracking and details of the input parameters of the reconstruction algorithm for the Re-tracking, respectively. The input parameters of the reconstruction algorithm for the standard tracking are also shown in Table 5.2. The number of holes (N_{max}^{hole}) and shared hits (N_{max}^{share}) are allowed up to three and one in the standard track reconstruction, respectively, while they are both required to be zero in the Re-tracking in order to suppress fake tracks that are originating from combinations of wrong space-points in the procedure of track-seed finding or outward-extension of trajectories. The Re-tracking extends the sensitive decay volume inwards from $R_{decay} > 370$ mm to $R_{decay} > 150$ mm, where R_{decay} is the chargino transverse decay radius, as shown in Fig. 5.3 and 5.4. The performances of the Re-tracking are given in Chapter 6.

Parameter	Standard	Re-tracking
[Track Finding]		
usePixel	True	True
useSCT	True	False
N_{min}^{clus}	7	3
N_{max}^{hole}	3	0
[Ambiguity Solving]		
$p_{T,min}$	0.1 GeV	1 GeV
N_{min}^{clus}	7	3
N_{min}^{pixel}	0	3
N_{max}^{share}	1	0
N_{max}^{hole}	3	0
$N_{min}^{pixelhole}$	2	0

Table 5.2: Configuration for the track reconstruction algorithm.

1. Space-Point Formation

SCT

● = SpacePoints for the standard tracking

Pixel

● = SpacePoints for the Re-tracking
→Not used in the standard tracking

2. Track Seed Finding

Pixel

○ = PixelHole
→Required to be 0 in the Re-tracking

→ = Good pixel-seeded tracks

3. Ambiguity Solving

Pixel

● = SharedHits
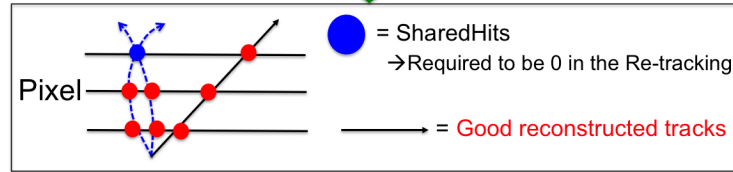→Required to be 0 in the Re-tracking
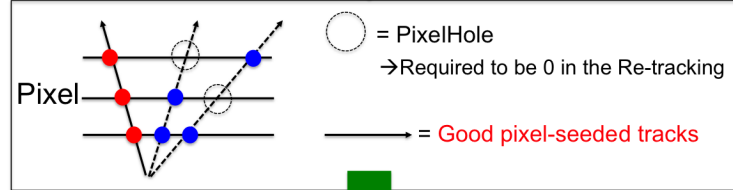
→ = Good reconstructed tracks

Figure 5.2: Flowchart of the Re-tracking.
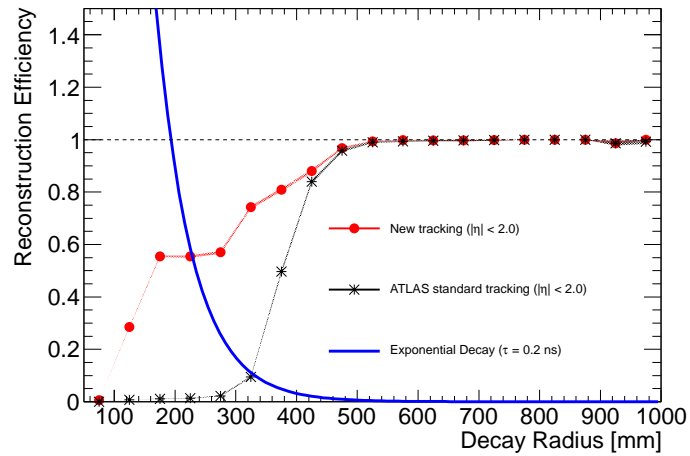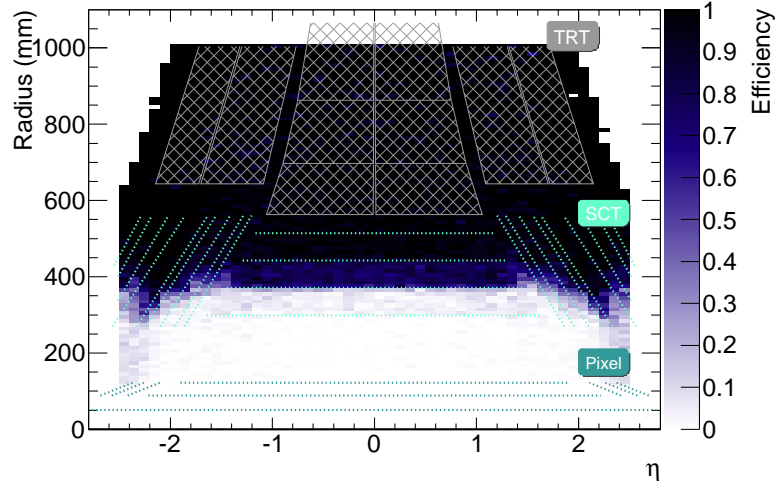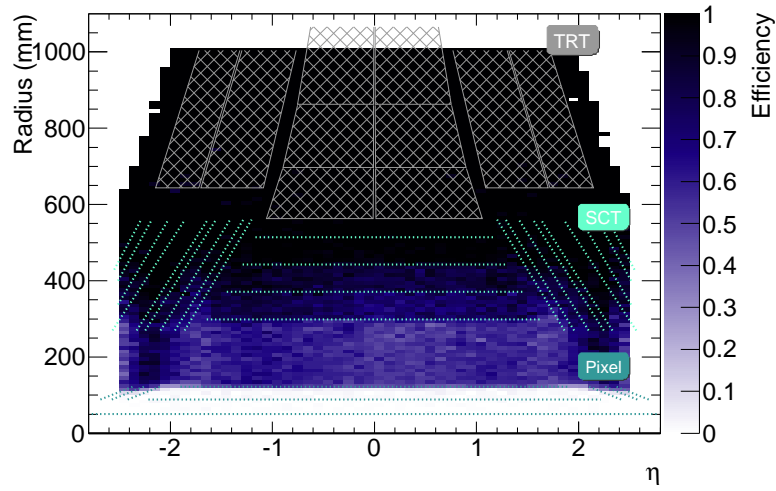

Figure 5.3: Tracking efficiency for decaying charginos as a function of R_{decay}.

(a) ATLAS standard track reconstruction

(b) Extended track reconstruction (= standard track reconstruction + Re-tracking)

Figure 5.4: Two-dimensional R_{decay}–η tracking efficiency map for decaying charginos with the standard (a) and extended (b) track reconstruction algorithms.

5.2   Vetex reconstruction

Primary vertices are reconstructed using an iterative vertex finding algorithm [92, 93]. Vertex seeds are obtained from the z-position of the reconstructed tracks at the beamline. An iterative χ^2 fit is performed using a seed and nearby tracks. Each track carries a weight that is a measure of its compatibility with the fitted vertex depending on the χ^2 of the fit. Tracks displaced by more than $7\,\sigma$ from the vertex are used to seed a new vertex and the procedure is repeated until no additional vertices can be found. The beam spot position is used as a three-dimensional constraint in the fit. Resulting reconstructed vertices are required to have at least two associated tracks.

5.3   Jet

5.3.1   Reconstruction

The aim of reconstruction of jets is to estimate the momentum of the colored partons that undergo fragmentation and hadronization processes before reaching the detector. The reconstruction of jets are performed by the following three steps:

1. Clustering signals from the calorimeter cells,

2. Combination of spatially related calorimeter cells into a jet by jet finding algorithm,

3. Calibration of reconstructed jets to the particle level.

5.3.2   Clustering of calorimeter cells

A cluster is seeded by a cell having a signal to noise ratio ($\equiv E_{\mathrm{cell}}/\sigma_{\mathrm{noise}}$) above a threshold of $E_{\mathrm{cell}}/\sigma_{\mathrm{noise}} > 4$. The noise σ_{noise} is measured for each cell independently and is defined as the expected RMS of the electronic noise in the cell. The contribution from pile-up is also added in quadrature. Cells neighboring to the seed whose $E_{\mathrm{cell}}/\sigma_{\mathrm{noise}}$ is greater than two are added to the cluster. Finally, all cells surrounding the cluster are added to the cluster without any energy threshold, and then a three-dimensional topological cluster (*topo-cluster*) is formed. The position of the cluster is calculated by the energy weighted cell positions.

5.3.3   Jet finding algorithm

Jets are reconstructed by anti-kT algorithm [94] with the distance parameter of 0.4 using topo-clusters as an input. The anti-k_T algorithm is an iterative sorting algorithm applied to topo-clusters, aiming to associate nearby topo-clusters into a jet using a distance defined below.

$$d_i = p_{T,i}^{-2} \tag{5.1}$$

$$d_{ij} = \min(p_{T,i}^{-2}, p_{T,j}^{-2}) \frac{(\eta_i - \eta_j)^2 + (\phi_i - \phi_j)^2}{R^2} \tag{5.2}$$

$$\equiv \min(p_{T,i}^{-2}, p_{T,j}^{-2}) \frac{\Delta_{ij}^2}{R^2} \tag{5.3}$$

where $p_{T,i}$ is the transverse momentum of each constituents, and R is the distance parameter controlling the size of the jet, which is set to be 0.4 in the anti-k_T algorithm. The algorithm starts by calculating the minimum value (d_{min}) among all d_i and d_{ij}. If the smallest distance is found to be d_{ij} between two topo-clusters, then those two topo-clusters are combined to form a larger topo-cluster: their four-momenta are summed, the distances are recalculated, and the iterative process continues. If the smallest distance is found to be a d_i, then that topo-cluster is defined as a jet and removed from the collection of topo-clusters. This algorithm continues until no more topo-clusters remain.

5.3.4 Calibration

Jets are reconstructed from the calorimeter clusters at the electromagnetic (EM) energy scale. The EM energy scale provides an energy calibration for electromagnetically interacting particles and was determined using test-beam measurements for electrons [95]. The measurement of jet transverse momentum at the EM scale ($p_T^{jet,EM}$) underestimates that of hadron-level jets due to the nature of the non-compensating calorimeters and the dead material. Thus, an average correction is applied to obtain the correct transverse momentum depending on η and $p_T^{jet,EM}$. For this purpose, a scheme to calibrate energy depositions from hadrons based on calorimeter signals and the observed shower shape (local cluster weighting; LCW) is used. LCW calibration starts by classifying topo-clusters as electromagnetic or hadronic based on their shower shapes. The energy of the hadronic topo-clusters is then corrected for the lower response of the calorimeters to hadronic deposits by applying multiplicative calibration weights to their constituent cells. These weights are derived from Geant4 simulations of charged single pions.

5.3.5 Jet energy scale uncertainty

The jet energy scale (JES) uncertainty [96] comes mainly from the uncertainty on the single particle response in the calorimeter. Other leading contributions come from the limitation on the knowledge for the detector such as the amount of dead material and the uncertainty on the effects of pile-up. Figure 5.5 shows the overall jet energy scale uncertainties as a function of $p_{T,jets}$ and η_{jets}
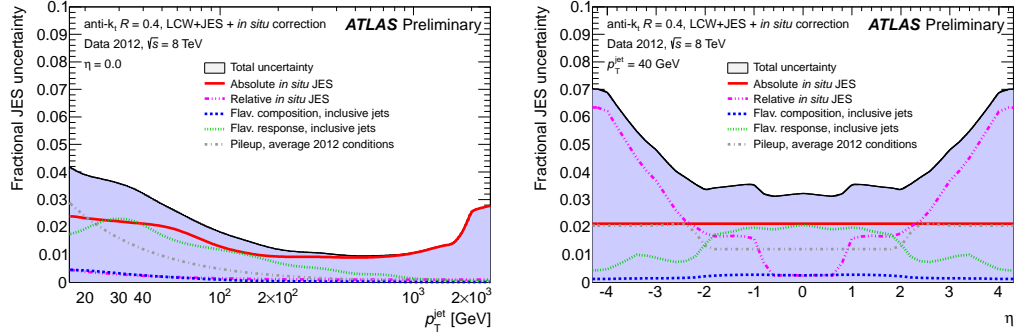
(a) Jet energy scale uncertainty as a function of $p_{\mathrm{T,jets}}$ at $|\eta_{\mathrm{jets}}| = 0.0$

(b) Jet energy scale uncertainty as a function of pseudorapidity at $p_{\mathrm{T,jets}} = 40$ GeV

Figure 5.5: Fractional jet energy scale systematic uncertainty components. The total uncertainty, which is calculated by summing all components in quadrature, is shown as a filled blue region topped by a solid black line.

These systematic uncertainties are assigned using in-situ techniques that exploit the transverse momentum balance between a jet and a well measured reference object: a direct transverse momentum balance between a jet and a photon or Z boson decaying to electron or muon pairs, and a balance between a high-p_{T} jet recoiling against one or more lower-p_{T} jets. Figure 5.6 shows the jet response ratio of the data to the MC simulation as a function of p_{T} for three in-situ techniques.

5.4 Electron

5.4.1 Reconstruction

Electron reconstruction starts with the formation of seed clusters in the middle sampling of the electromagnetic calorimeter, and then they are required to have corresponding reconstructed tracks.

1. **Clustering :** A sliding-window clustering algorithm [97] is used to reconstruct electron clusters. The sliding-window algorithm scans a fixed-size window over the $\eta - \phi$ grid of calorimeter cells, searching for a local maxima of energy contained in the window. The reconstruction starts by clustering seeds with a window size 3×0.025 units in η and 5×0.025 units in ϕ. The seed clusters are required to have transverse energies above a threshold of 2.5 GeV.

2. **Track-Cluster matching :** Once the seed clusters are formed, they are required to have corresponding reconstructed tracks that are extrapolated from the last measurement point in the ID to the middle sampling of the electromagnetic calorimeter. The η-distance between the track impact point and the
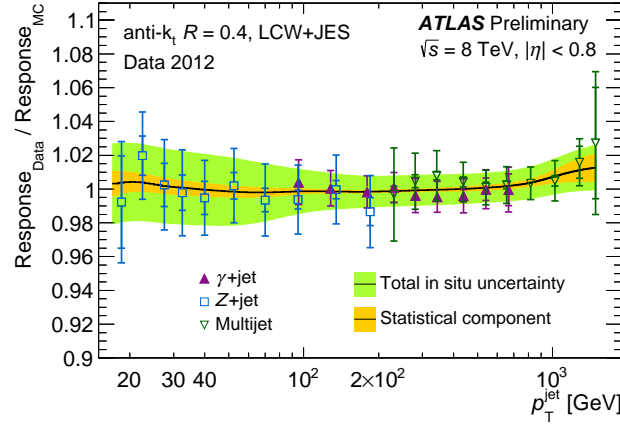
Figure 5.6: Jet response ratio of the data to the MC simulation as a function of p_{T} for three in situ techniques combineded to determine the in-situ energy scale correction: Z+jet (squares), gamma+jet (full triangles), and QCD multi-jet (empty triangles) events. The error bars indicate the statistical and the total uncertainties. The black line shows the combination of all in-situ techniques, and the outer band indicates the total uncertainty resulting from the combination of all in-situ techniques, while the inner band shows the fraction from statistical uncertainties only.

cluster position is required to fulfill $\Delta\eta < 0.05$. To account for energy losses by bremsstrahlung, the size of ϕ-window is set to 0.1 on the side where the extrapolated track bends as it traverses the solenoidal magnetic field, and 0.05 on the other side. An electron is reconstructed if at least one track is matched to the seed cluster. If multiple tracks are matched to the cluster, tracks with larger silicon hits are preferred, and the track with the closest in the η-ϕ plane is chosen. In 8 TeV data, in order to recover the track reconstruction efficiency for electrons that undergo significant bremsstrahlung in the detector, a Gaussian Sum Filter (GSF) algorithm [98] that re-fit tracks associated to the seed cluster is developed. This algorithm consists of a modified pattern recognition that allows for energy loss at each material surface, and improves the reconstruction efficiency by 7-8 % as shown in Fig. 5.7

After the track-cluster matching, the electron clusters are rebuilt using 3×7 (5×5) longitudinal towers of cells in the barrel (endcap) region. The electron energy is then determined by adding four different components: (a) the energy deposit measured in the cluster, (b) the energy estimated to have been lost in the material in front of the electromagnetic calorimeter, (c) the energy estimated to have leaked laterally outside of the cluster, and (d) the energy estimated to have leaked longitudinally behind the cluster. These components are parametrized as a function of the energies measured in the different longitudinal layers of the
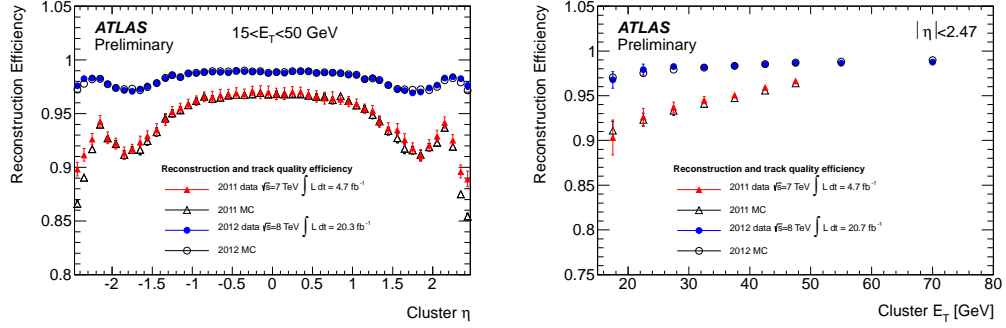
(a) Electron reconstruction efficiency as a func- (b) Electron Reconstruction efficiency as a func-
tion of η for electrons with $15 < E_T < 50$ GeV.   tion of E_T for electrons with $|\eta| < 2.47$.

Figure 5.7: Electron Reconstruction efficiency for data (filled markers) and MC
(open markers) for the 2011 (triangles) and the 2012 (circles) data samples.

electromagnetic calorimeter based on MC.

5.4.2   Identification criteria

The purity of real electrons is small at the stage described above. Reconstructed
electrons suffer large backgrounds originating from (a) mis-identified hadrons,
(b) photon conversions, and (c) semi-leptonic decays of heavy flavor hadrons.
Therefore, electrons are identified by the application of selection criteria. Three
reference sets of selection requirements (*Loose*, *Medium* and *Tight*) are defined with
increasing background rejection power as summarized in Table 5.3. Figure 5.8
shows the identification efficiency of electrons estimated with a "tag and probe"
method using $Z \rightarrow ee$ decays as a function of E_T or the number of primary ver-
tices. In this analysis, the loose (tight) identification criteria is adopted for the
identification of electrons in the signal search (background control) sample. The
dependency of pile-up on the identification efficiency is negligibly small, and the
average efficiency for the loose (tight) criteria is about 95 (80) %.

5.5   Muon

5.5.1   Reconstruction

Muon candidates are reconstructed by the ID and the MS. Several algorithms are
adopted to reconstruct muons according to the available information from the ID
and the MS:

- **Stand-alone muon :** The trajectory of muon is reconstructed only in the MS.
  The direction and the impact parameter of the muon at the interaction point
  are determined by extrapolating the track reconstructed in the MS back to

Type	Description	Variable name
Loose		
Acceptance of the detector	• $\|\eta\| < 2.47$	
Hadron leakage	• Ratio of E_T in the first layer of the hadronic calorimeter to E_T of the EM cluster (in the range $\|\eta\| < 0.8$ and $\|\eta\| > 1.37$) • Ratio of E_T in the hadronic calorimeter to E_T of the EM cluster (in the range $\|\eta\| > 0.8$ and $\|\eta\| < 1.37$)	$R_{\mathrm{h}ad1}$ $R_{\mathrm{h}ad}$
First layer of EM calorimeter.	• Total shower width. • Ratio of the energy difference associated with the largest and second largest energy deposit over the sum of these energies	w_{stot} E_{ratio}
Second layer of EM calorimeter	• Ratio in η of cell energies in 3×7 versus 7×7 cells. • Lateral width of the shower.	R_η $w_{\eta 2}$
Track quality	• Number of hits in the pixel detector ≥ 1. • Number of hits in the pixel and SCT detectors ≥ 7.	N_{pixel} N_{Si}
Track matching	• $\Delta\eta$ between the cluster and the track < 0.015 (< 0.005 for Medium and Tight selection)	$\Delta\eta_1$
Medium = Loose +		
Third layer of EM calorimeter	• Ratio of E_T in the third sampling to E_T of the EM cluster	f_3
Track quality	• Number of hits in the innermost pixel layer • Ratio of the number of high-threshold hits to the total number of hits in the TRT. • Transverse impact parameter with respect to the primary vertex < 5 mm (< 1 mm for Tight selection)	$N_{\mathrm{b-layer}}$ R_{TRT} d_0
Tight = Medium +		
Track quality	• Number of hits in the TRT.	N_{TRT}
Track matching	• $\Delta\phi$ between the cluster and the track. • Ratio of the cluster energy to the track momentum.	$\Delta\phi_2$ E/p
Conversions	• Electron candidates matched to reconstructed photon conversions are rejected	

Table 5.3: Definition of variables used for loose, medium, and tight electron identification requirements for the central region of the detector ($\|\eta\| < 2.47$).
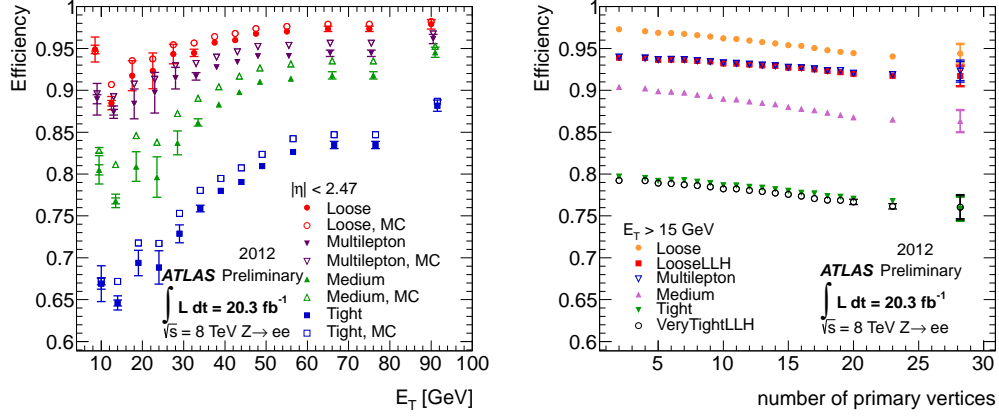
(a) Identification efficiency of electrons as a func-
tion of E_T.

(b) Identification efficiency of electrons as a func-
tion of the number of reconstructed primary ver-
tices.

Figure 5.8: Identification efficiency of electrons estimated with a "tag and probe"
method using $Z \rightarrow ee$ decays.

the point of closest approach to the beam line. The extrapolation takes into
account both multiple scatterings and energy losses in the calorimeter.

- **Combined muon :** A muon candidate is reconstructed independently in the
  ID and MS. A combined track is then formed from the successful combination
  of a track made by the stand-alone algorithm with a track reconstructed in
  the ID.

- **Segment-tagged muon :** A track in the ID is reconstructed as a muon if at
  least one track segment in the MDT or CSC is associated with the extrapolated
  track to the MS.

In order to reject fake muons originating mostly from semi-leptonic decays of
heavy flavor hadrons, tracks formed by the ID are required to pass the quality
criteria based on the number of hits in the pixel, SCT and TRT detectors:

- $N_{b-layer} \geq 1$, if crossing an active module of the innermost pixel layer.

- $N_{pixel} \geq 1$.

- $N_{SCT} \geq 5$.

- The number of associated holes in the silicon detectors < 3.

- $(N_{TRT} + N_{TRT^{outliers}}) > 5$ and $N_{TRT^{outliers}} < 0.9(N_{TRT} + N_{TRT^{outliers}})$ for $0.1 < |\eta| <$
  1.9.

- If $(N_{\text{TRT}} + N_{\text{TRT}^{\text{outliers}}}) > 5$, then $N_{\text{TRT}^{\text{outliers}}} < 0.9(N_{\text{TRT}} + N_{\text{TRT}^{\text{outliers}}})$ for $|\eta| < 0.1$ or $|\eta| > 1.9$.

where N_{SCT} and $N_{\text{TRT}^{\text{outliers}}}$ denote the number of SCT hits and the number of TRT outliers on the muon track, respectively.

5.5.2   Performance

The reconstruction efficiency of muons is measured with a "tag and probe" method using di-muon decays of Z bosons [99]. Figure 5.9 (a) and (b) show the reconstruction efficiencies for combined muons measured with the data and MC simulation as a function of η and the number of reconstructed primary vertices, respectively. The average reconstruction efficiency is estimated to be about 97 % and the difference between data and MC simulation is less than 2 %. The dependency of pile-up on the reconstruction efficiency is negligibly small and calculated to be less than 2 %.
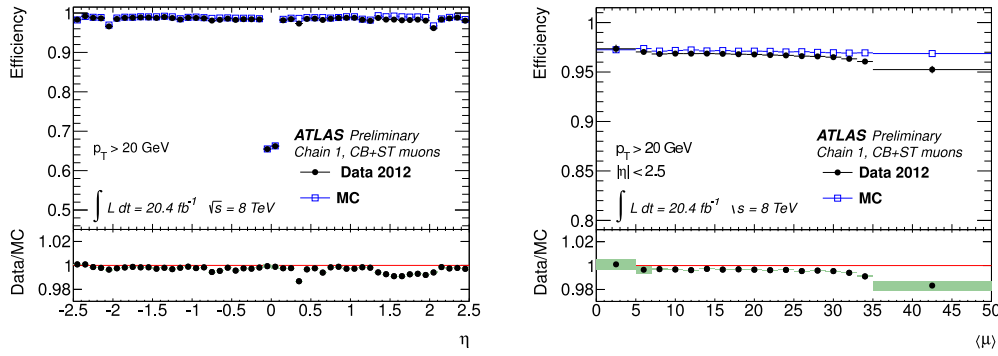
(a) Reconstruction efficiency of muons as a function of η.

(b) Reconstruction efficiency of muons as a function of the number of reconstructed primary vertices.

Figure 5.9: Reconstruction efficiency of muons estimated with a "tag and probe" method using di-muon decays of Z bosons.

5.6   Missing transverse energy

The missing transverse energy is the energy imbalance in the transverse plane. The physical source of such an imbalance is the presence of unseen particles such as neutrinos or LSPs escaping the detector without leaving any signal. The $E^{\text{miss}}_{x(y)}$ is calculated from the negative vector sum of calibrated $\overrightarrow{p}_{x,y}$ of reconstructed physics objects. The topo-clusters not associated with any such objects are also taken into account as the $E^{\text{miss}}_{\text{T}}$ soft term.

$$E_{\text{x(y)}}^{\text{miss}} = E_{\text{x(y)}}^{\text{miss,e}} + E_{\text{x(y)}}^{\text{miss,jets}} + E_{\text{x(y)}}^{\text{miss,}\mu} + E_{\text{x(y)}}^{\text{miss,SoftTerm}}. \tag{5.4}$$

$$E_{\text{T}}^{\text{miss}} = \sqrt{(E_{\text{x}}^{\text{miss}})^2 + (E_{\text{y}}^{\text{miss}})^2}. \tag{5.5}$$

In Eq. 5.5, electrons reconstructed by loose criteria described in Sec. 5.4, jets with $p_{\text{T}} > 20$ GeV and $|\eta| < 4.5$, and muons reconstructed by the selection criteria described in Sec. 5.5 are used. The soft term is calculated from topo-clusters and tracks not associated to high-p_{T} objects. The topo-clusters are calibrated using the LCW technique, and any overlap between tracks and topo-clusters are resolved.

The energy scale uncertainties of jets, electrons, and muons are propagated to the $E_{\text{T}}^{\text{miss}}$ calculation and used to assign the $E_{\text{T}}^{\text{miss}}$ scale uncertainty.

Chapter 6

Tracking Performance

The extended track reconstruction, introduced in Sec. 5.1.4, significantly improves the tracking efficiency for decaying charginos at low radius. This chapter summarizes the studies that validate the performances of the extended track reconstruction.

6.1 Tracking performance for decaying charginos

As described in Sec. 5.1.4, the Re-tracking requires a minimum of three pixel hits and reconstruct momenta with smaller track stubs, which may result in a decline in the performances especially on the p_T-scale and resolution. The track p_T is a discriminant variable between signal and background tracks, therefore, its performance is critical to this analysis.

Figure 6.1 shows the two-dimensional distributions of $(p_T^{rec} - p_T^{\tilde{\chi}_1^\pm})/p_T^{\tilde{\chi}_1^\pm}$ vs. $p_T^{\tilde{\chi}_1^\pm}$ for different numbers of SCT hits N_{SCT}, where $p_T^{rec(\tilde{\chi}_1^\pm)}$ is the reconstructed (chargino) track p_T. In the case that a chargino decays before reaching the first SCT layer and the corresponding track have no associated SCT hits, the reconstructed p_T is biased and has a poor resolution. Therefore, reconstructed tracks are required to have $N_{SCT} \geq 2$. Although this requirement reduces the efficiency for charginos having decay radii below 300 mm (the first SCT layer), it significantly suppresses fake tracks that could have largely mismeasured p_T (p_T-mismeasured tracks) and contribute to the background in this analysis.

Figure 6.2 shows the relation between the number of silicon hits associated to reconstructed chargino tracks and the true decay radius of $\tilde{\chi}_1^\pm$, ensuring that the decay vertex and track length are well reconstructed.

6.2 Tracking performance in QCD multi-jet events

When charged hadrons interact with material in the silicon detectors, the standard track reconstruction can hardly find their tracks, while the Re-tracking enhances
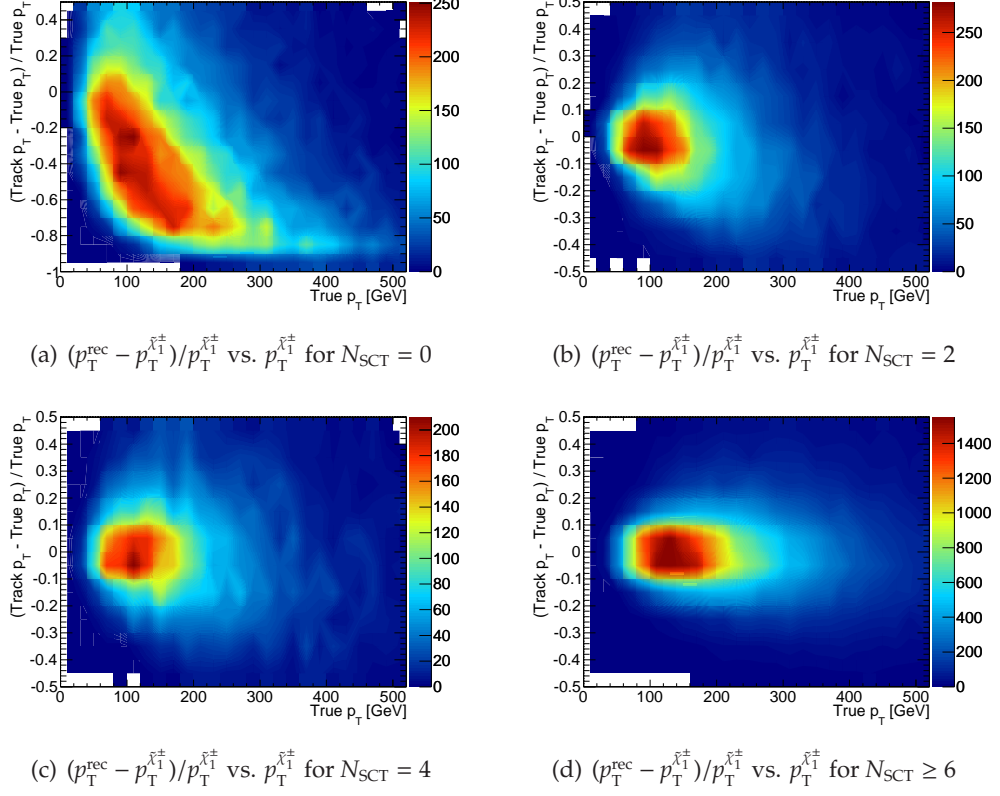
(a) $(p_T^{rec} - p_T^{\tilde{\chi}_1^{\pm}})/p_T^{\tilde{\chi}_1^{\pm}}$ vs. $p_T^{\tilde{\chi}_1^{\pm}}$ for $N_{SCT} = 0$

(b) $(p_T^{rec} - p_T^{\tilde{\chi}_1^{\pm}})/p_T^{\tilde{\chi}_1^{\pm}}$ vs. $p_T^{\tilde{\chi}_1^{\pm}}$ for $N_{SCT} = 2$

(c) $(p_T^{rec} - p_T^{\tilde{\chi}_1^{\pm}})/p_T^{\tilde{\chi}_1^{\pm}}$ vs. $p_T^{\tilde{\chi}_1^{\pm}}$ for $N_{SCT} = 4$

(d) $(p_T^{rec} - p_T^{\tilde{\chi}_1^{\pm}})/p_T^{\tilde{\chi}_1^{\pm}}$ vs. $p_T^{\tilde{\chi}_1^{\pm}}$ for $N_{SCT} \geq 6$

Figure 6.1: Two-dimensional distribution of $(p_T^{rec} - p_T^{\tilde{\chi}_1^{\pm}})/p_T^{\tilde{\chi}_1^{\pm}}$ vs. $p_T^{\tilde{\chi}_1^{\pm}}$ with different requirements on N_{SCT}.
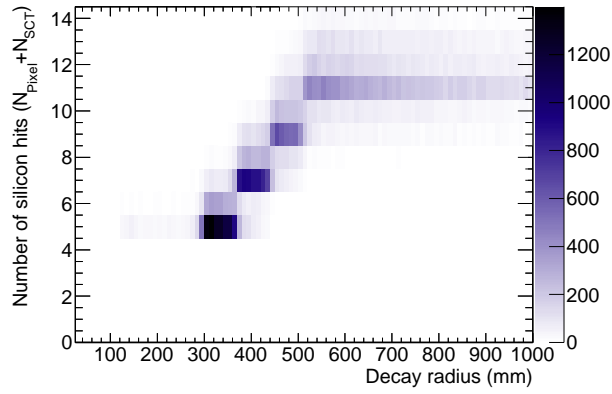

Figure 6.2: Relation between the number of silicon hits associated to the reconstructed chargino track and the decay radius of $\tilde{\chi}_1^{\pm}$.

the potential for reconstructing their primary tracks. The tracking performance, especially for tracks reconstructed by the Re-tracking, is validated using hadron tracks in a QCD multi-jet enriched sample, by comparing to that for MC events.

Events with isolated hadron tracks are selected as follows:

Event selection

- Dataset : QCD multi-jet enriched sample collected by single-jet triggers.

- Jet quality requirements[1].

- At least one reconstructed primary vertex with a minimum of five tracks with $p_T > 0.4$ GeV.

- No identified electrons and muons with $p_T > 10$ GeV.

- Leading jet $p_T > 90$ GeV.

- $E_T^{miss} < 90$ GeV, which is orthogonal to the event selection in the signal search sample[2].

- At least one hadron track.

Selection criteria for hadron tracks

- $p_T > 15$ GeV.

- $|d_0| < 1.5$ mm.

- $|z_0 \sin \theta| < 1.5$ mm.

- $N_{b-layer} \geq 1$, if crossing an active module of the innermost pixel layer.

- $N_{pixel} \geq 1$.

- $2 \leq N_{SCT} < 4$.

- ΔR between the track and the nearest jet with $p_T > 20$ GeV should be smaller than 0.1.

where z_0 is the longitudinal impact parameters with respect to the primary vertex.

The requirement $2 \leq N_{SCT} < 4$ enhances pixel-seeded tracks reconstructed by the Re-tracking. The variables of track hit information and track quality are summarized in Table 6.1.

Figure 6.3–6.5 show various distributions of the reconstructed tracks for the observed data in the QCD multi-jet enriched sample and MC predictions. The performance of Re-tracking in the observed data reasonably agrees with that in the MC simulation, even though the number of hits in silicon detectors are fewer than that of ATLAS standard tracks [100].

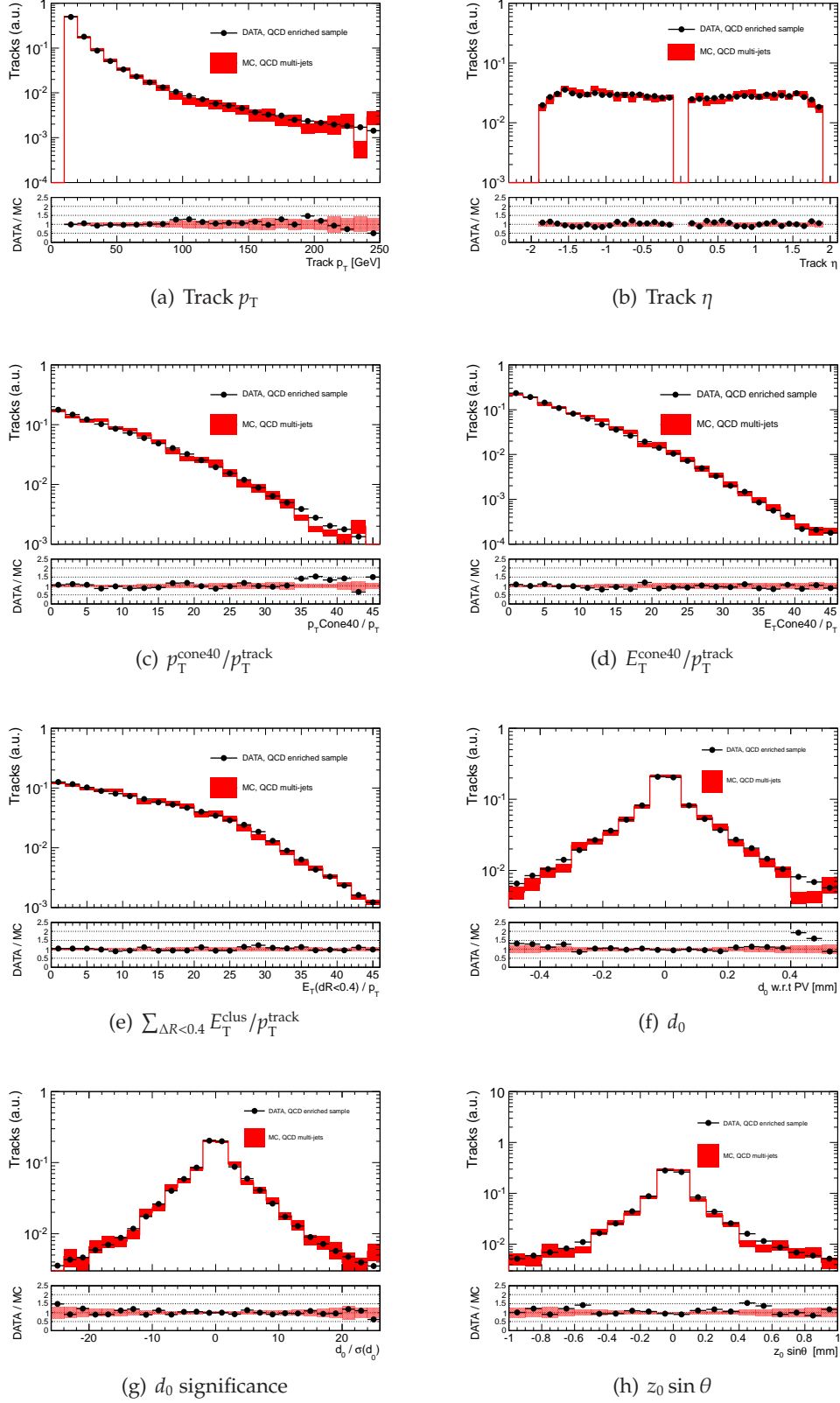
[1]Described in Sec. 8.2.3.
[2]Described in Sec. 8.2.4.

(a) Track p_T

(b) Track η

(c) p_T^{cone40}/p_T^{track}

(d) E_T^{cone40}/p_T^{track}

(e) $\sum_{\Delta R<0.4} E_T^{clus}/p_T^{track}$

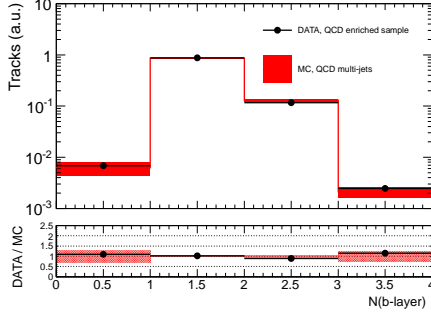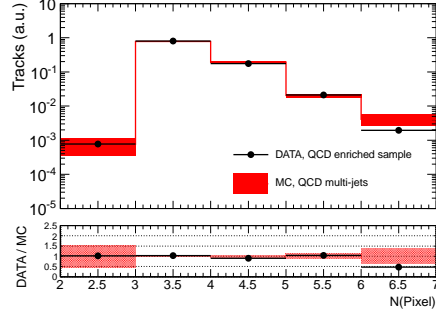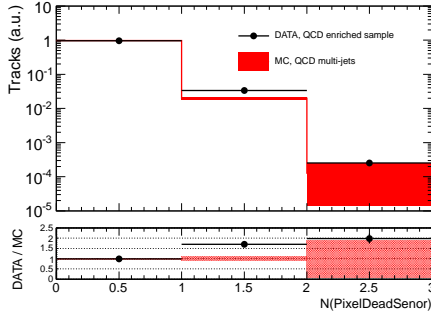(f) d_0

(g) d_0 significance

(h) $z_0 \sin\theta$

Figure 6.3: Reconstructed track p_T, η, isolation information, and impact parameter variables for hadron tracks in the QCD multi-jet enriched sample and MC predictions.
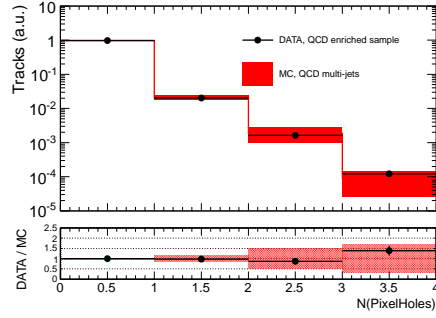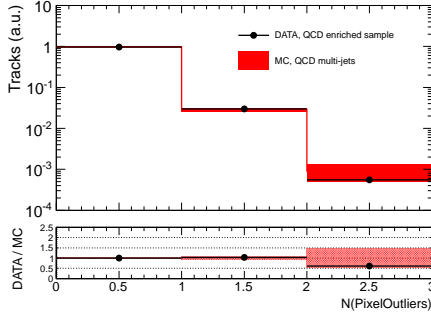
(a) Number of b-layer hits
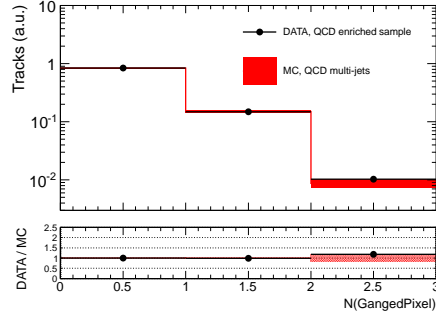
(b) Number of pixel hits
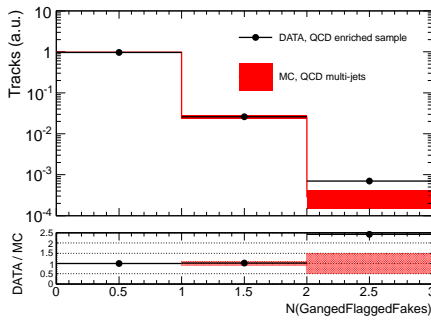
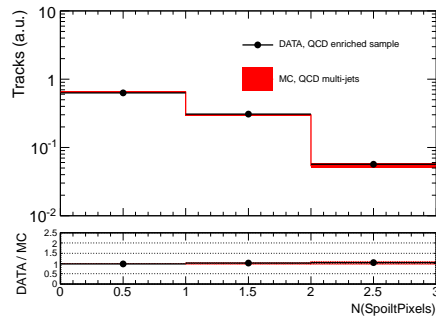(c) Number of dead pixel sensors

(d) Number of pixel holes

(e) Number of pixel outliers

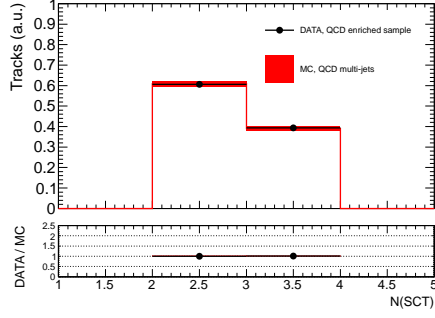(f) Number of ganged pixel hits

(g) Number of ganged pixel hits flagged as fake

(h) Number of spoilt pixel hits
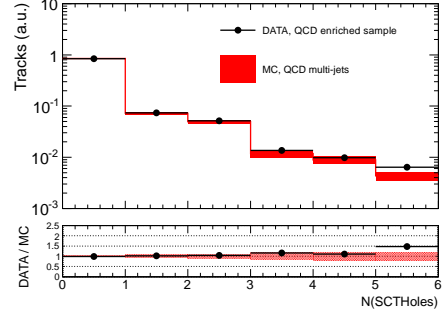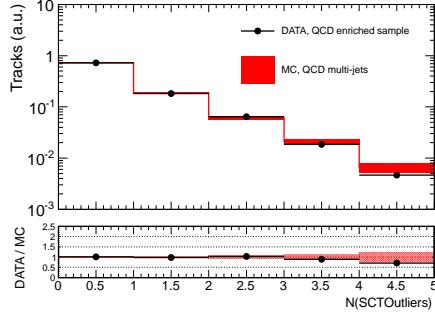
Figure 6.4: Pixel-hit variables for hadron tracks in the QCD multi-jet enriched sample and MC predictions.
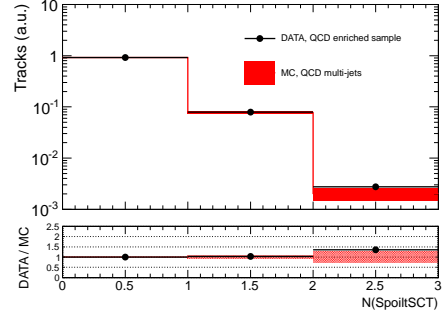
(a) Number of SCT hits

(b) Number of SCT holes

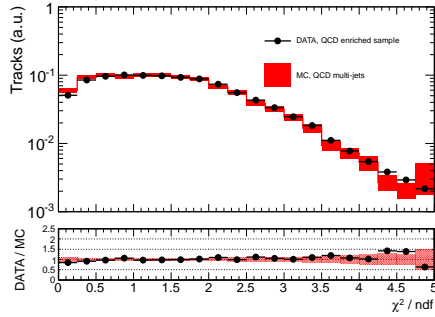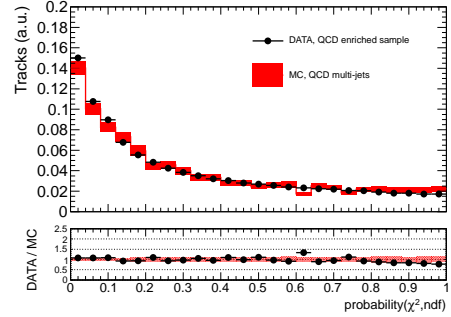(c) Number of SCT outliers

(d) Number of spoilt SCT hits

(e) χ^2/ndf

(f) χ^2 probability

Figure 6.5: SCT-hit and track quality variables for hadron tracks in the QCD multi-jet enriched sample and MC predictions.

Variable	Description
Number of dead sensors	The number of dead sensors on the track
Number of holes	The number of pixel layers or SCT sensors on the track with the absence of hits
Number of outliers	The number of hits with bad track-fit qualities
Number of spoilt hits	The number of hits with broad position errors
Number of ganged pixels	The number of hits formed in a single pixel row of which the readout is shared with another pixel
$p_\mathrm{T}^{\mathrm{cone40}}$	The sum of p_T of all tracks with $p_\mathrm{T} > 400$ MeV, $\|d_0\| < 1.5$ mm, and $\|z_0 \sin\theta\| < 1.5$ mm that lie within a cone of $\Delta R = 0.4$ around the track
$E_\mathrm{T}^{\mathrm{cone40}}$	The transverse calorimeter energy deposited in a cone of $\Delta R < 0.4$ around the track excluding E_T of its representing calorimeter cluster
$\sum_{\Delta R < 0.4} E_\mathrm{T}^{\mathrm{clus}}$	The sum of cluster energies in a cone of $\Delta R = 0.4$ around the track

Table 6.1: Definition of variables for track hit information and track quality.

Chapter 7

Properties of Signal Events

7.1 Production process

The AMSB model can be explored in the following two production processes at the LHC.

- **Strong production process**
  Production cross-sections for gluinos via strong interactions are predicted to be large in *pp* collisions. The typical cross-section is ~ 0.1 pb for a gluino with a mass of ~ 1 TeV. In the AMSB model, the masses of other sparticles with color charge are predicted to be $O(10\text{-}100)$ TeV as indicated in Sec. 2.3.4. Therefore, only the gulino among colored sparticles can be produced at LHC energies. The event topology of the gluino-pair production process is characterized by multiple high$-p_{\mathrm{T}}$ jets emitted from the cascade decay of the gluino and a large $E_{\mathrm{T}}^{\mathrm{miss}}$ due to the LSPs escaping the detector.

- **Direct electroweak gaugino production process**
  The lightest charginos can be directly produced via electroweak interactions with a sizable cross-section at LHC energies as shown in Fig. 4.3. The dominant channels of the $\tilde{\chi}_1^{\pm}$ electroweak production are $\tilde{\chi}_1^{\pm}\tilde{\chi}_1^0$ and $\tilde{\chi}_1^+\tilde{\chi}_1^-$. The typical cross-section is ~ 1 pb for a chargino with a mass of ~ 200 GeV, and 20000 events are expected with the integrated luminosity used in this search (~ 20.3 fb^{-1}).

Previously, ATLAS explored charginos that have significant lifetimes via the gluino-pair production process [9,10,11]. However, a stringent limit of < 1.4 TeV [12] has been already set on the gluino mass by inclusive searches for squark and gluino production as shown in Fig. 7.1. Given the ratio M_3/M_2 of ~ 8 in the AMSB model, the mass of gluino is comparatively large. These facts indicate that the gluino-pair production process is suppressed at LHC energies, and the electroweak gaugino production is of particular importance. This search is dedicated to the direct electroweak gaugino production. Figure 7.2 shows an event display of the direct

production of $\tilde{\chi}_1^\pm \tilde{\chi}_1^0$ in a signal MC event. Since a chargino decays into a neutralino and a low-momentum charged pion in the ID, the signal events can not be triggered by a chargino. Therefore, a high-p_T jet from initial-state radiation is utilized to trigger the signal event. The resulting signal topology is then characterized by

- A high-p_T jet.

- Large missing transverse momentum due to LSPs escaping the detector.

- A high-p_T disappearing track.

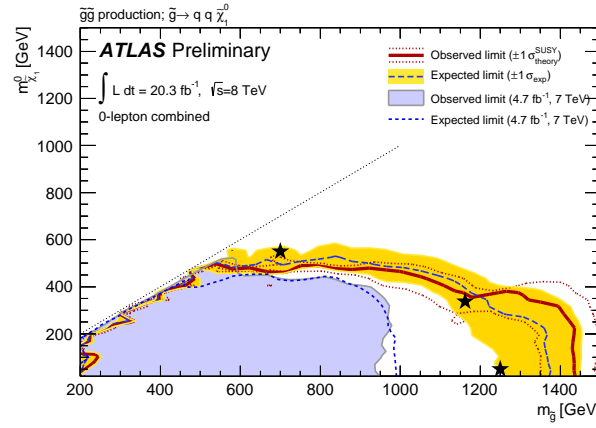Primary diagrams contributing to this search are illustrated in Fig. 4.4.

Figure 7.1: 95% CL exclusion curve for the direct production of gluino pairs with decoupled squarks. Gluinos are required to decay to two jets and a neutralino LSP. The blue dashed lines show the expected limits at 95% CL, with the light (yellow) bands indicating the 1σ excursions due to experimental and background-theory uncertainties. Observed limits are indicated by medium (maroon) curves, where the solid contour represents the nominal limit, and the dotted lines are obtained by varying the signal cross-section by the theoretical scale and PDF uncertainties.

7.2   Finding decaying chargino tracks

The expected signature of the chargino signal strongly depends on its lifetime. As shown in Fig. 7.3, the mean decay length of the lightest charginos is expected to be $\mathcal{O}$(cm). The pixel and SCT detectors cover the radial range from 50 to 514 mm, and the TRT, of particular importance to this search, covers the radial range from 560 to 1100 mm in the barrel region.

Strategies to detect the chargino tracks can be then classified into the followings depending on the $\tilde{\chi}_1^\pm$ decay vertex:
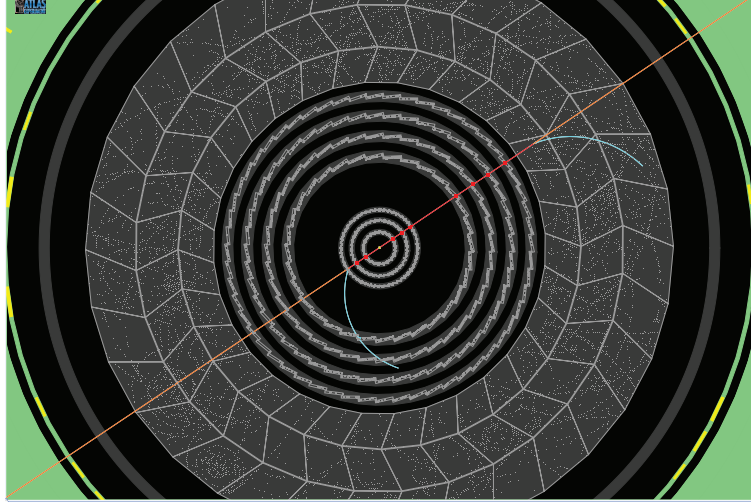
Figure 7.2: Event display of the direct production of $\tilde{\chi}_1^\pm \tilde{\chi}_1^0$ in a signal MC event. The true particle tracks in decays $\tilde{\chi}_1^\pm \to \tilde{\chi}_1^0 \pi^\pm$ are indicated by solid lines.
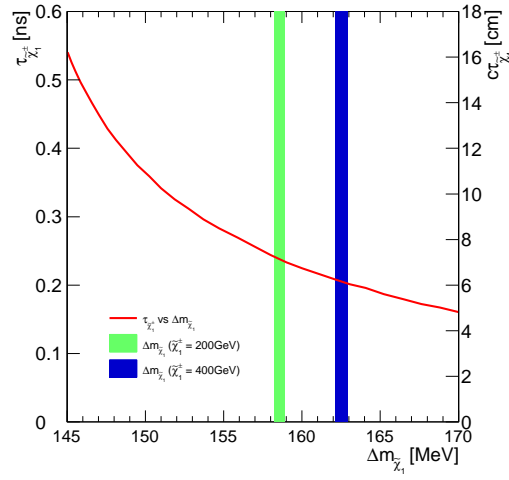
Figure 7.3: The $\tau_{\tilde{\chi}_1^\pm}$ ($c\tau_{\tilde{\chi}_1^\pm}$) as a function of $\Delta m_{\tilde{\chi}_1}$. The light (dark) green band shows the wino mass splitting ($\Delta m_{\tilde{\chi}_1}$) derived from Fig. 2.4 for the wino mass of 200 (400) GeV.

- **R$_{decay}$ < 50 mm:** Charginos decay before reaching the ID, therefore, they leave no hits in the detector; the detection of $\tilde{\chi}_1^\pm$ is impossible. In this case, the search for events with mono-jet plus large E_T^{miss} may work. However, it suffers from irreducible background processes such as $Z \rightarrow \nu \bar{\nu}$ and $W \rightarrow \tau \bar{\nu}$, and has low sensitivity.

- **50 mm < R$_{decay}$ < 550 mm:** Charginos decay in the silicon detectors and results in short tracks that can be reconstructed by the Re-tracking.

- **550 mm < R$_{decay}$ < 1100 mm:** Charginos decay in the TRT detectors. Their tracks can be fully reconstructed with the ATLAS standard track reconstruction.

In the search based on the 7 TeV dataset [13], the extended track reconstruction was not adopted and the sensitivity to charginos having $\tau_{\tilde{\chi}_1^\pm}$ of a fraction of a nanosecond was poor as shown in Fig. 2.9, which is attributed to the fact that the ATLAS standard track reconstruction is non-optimal for decaying charginos. It requires at least seven silicon hits associated to a track, resulting in an inefficiency for charginos decaying before reaching the outer SCT layers. The Re-tracking proceeds by re-running the pixel-seeded tracking algorithm and provides a fully efficient tracking capability for charginos traversing the pixel detector. The track selection efficiency for decaying charginos has been improved significantly as shown in Fig. 7.4. The efficiency for charginos with $\tau_{\tilde{\chi}_1^\pm} \sim 0.2$ ns, predicted for $\Delta m_{\tilde{\chi}_1} \sim 160$ MeV, is around 100 times larger than in the previous searches. Details on the track selection are given in Sec. 8.2.5.

7.3 Properties of chargino tracks

There are no SM processes that predict the disappearing-track signature. Therefore, the vast majority of background events can be removed by identifying a disappearing track in the event. However, tracks with a small number of hits in the silicon detectors can be easily formed by a wrong combination of space-points originating from low-p_T charged particles that are not reconstructed, and could have anomalously high values of p_T. Such p_T-mismeasured tracks can mimic the disappearing-track signature. This section investigates ways to suppress the p_T-mismeasured tracks by comparing track properties and to enhances the search sensitivity.

Figure 7.5–7.9 show the track properties for charginos with a mean lifetime of 0.2 ns and p_T-mismeasured tracks in a QCD multi-jet enriched sample. The properties for the hadron tracks that are fully reconstructed in a QCD multi-jet enriched sample are also shown in the figure. The following requirements are commonly applied to the tracks.

The common requirements
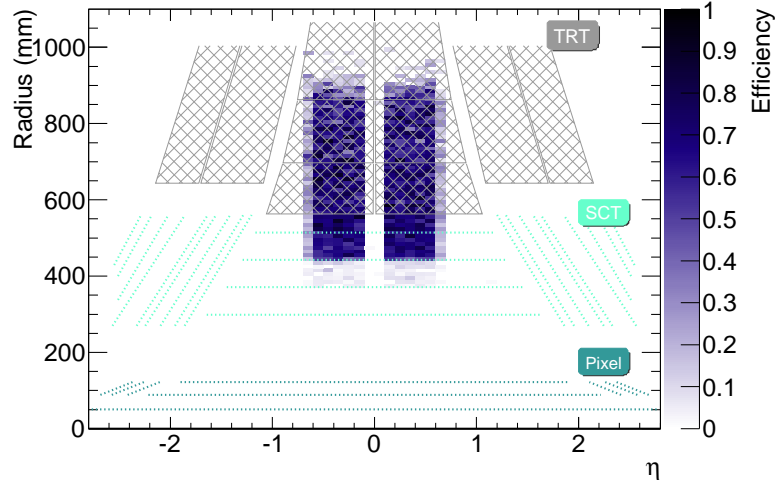
(a) ATLAS standard track reconstruction
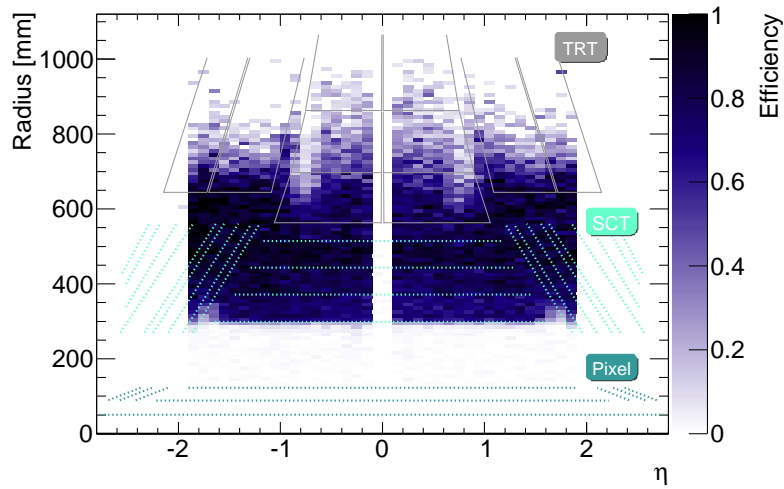
(b) Extended track reconstruction

Figure 7.4: Track selection efficiency for decaying charginos of (a) the ATLAS standard track reconstruction and (b) the extended track reconstruction with the application of the track selection requirements given in Sec. 8.2.5.

- $p_T > 15$ GeV.

- Tracks must point the TRT active region $0.1 < |\eta| < 1.9$.

- $|d_0| < 1.5$ mm.

- $|z_0 \sin\theta| < 1.5$ mm.

- $N_{b-layer} \geq 1$, if crossing an active module of the innermost pixel layer.

- $N_{pixel} \geq 1$.

- $N_{SCT} \geq 2$.

In addition to requirements listed above, the chargino signal, p_T-mismeasured tracks, and hadron tracks are required to fulfill the following criteria.

The definition of chargino tracks

- The reconstructed track is required to originate from the chargino based on the MC truth information.

The definition of p_T-mismeasured tracks

- The reconstructed track p_T must be at least two times larger than the true p_T: $(p_T{}^{rec}\text{-}p_T{}^{true})/p_T{}^{true} > 1.0$.

The definition of hadron tracks

- The track must accompany hadronic activities in the calorimeter: ΔR between the track and nearest jets with $p_T > 20$ GeV must be less than 0.1.

Properties of chargino tracks   The chargino tracks have high p_T and are well isolated from hadronic activities as shown in Fig. 7.5. The p_T-mismeasured tracks are presumably originated from low-p_T charged particles in pile-up jets, therefore, p_T-mismeasured tracks could have finite hadronic activities around them. By requiring a small hadronic activity around the candidate track, not only hadron tracks but also p_T-mismeasured tracks can be suppressed.

Concerning the hit information in the pixel detector, the pixel qualities for p_T-mismeasured tracks become poor because they are formed by a wrong combination of space-points of different particles. Therefore, the number of absent hits (holes) in the pixel detector, hits with bad track-fit qualities (outliers), and hits with broad position errors (spoilt hits) for p_T-mismeasured tracks become large compared to those for charginos and hadron tracks as shown in Fig. 7.6. A similar feature is observed in the SCT detector as shown in Fig. 7.7.

The number of hits in the SCT detector for charginos depends on the proper lifetime of the chargino. As shown in Fig. 7.7 (a), the number of SCT hits for charginos with a mean lifetime of 1.0 ns peaks at $N_{SCT} \sim 8$, while that with a mean lifetime of 0.2 ns peaks at $N_{SCT} \sim 2$.

The mechanism that makes p_T-mismeasured tracks implies that their impact parameters are randomly distributed as shown in Fig. 7.5 (e), (f), and (g). Therefore, a large amount of p_T-mismeasured tracks can be removed by requiring a small impact parameter without any loss of chargino tracks. The track-quality information of p_T-mismeasured tracks are also shown in Fig. 7.7 (e) and (f).

The energy loss information (dE/dx), provided by the pixel detector, is expected to help to identify charginos especially having high masses. Figure 7.8 shows the dE/dx for chargino tracks with various masses, p_T-mismeasured, and hadron tracks. The charginos that remain after the monojet selection applied at the trigger level are highly boosted, and p_T-mismeasured tracks could have large dE/dx as they originate from low-p_T hadrons. Therefore, the discrimination of charginos based on the dE/dx information does not work effectively.

When charginos decay before reaching the TRT detector ($R_{decay} < 563$ mm in the barrel region), N_{TRT} is expected to have a value near zero; conversely, charged particles traversing the TRT typically have $N_{TRT} \simeq 34$. Therefore, vast majority of hadron tracks can be removed by requiring few hits in the TRT detector as shown in Fig. 7.9

(a) Track p_T

(b) Track η

(c) p_T^{cone40}/p_T^{track}

(d) E_T^{cone40}/p_T^{track}

(e) $\sum_{\Delta R<0.4} E_T^{clus}/p_T^{track}$

(f) d_0

(g) d_0 significance

(h) $z_0 \sin\theta$
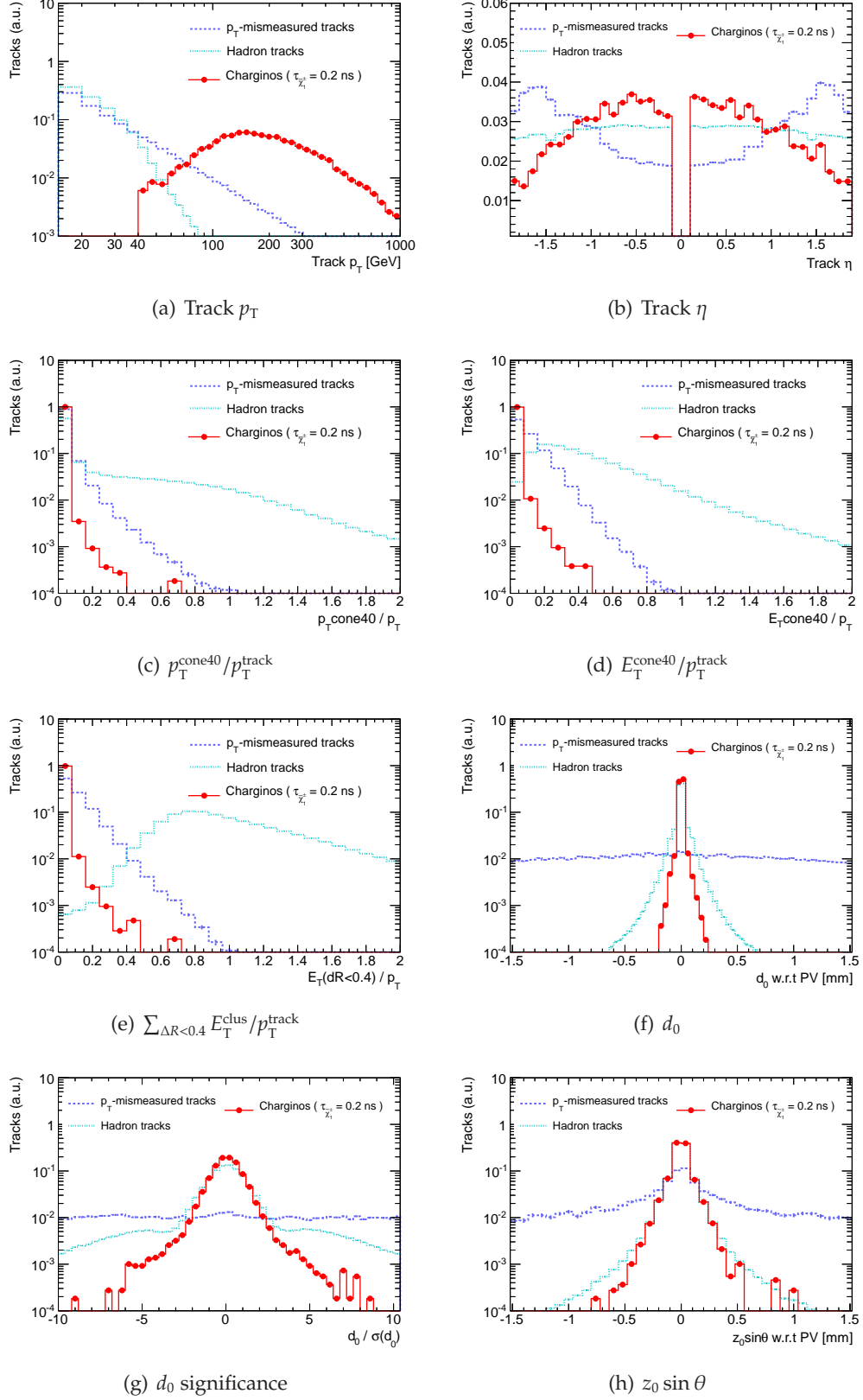
Figure 7.5: Reconstructed track p_T, η, isolation information, and impact parameter variables for charginos, p_T-mismeasured tracks, and hadron tracks in QCD multi-jet MC events.
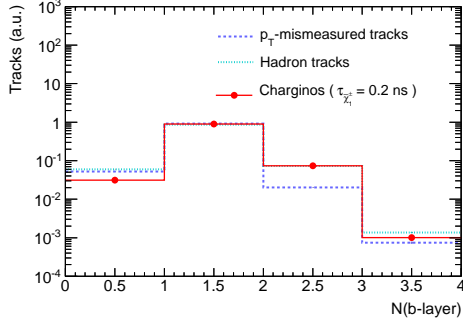
(a) Number of b-layer hits
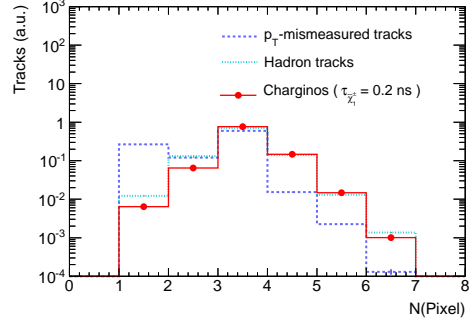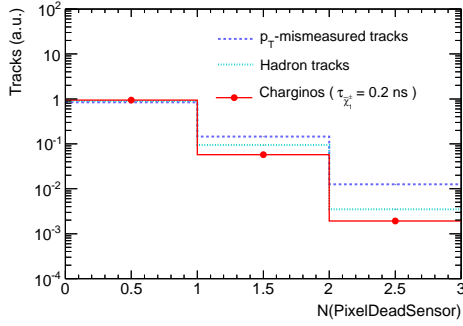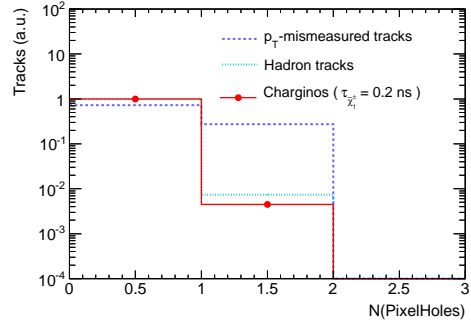
(b) Number of pixel hits

(c) Number of dead pixel sensors

(d) Number of pixel holes
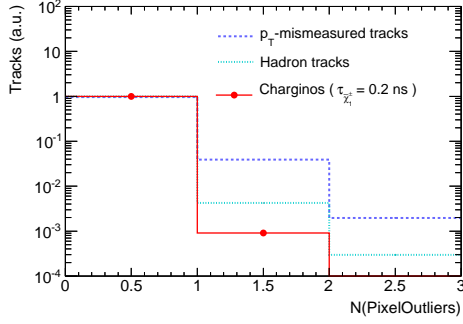
(e) Number of pixel outliers
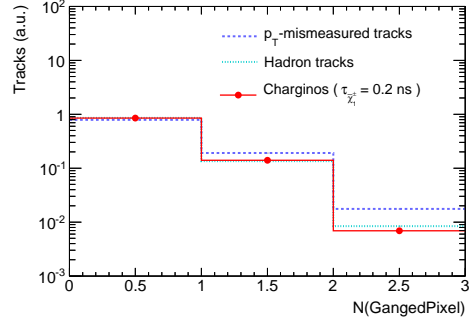
(f) Number of ganged pixel hits
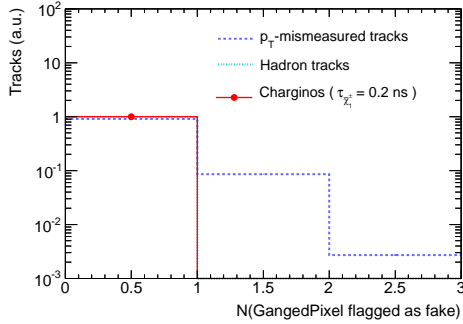
(g) Number of ganged pixel hits flagged as fake
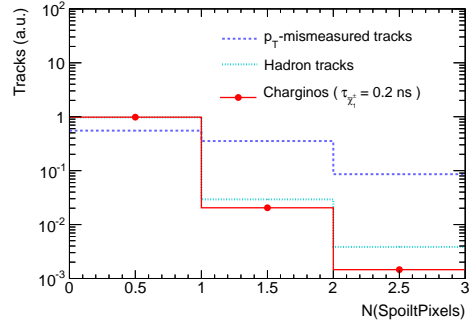
(h) Number of spoilt pixel hits

Figure 7.6: Pixel-hit variables for charginos, p_T-mismeasured tracks, and hadron tracks in QCD multi-jet MC events.

(a) Number of SCT hits

(b) Number of SCT holes

(c) Number of SCT outliers

(d) Number of spoilt SCT hits

(e) χ^2/ndf

(f) χ^2 probability
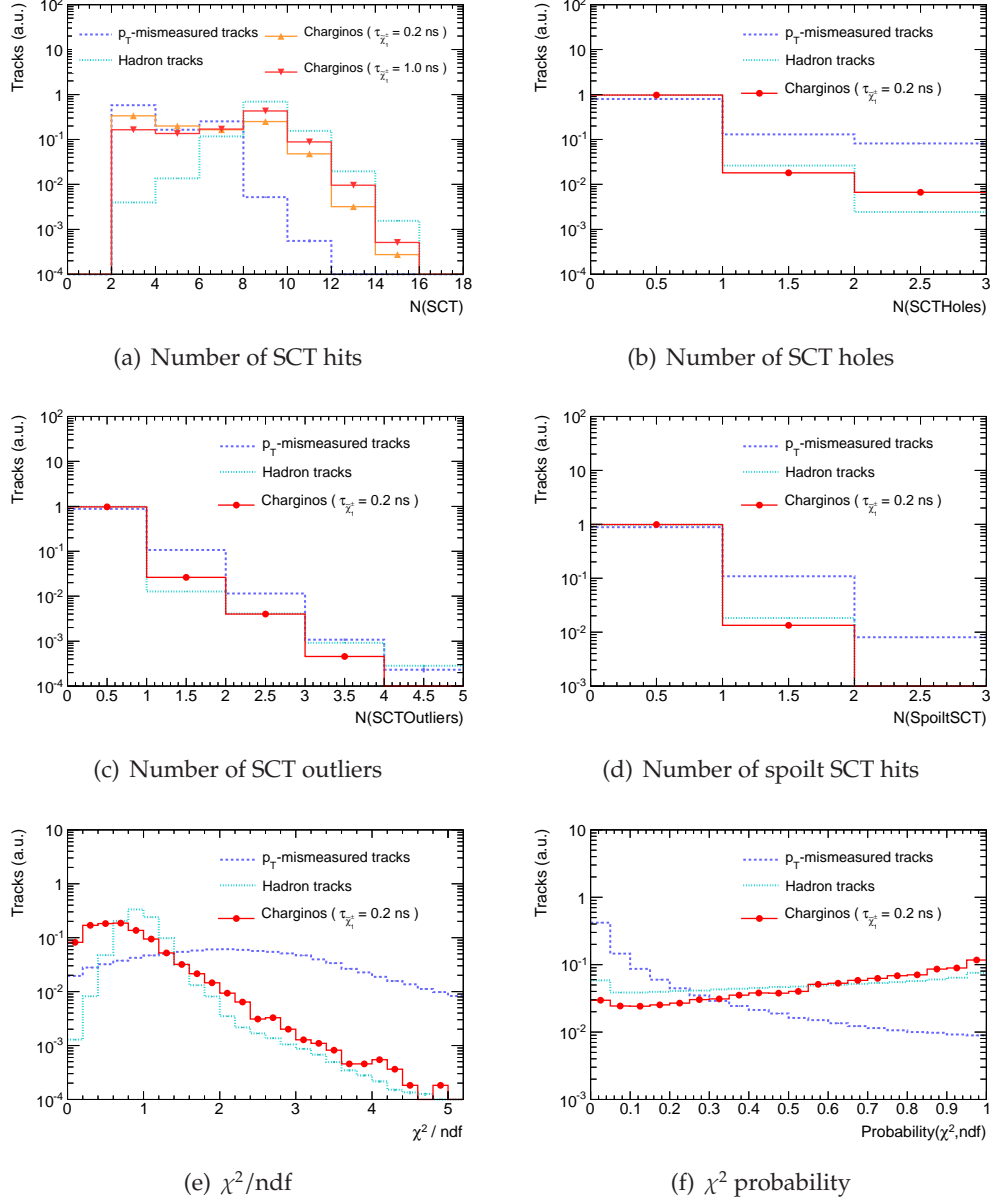
Figure 7.7: SCT-hit variables and track quality information for charginos, p_{T}-mismeasured tracks, and hadron tracks in QCD multi-jet MC events.
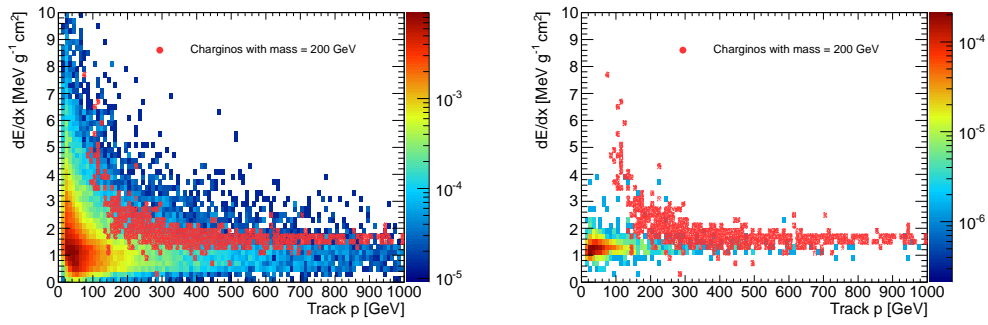
(a) The dE/dx vs track momentum for chargino tracks and p_T-mismeasured tracks

(b) The dE/dx vs track momentum for chargino tracks and hadron tracks
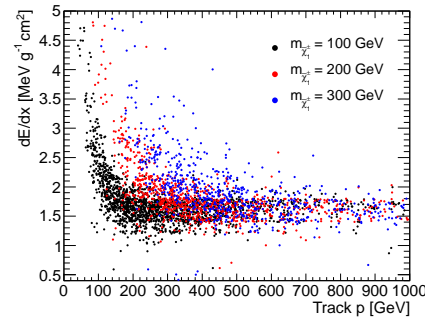
(c) The dE/dx vs track momentum for chargino tracks with various masses

Figure 7.8: The dE/dx information for charginos, p_T-mismeasured tracks, and hadron tracks in QCD multi-jet MC events.
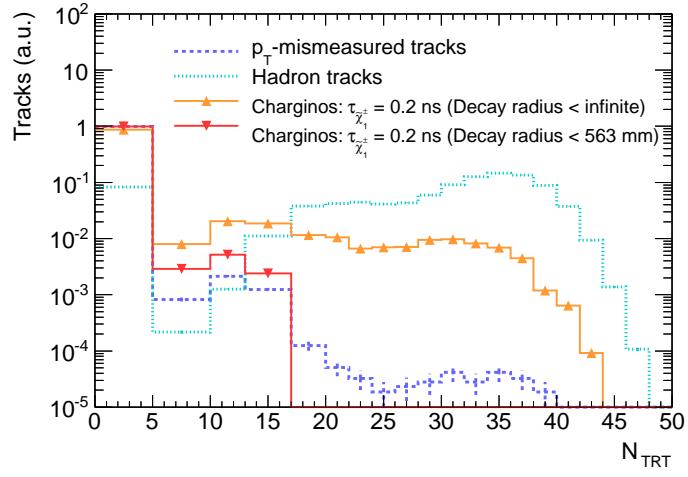
Figure 7.9: The N_{TRT} distribution for charginos, p_{T}-mismeasured tracks, and hadron tracks in QCD multi-jet MC events. When charginos decay before reaching the TRT detector ($R_{decay} < 563$ mm), N_{TRT} is expected to have a value near zero; conversely, charged particles traversing the TRT typically have $N_{\mathrm{TRT}} \simeq 34$.

Chapter 8

Event Selection

The SM processes, especially W+jet events that naturally have large $E_\mathrm{T}^\mathrm{miss}$, can result in final-state kinematics similar to that of the signal. Therefore, the signal events can not be enhanced by any kinematic selection requirements, and tight requirements on kinematics reduce the signal efficiency a lot. In this analysis, a dedicated topological trigger is developed to attain a higher signal efficiency. Kinematic selection criteria are applied to ensure a high trigger efficiency, and the vast majority of background events are removed by identifying a high-p_T disappearing track in the event.

8.1 Online selection

8.1.1 Trigger

As stated in Sec. 7.1, the signal event topology is characterized by a high–p_T jet and large $E_\mathrm{T}^\mathrm{miss}$, and they are well balanced in the transverse plane. Therefore, the analysis makes use of a dedicated topological trigger named `EF_j80_a4tchad_xe70_tclcw_dphi2j45xe10` in order to suppress a huge QCD multi-jet events and attain a higher signal efficiency than that of ATLAS standard triggers. Details on the selection requirements are described in Sec. 4.1.1.

Figure 8.1 shows the $\Delta\phi_\mathrm{min}^{\mathrm{jet}-E_\mathrm{T}^\mathrm{miss}}$ distributions for signal and SM MC events after the trigger requirement except for the $\Delta\phi_\mathrm{min}^{\mathrm{jet}-E_\mathrm{T}^\mathrm{miss}}$ selection. The signal events make up the population at $\Delta\phi_\mathrm{min}^{\mathrm{jet}-E_\mathrm{T}^\mathrm{miss}} \sim \pi$ while QCD multi-jet events have smaller values of $\Delta\phi_\mathrm{min}^{\mathrm{jet}-E_\mathrm{T}^\mathrm{miss}}$ due to the fact that $E_\mathrm{T}^\mathrm{miss}$ originates most likely from the jet–p_T mismeasurements, and $E_\mathrm{T}^\mathrm{miss}$ and the mismeasured jet are aligned in the transverse plane. This trigger helps to reject the majority of QCD multi-jet events online. As shown in Fig. 8.2, by requiring $\Delta\phi_\mathrm{min}^{\mathrm{jet}-E_\mathrm{T}^\mathrm{miss}} > 1.0$, nearly half of QCD multi-jet events can be removed without any loss of signal events with $m_{\tilde\chi_1^\pm} = 200$ GeV and $\tau_{\tilde\chi_1^\pm} = 0.2$ ns. Figure 8.3 shows estimated event rates at a peak luminosity

of 7.7×10^{33} cm^{-2}s^{-1} as a function of a threshold on a $\Delta\phi_{\text{min}}^{\text{jet}-E_{\text{T}}^{\text{miss}}}$ for QCD multi-jet events, $W \to l\nu$+jets events, $Z \to \nu\bar{\nu}$+jets events, and signal events, which indicates that the event rate can be reduced to ~ 4 Hz with $\Delta\phi_{\text{min}}^{\text{jet}-E_{\text{T}}^{\text{miss}}} > 1.0$ cut. However, a part of events is also triggered by other triggers used in ATLAS SUSY searches [12, 101] whose trigger rates are ~ 10 Hz. Table 8.1 shows overlap fractions and rate increases for QCD multi-jet events, $W \to l\nu$+jets events, and $Z \to \nu\bar{\nu}$+jets events. The actual contribution to the total event rate is reasonably small and estimated to be ~ 2 Hz.

Table 8.2 shows the trigger efficiency for signal events with $m_{\tilde{\chi}_1^\pm} = 200$ GeV and $\tau_{\tilde{\chi}_1^\pm} = 0.2$ ns. The trigger efficiencies of other triggers used in ATLAS SUSY searches are also shown. The topological trigger enables to achieve a higher efficiency than those of the standard triggers.
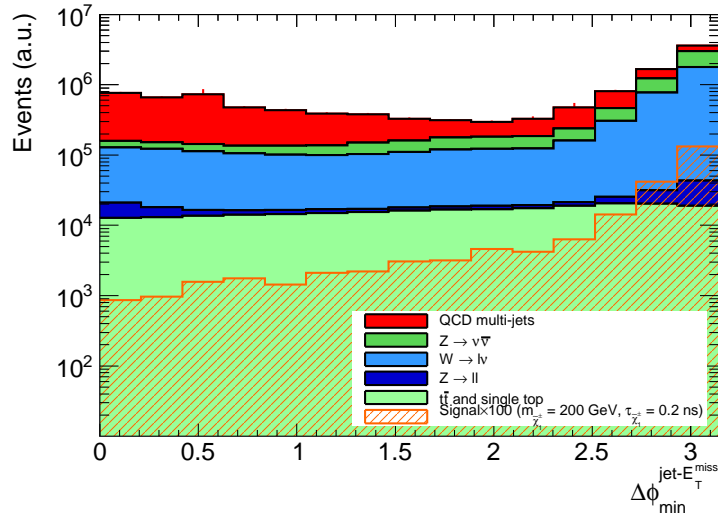
Figure 8.1: The $\Delta\phi_{\text{min}}^{\text{jet}-E_{\text{T}}^{\text{miss}}}$ distributions for signal and SM MC events.

	QCD	$W \to l\nu$	$Z \to \nu\bar{\nu}$
Overlap fraction	32 %	88 %	89 %
Rate increase	1.4 Hz	0.14 Hz	0.08 Hz

Table 8.1: Overla fraction of the topological trigger with other triggers used in ATLAS SUSY searches [12, 101]. The actual contribution to the total event rate is also shown.
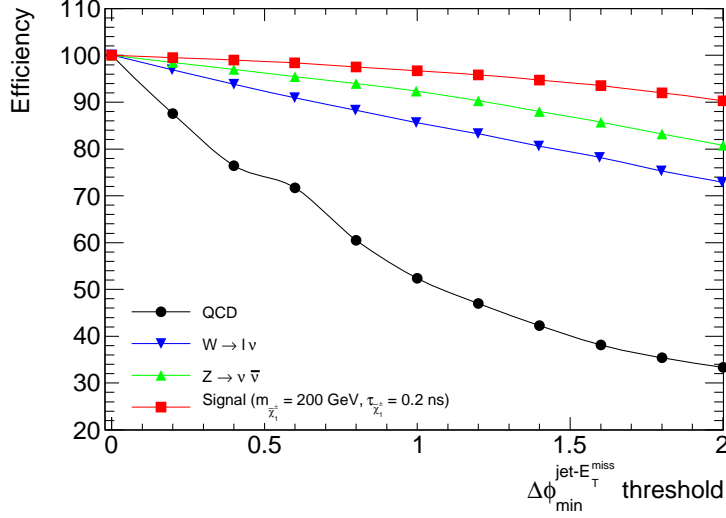
Figure 8.2: Trigger efficiencies as a function of a threshold on a $\Delta\phi_{\mathrm{min}}^{\mathrm{jet}-E_{\mathrm{T}}^{\mathrm{miss}}}$ requiremenet for QCD multi-jet events, $W \to l\nu$+jets events, $Z \to \nu\bar{\nu}$+jets events and signal events with $m_{\tilde{\chi}_1^\pm} = 200$ GeV and $\tau_{\tilde{\chi}_1^\pm} = 0.2$ ns.
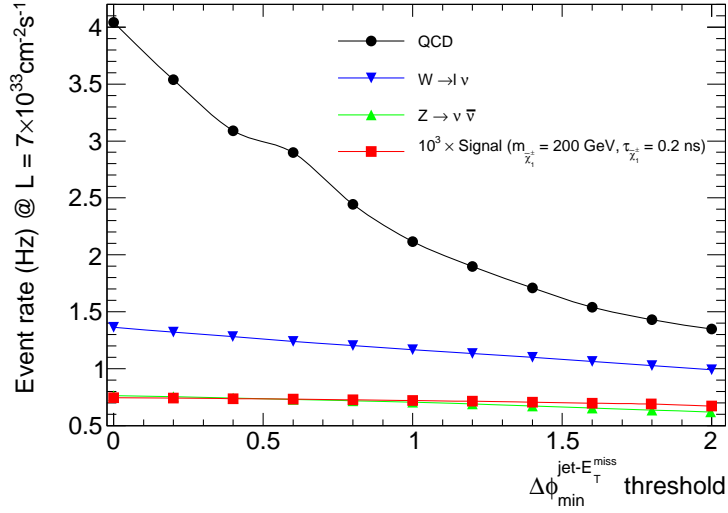
Figure 8.3: Estimated event rates at a peak luminosity of 7.7×10^{33} cm^{-2}s^{-1} as a function of a threshold on a $\Delta\phi_{\mathrm{min}}^{\mathrm{jet}-E_{\mathrm{T}}^{\mathrm{miss}}}$ requiremenet for QCD multi-jet events, $W \to l\nu$+jets events, and signal events with $m_{\tilde{\chi}_1^\pm} = 200$ GeV and $\tau_{\tilde{\chi}_1^\pm} = 0.2$ ns.

Trigger	EF_j80_a4tchad_ xe70_tclcw_ dphi2j45xe10	EF_j80_a4tchad_ xe100_tclcw_ veryloose	EF_xe80_tclcw_loose
Leading jet p_T	> 80 GeV	> 80 GeV	
E_T^{miss}	> 70 GeV	> 100 GeV	> 80 GeV
$\Delta\phi_{min}^{jet-E_T^{miss}}$	> 1.0		
Rate	~ 4 Hz	~ 2 Hz	~ 10 Hz
Signal efficiency	6.9 %	3.0 %	4.6 %

Table 8.2: Comparison of trigger efficiencies for signal events ($m_{\tilde{\chi}_1^\pm}$ = 200 GeV, $\tau_{\tilde{\chi}_1^\pm}$ = 0.2 ns) with three different triggers.

Efficiency

In order to evaluate the trigger efficiency for the signal events, a data control sample collected by the muon triggers is used. The events are required to pass the following criteria:

- Trigger : EF_mu24i_tight or EF_mu36_tight [1].

- No muons that have significantly large values of the curvature error, $|d_0|$ and $|z_0|$, which could arise from failures of reconstruction or cosmic-ray muons.

- No identified electrons with p_T > 10 GeV.

- Exact one reconstructed muon with p_T > 25 GeV and $|\eta|$< 2.4.

- p_T^{cone40}/p_T < 0.1.

- m_T > 40 GeV.

- E_T^{miss} > 40 GeV.

where m_T is the transverse mass between a lepton and E_T^{miss} defined by

$$m_T = \sqrt{2(p_T^{lepton}E_T^{miss} - \vec{p}_T^{lepton} \cdot \vec{E}_T^{miss})}. \tag{8.1}$$

These requirements remove the vast majority of QCD multi-jet events and enhance $W \rightarrow \mu\nu$+jets events.

The signal event topologies can be emulated by subtracting the muon contribution in the calculation of E_T^{miss} for the $W \rightarrow \mu\nu$+jets data control sample. Figure 8.4 (a) and (b) show the offline $\Delta\phi_{min}^{jet-E_T^{miss}}$ distributions in the $W \rightarrow \mu\nu$+jets control sample before and after the trigger requirement. The data and MC events reasonably agree, and the cut of 1.5 on $\Delta\phi_{min}^{jet-E_T^{miss}}$ places it on plateau.

---

[1] Triggers used in this analysis are summarized in Sec. 4.1.

(a) Before the trigger requirement

(b) After the trigger requirement
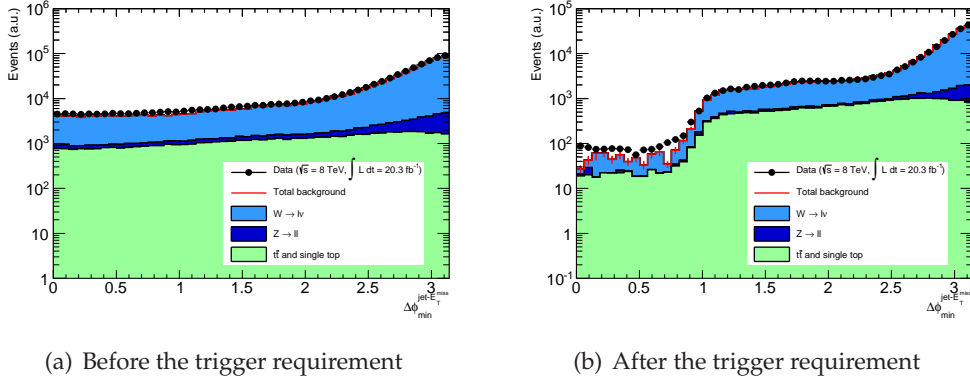
Figure 8.4: Offline $\Delta\phi_{\mathrm{min}}^{\mathrm{jet}-E_{\mathrm{T}}^{\mathrm{miss}}}$ distribution for the $W \rightarrow \mu\nu$ control sample before (a) and after (b) applying the trigger requirement.

The trigger efficiency is then given by the fraction of events passing the trigger after the application of $W \rightarrow \mu\nu$ selection criteria. Figure 8.5 (a) and (b) show the trigger efficiencies as a function of the leading jet p_{T} and $E_{\mathrm{T}}^{\mathrm{miss}}$. The requirements of $E_{\mathrm{T}}^{\mathrm{miss}} > 90\,\mathrm{GeV}$ and $p_{\mathrm{T}} > 90\,\mathrm{GeV}$ on the leading jet are applied in Fig. 8.5 (a) and (b), respectively. Two-dimensional efficiency maps and its data/MC ratio are also shown in Fig. 8.6 and 8.7, respectively. The MC simulation describes the data well, and the trigger acceptances for the data and MC events surviving the kinematic selection described in Sec. 8.2.4 agree within 4.5%; this value is assigned as a systematic uncertainty on the trigger efficiency for the signal MC events.

(a) Leading jet p_{T}
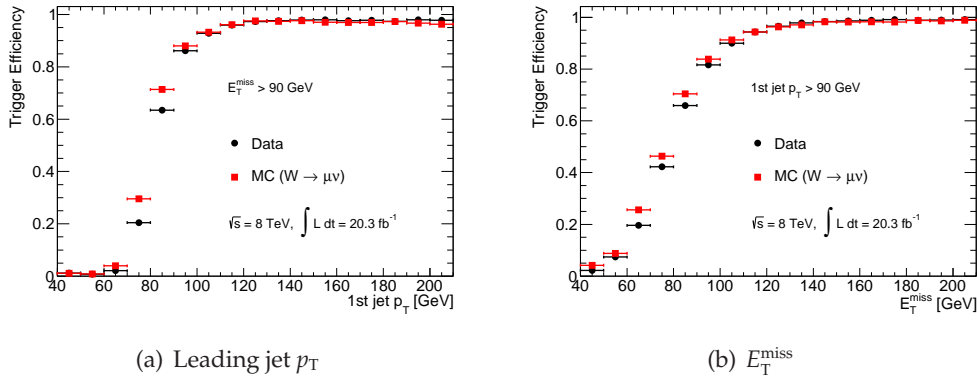
(b) $E_{\mathrm{T}}^{\mathrm{miss}}$

Figure 8.5: Trigger efficiency as a function of the leading jet p_{T} (a) and $E_{\mathrm{T}}^{\mathrm{miss}}$ (b).
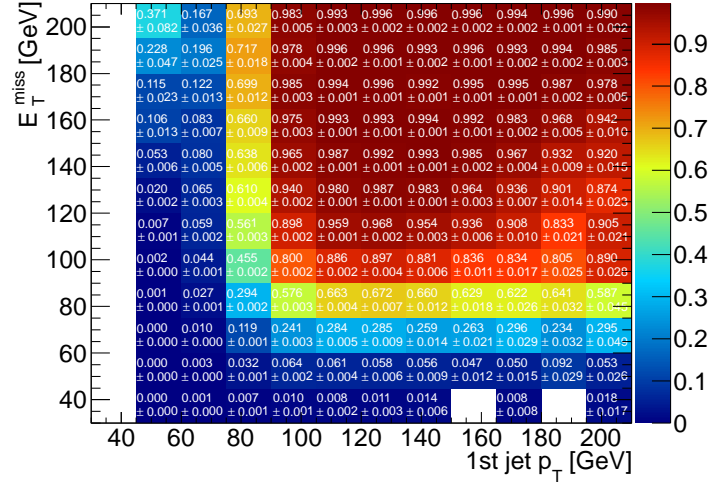
(a) Data
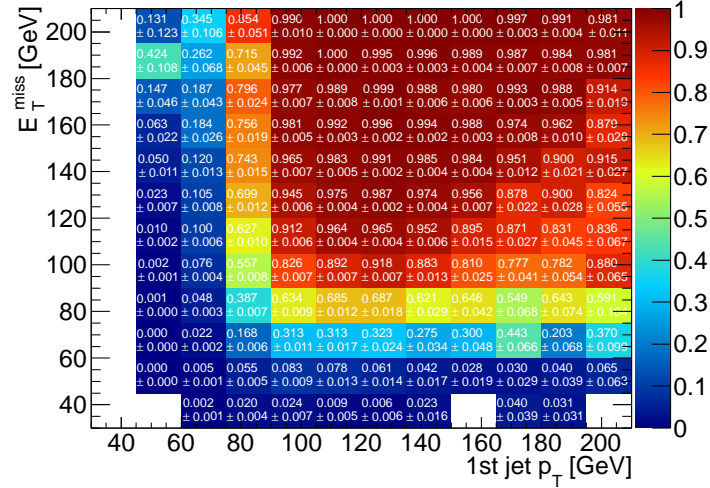
(b) MC

Figure 8.6: Trigger efficiency for the data (a) and MC events (b) as function of the leading jet p_T and $E_\mathrm{T}^\mathrm{miss}$.
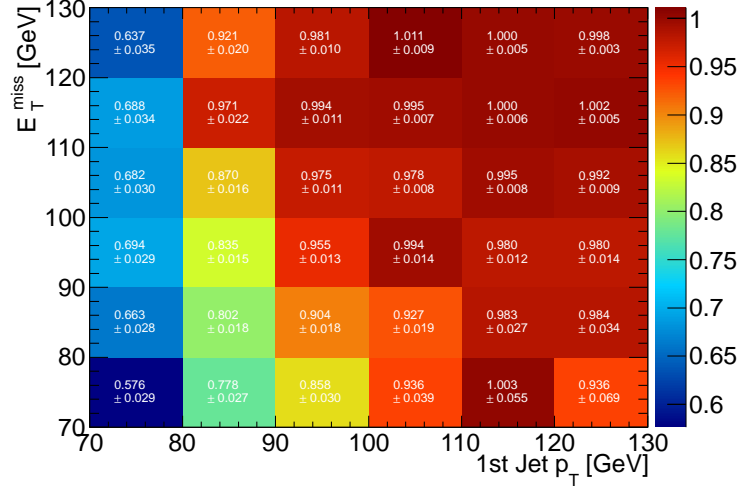
Figure 8.7: Ratio of the trigger efficiency between the data and MC events as a function of the leading jet p_T and E_T^{miss}.

8.2 Offline selection

First, rejection cuts to suppress events originating from non-collision background events are applied to reconstructed jets. The signal candidate events are then selected using kinematic variables together with the properties of disappearing tracks. This section describes the kinematic and disappearing track selection criteria. The data reduction is also summarized.

8.2.1 Primary vertex selection

The event vertex [92] is required to have at least five associated tracks with $p_T > 0.4$ GeV. When more than one such vertex is found, the vertex with the largest $\sum |p_T|^2$ of the associated tracks is chosen as primary.

8.2.2 Overlap removal

Since the physics objects described in Sec. 5 are reconstructed independently, their overlap must be resolved to avoid double counting. The overlap removal is proceeded in the following way.

1. First, a jet that overlaps with an electron is removed. If a jet is reconstructed with $\Delta R < 0.2$ of an electron, they are considered to be seeded by the same object and in this case, the object is regarded as an electron.

2. After the overlap removal, an electron with $\Delta R < 0.4$ around a jet is removed since jets are reconstructed with the distance parameter of $\Delta R = 0.4$ and it is accounted in the original jet.

3. Similarly, a muon with $\Delta R < 0.4$ around a jet is removed. Unlike the electron case, even if a muon is close to a jet, the muon deposits only a small amount of energy in the calorimeter. The removed muon is not counted as an isolated muon candidate but its momentum is included in the missing momentum calculation.

8.2.3 Event cleaning

Fake jets can be formed from non-collision background events such as beam-halo muons or cosmic-rays if the muons undergo significant bremsstrahlung in the detector. The burst-noise in the HEC and the coherent noise in the LAr EM calorimeter could also be reconstructed as fake jets. A set of requirements are designed to have a high rejection against such fake jets while keeping an inefficiency of jets originating from pp collisions $\sim 0.1\,\%$ [102]. These selection requirements are based on the timing information, the pulse shape, the fraction of energy deposited in specific calorimeter layers, and the information of tracks associated with the jets. Events are rejected if any jets that have $p_T > 20$ GeV and fail to pass any of the rejection requirements.

8.2.4 Kinematic selection criteria

In order to suppress background events from W/Z + jets and top-pair production processes, events are discarded if they contain any electron or muon candidates (lepton veto). Events containing muons are further suppressed by requiring no tracks with $p_T > 10$ GeV reconstructed in the MS (stand-alone muon veto). The candidate events are required to have $E_T^{\mathrm{miss}} > 90$ GeV and at least one jet with $p_T > 90$ GeV. In order to further suppress the QCD multi-jet events, $\Delta\phi_{\mathrm{min}}^{\mathrm{jet}-E_T^{\mathrm{miss}}} > 1.5$ is also required.[2] The trigger selection is $> 98\%$ efficient for signal events satisfying these selection requirements.

Figure 8.8 (a),(b), (c), and (d) show the distributions of leading jet p_T, E_T^{miss}, $\Delta\phi_{\mathrm{min}}^{\mathrm{jet}-E_T^{\mathrm{miss}}}$, and the number of jets with $p_T > 45$ GeV after applying all the kinematic selection requirements and requiring at least one isolated track with $p_T > 15$ GeV. At this stage, the background events dominate in the search, however, the vast majority of these backgrounds are removed by identifying a disappearing track.

---

[2]If the event has only one jet with $p_T > 45$ GeV, $\Delta\phi_{\mathrm{min}}^{\mathrm{jet}-E_T^{\mathrm{miss}}}$ is calculated using the leading jet only.

(a) Leading jet p_T

(b) $E_\mathrm{T}^\mathrm{miss}$

(c) $\Delta\phi_\mathrm{min}^{\mathrm{jet}-E_\mathrm{T}^\mathrm{miss}}$

(d) Number of jets with $p_\mathrm{T} > 45$ GeV
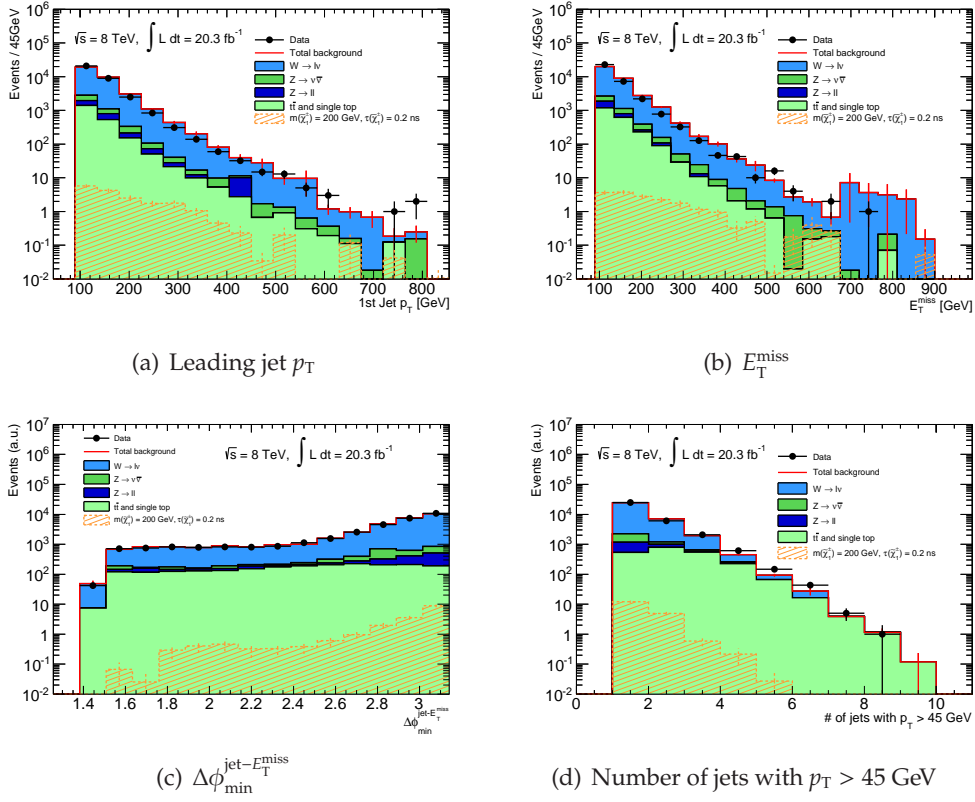
Figure 8.8: Distributions of leading jet p_T, $E_\mathrm{T}^\mathrm{miss}$, $\Delta\phi_\mathrm{min}^{\mathrm{jet}-E_\mathrm{T}^\mathrm{miss}}$, and the number of jets with $p_\mathrm{T} > 45$ GeV after all the kinematic selection cuts and requiring at least one isolated track.

8.2.5   Disappearing track selection

As shown in Fig. 7.5–7.9, the tracks originating from charginos are expected to have high p_T, to be isolated, and to have few associated hits in the outer region of the ID. The TRT detector, in particular, provides substantial discrimination against penetrating stable charged particles if only a small number of hits on the track is required. Therefore, candidate tracks for decaying charginos are required to fulfill the following criteria:

(I) the track must have $N_{pixel} \geq 1$, $N_{b\text{-layer}} \geq 1$ if crossing an active module of the innermost pixel layer, $N_{SCT} \geq 2$, $|d_0| < 0.1$ mm, and $|z_0 \sin \theta| < 0.5$ mm.

(II) the track reconstruction must be of good quality, meeting the following requirements: it must have a track fit χ^2-probability of $> 10\%$, no hits formed in a single pixel row of which the readout is shared with another pixel (the number of ganged pixel hits flagged as fake is required to be zero), and no hits missing in active silicon modules along the trajectory between the first and last hit of the track (the number of holes in the silicon detectors is required to be zero).

(III) the track must be isolated: it must fulfill $p_T^{cone40}/p_T < 0.04$. There must also be no jets having p_T above 45 GeV within a cone of $\Delta R = 0.4$ around the candidate track.

(IV) the candidate track must have p_T above 15 GeV, and must be the highest-p_T isolated track in the event.

(V) the candidate track must satisfy $0.1 < |\eta| < 1.9$.

(VI) the number of TRT hits associated with the track N_{TRT}, determined by counting hits lying on the extrapolated track, must be less than five.

These selections are determined by comparing the properties of chargino tracks with those of background tracks as shown in Fig. 7.5–7.9. Criteria (I) and (II) are applied in order to ensure well-reconstructed primary tracks. Criteria (III) and (IV) are employed to select chargino tracks that are isolated and have in most cases the highest p_T. These criteria also substantially reduce background tracks from the pile-up. Criterion (V) is used to ensure coverage by the TRT active region and enhance the rejection of background tracks. Criterion (VI) helps to remove the majority of background tracks in SM processes, as shown in Fig. 8.9. For SM charged particles traversing the TRT detector, the number of TRT hits is typically $N_{TRT} \simeq 32$, whereas for charginos that decay before reaching the TRT the expected is $N_{TRT} \simeq 0$. The distributions for different η regions are also shown in Fig. 8.10. Hereafter, "high-p_T isolated track selection" and "disappearing-track selection" indicate criteria (I)–(V) and (I)–(VI), respectively.

A summary of track selection requirements and the data reduction are given in Table 8.3. After the application of all kinematic and disappearing-track selection criteria, 3256 candidate events remain.
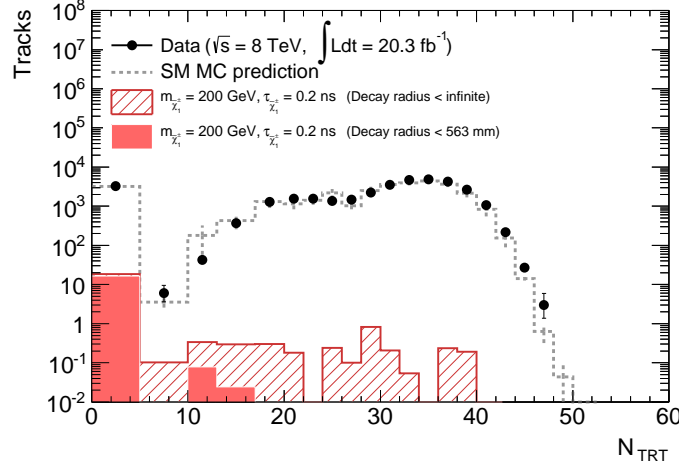
Figure 8.9: The N_{TRT} distribution for data and signal MC events ($m_{\tilde{\chi}_1^\pm} = 200$ GeV, $\tau_{\tilde{\chi}_1^\pm} = 0.2$ ns) with the high-p_{T} isolated track selection. The expectation from SM MC events is also shown. The solid colored histogram shows the expected distribution for charginos with a decay radius < 563 mm while the hatched histogram shows it for all charginos for these mass and lifetime values. Tracks with $N_{\text{TRT}} < 5$ in SM events, mimicking the decaying-chargino signature, are described in Chapter 9.

The breakdown of the background processes and their origins, derived by the MC simulation, are given in Table 8.4 and 8.5, respectively, showing that the primary contribution comes from charged hadrons predominantly in $W(\rightarrow \tau\nu)$+jets processes.

The fraction of background events remaining after the kinematic and disappearing-track selection criteria is significantly small; a background estimation based on the MC simulation would suffer from large uncertainties due to the poor statistics. There is also a difficulty simulating the properties of background tracks. Therefore, a data-driven approach is employed to estimate the background track-p_{T} spectrum after the application of all the selection requirements, in particular the disappearing track selection. Detailed descriptions of the background estimation procedure are given in Chapter 9.
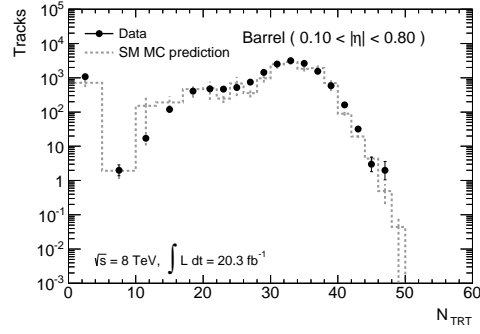
(a) $0.1 < |\eta| \le 0.8$
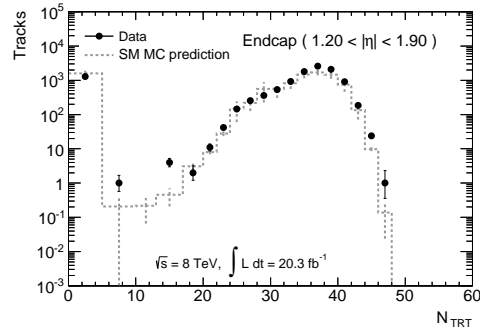
(b) $1.2 < |\eta| \le 1.9$
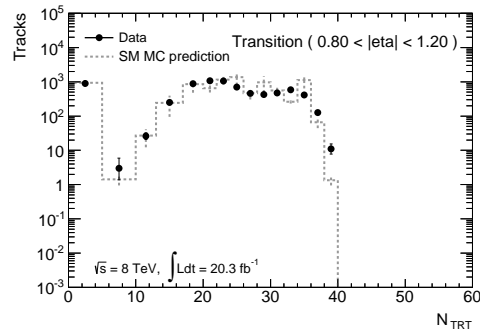
(c) $0.8 < |\eta| \le 1.2$

Figure 8.10: The N_{TRT} distribution of high-p_{T} isolated tracks pointing to the TRT barrel (a), endcap (b), and transition (c) regions for data. The expectation from SM MC events is also shown.

Selection requirement	Observed events	Expected signal MC events (efficiency [%])
Quality requirements and trigger	20479553	1873 (8.8)
Jet cleaning	18627508	1867 (8.8)
Lepton veto	12485944	1827 (8.6)
Leading jet $p_T > 90$ GeV	10308840	1571 (7.4)
$E_T^{miss} > 90$ GeV	6113773	1484 (7.0)
$\Delta\phi_{min}^{jet-E_T^{miss}} > 1.5$	5604087	1444 (6.8)
High-p_T isolated track selection	34379	21.9 (0.10)
Disappearing-track selection	3256	18.4 (0.087)

Table 8.3: Summary of selection requirements and data reduction for data and expected signal events ($m_{\tilde{\chi}_1^\pm} = 200$ GeV, $\tau_{\tilde{\chi}_1^\pm} = 0.2$ ns). The signal selection efficiencies are also shown in parentheses. Signal efficiencies are low at the first stage due to the trigger based on a jet from initial-state radiation.

MC process	Fraction [%]
$W(\to e\nu)$+jets	10.6
$W(\to \mu\nu)$+jets	4.1
$W(\to \tau\nu)$+jets	71.5
$Z(\to ee)$+jets	0.01
$Z(\to \mu\mu)$+jets	0.17
$Z(\to \tau\tau)$+jets	2.7
$Z(\to \nu\bar{\nu})$+jets	4.1
$t\bar{t}$	5.5
single top	1.3

Table 8.4: Contribution of individual SM background processes to the total background after the application of the kinematic selection requirements and the high-p_T isolated track selection.

Track origin	Fraction [%]
Charged hadron tracks	83.9
Electron tracks	12.2
Muon tracks	3.4
p_T-mismeasured tracks	0.5

Table 8.5: Origins of the background tracks and their contribution to the total background after the application of the kinematic selection requirements and the high-p_T isolated track selection.

Chapter 9

Background Estimation

Charged hadrons, leptons in the SM processes, and p_T-mismeasured tracks remain after the application of the high–p_T isolated track selection requirements and a fraction of them could be reconstructed as disappearing tracks. Background track mechanisms are categorized as follows:

- Charged hadrons interacting with the materials of the SCT detector.

- Charged leptons failing to satisfy their identification criteria.

- Low-p_T charged particles whose p_T is badly measured due to the scattering by material of the ID.

The first category is labeled as "high–p_T interacting-hadron tracks", predominantly originating from τ hadronic decays. The charged lepton background tracks originate most likely due to large bremsstrahlung or scattering before reaching the TRT detector; the large contribution comes from low–p_T electrons. The p_T-mismeasured tracks could remain after all event selection and have anomalously high values of p_T. Figure 9.1 shows an illustration of these disappearing high–p_T tracks.

Interacting-hadron and electron tracks are responsible for the background in the range $p_T < 50$ GeV, whereas p_T-mismeasured tracks are dominant for $p_T > 100$ GeV. A small contribution from muon tracks is expected throughout the full p_T range.

A background estimation based on the MC simulation has difficulty accurately describing the properties of these background tracks. Therefore, the background contribution to the disappearing-track candidates is estimated using techniques that do not rely on the MC simulation. Each of background tracks shows a distinctive p_T spectrum; the track p_T is used as the final discriminant. A simultaneous fit is performed for the extraction of the signal yield using the observed p_T spectrum and templates of background-track p_T spectra produced from dedicated control data samples.

This section introduces data-driven techniques to estimate the p_T spectrum for each background component.

107
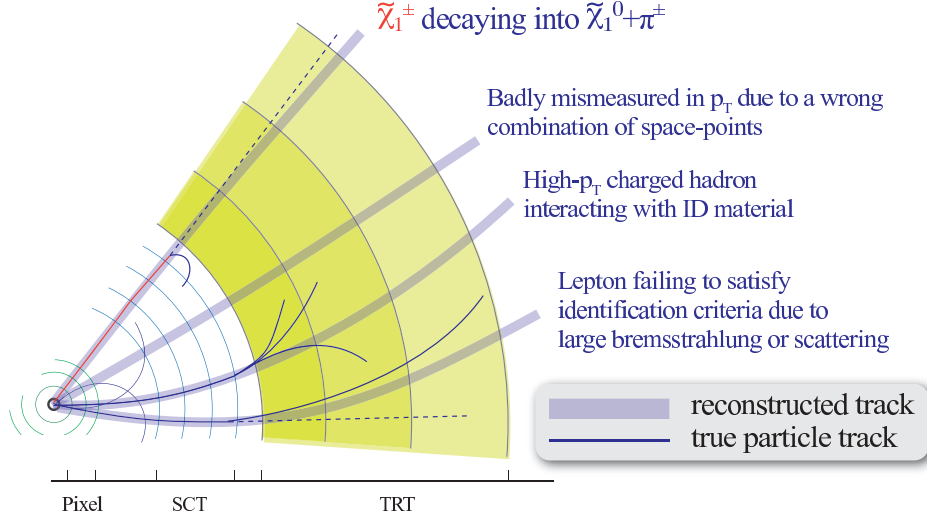
Figure 9.1: Origins of high-p_T disappearing tracks

9.1 Interacting-hadron tracks

9.1.1 Control sample for interacting-hadron tracks

Figure 9.2 shows an event display of an interacting-hadron track that is reconstructed as a disappearing track. A template of track-p_T spectrum of interacting-hadron tracks is derived based on the fact that the shape of the p_T distribution of interacting-hadron tracks is the same as that of non-interacting-hadron tracks. In the p_T range above 15 GeV, where inelastic interactions dominate, the interaction rate has nearly no dependence on p_T [21], which is also confirmed by the detector simulation as shown in Fig. 9.3.

A pure data control sample of high-p_T non-interacting-hadron tracks is obtained as follows:

1. Apply the same kinematic selection requirements as for the signal search sample.

2. Require the leading track to have $N_{TRT} > 25$ to ensure that charged particles penetrate the TRT detector without any interactions.

3. Require the leading track to have an associated calorimeter activity: $E_T^{cone40} > 7.5$ GeV and $\sum_{\Delta R < 0.4} E_T^{clus}/p_T^{track} > 0.4$.

Figure 9.4 (a) and (b) show the E_T^{cone40} and $\sum_{\Delta R < 0.4} E_T^{clus}/p_T^{track}$ distributions for hadronically decaying taus, charged hadrons in QCD multi-jet events, electrons, muons, and decaying charginos, respectively. By applying the selection requirements defined above, a pure data sample of non-interacting-hadron tracks is obtained; the contamination of electrons and muons is estimated to be negligible
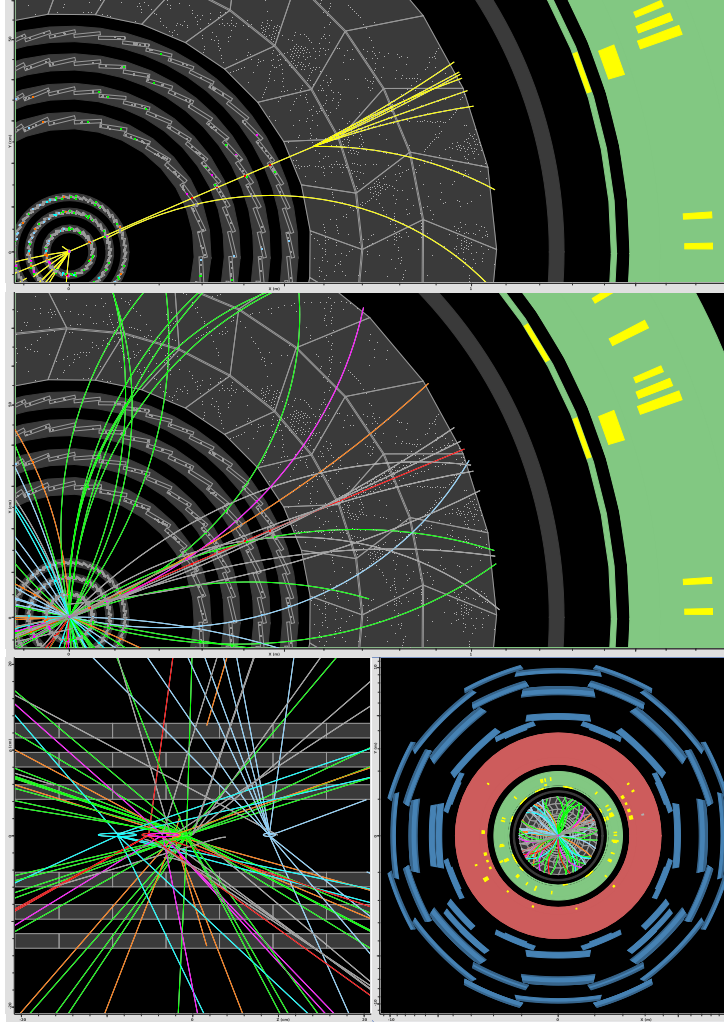
Figure 9.2: Event display of a MC event containing an interacting-hadron track. The upper (middle) figure shows a true (reconstructed) charged hadron interacting with the TRT detector. The corresponding reconstructed track is indicated by a red solid line.

($< 1\%$). A validation of this approach is performed using the $W \rightarrow \tau\nu$ MC sample, since the interacting-hadron track background in the signal search sample predominantly comes from hadronically decaying taus in W+jets events as shown in Table 8.4. Figure 9.5 shows the p_T distribution of isolated hadron tracks in $W \rightarrow \tau\nu$ MC events with the requirements that are applied in the signal search and the control sample, showing no difference of the p_T shape between each other.
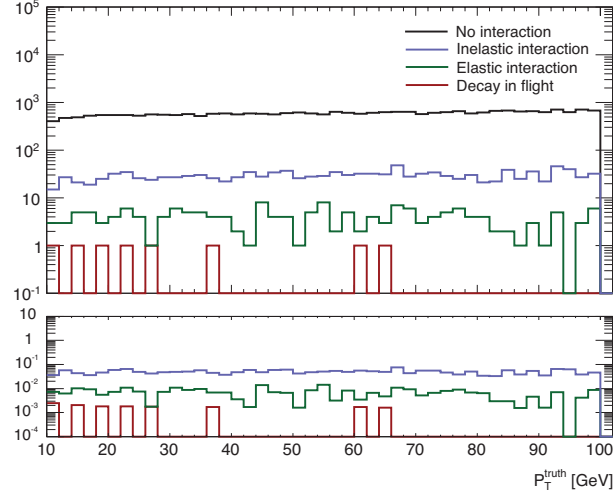
Figure 9.3: True p_T distribution of charged pions for each type of interaction. The ratios with respect to the non-interacting hadrons are also shown in the bottom figure.

9.1.2 Extraction of p_T shape

The interacting-hadron tracks show a steeply falling p_T spectrum with a high-p_T tail, which is "power low with exponential tail cutoff" like. However, the contribution of this background to the disappearing-track candidates having $p_T >$ 100 GeV is negligibly small due to the overlap removal with jets with $p_T > 45$ GeV. In order to develop a data-driven p_T spectrum of the high-p_T interacting-hadron tracks, an ansatz functional form

$$f(x) = \frac{(x + a_0)^{a_1}}{x^{a_2 + a_3 \ln(x)}},$$ (9.1)

is fitted to the p_T spectrum of the control data sample of the high-p_T non-interacting-hadron tracks, where $x \equiv p_T^{\text{track}}$ and a_i ($i = 0, 1, 2$) are fit parameters. Figure 9.6 shows the track p_T distribution and the p_T shape derived by a maximum likelihood fit. The data is well-described by this functional form; χ^2 per degree of freedom of 25.2/50 is calculated from the difference between the data and the best-fit form.

The resulting parameters and the 3×3 covariance matrix are given as

$$a_i = \begin{pmatrix} 7.45 & \pm & 0.20 \\ 75.9 & \pm & 0.76 \\ 1.16 & \pm & 0.63 \\ 9.40 & \pm & 0.08 \end{pmatrix},$$ (9.2)

(a) $\sum_{\Delta R < 0.4} E_T^{clus}/p_T^{track}$
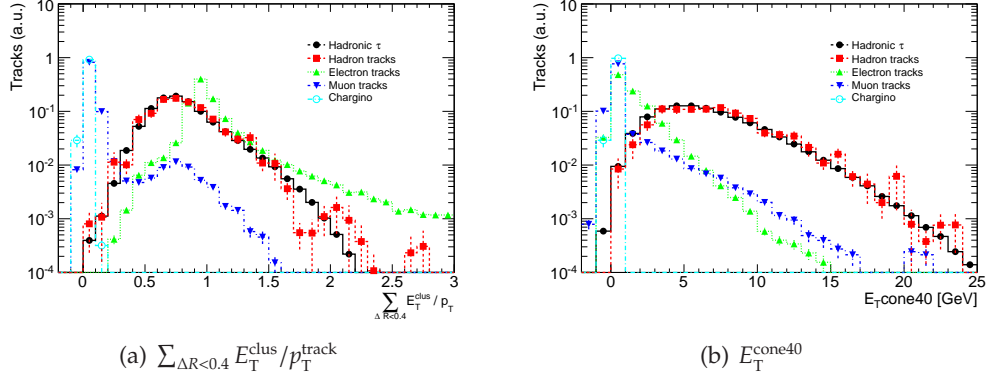
(b) E_T^{cone40}

Figure 9.4: The $\sum_{\Delta R < 0.4} E_T^{clus}/p_T^{track}$ and E_T^{cone40} distributions.
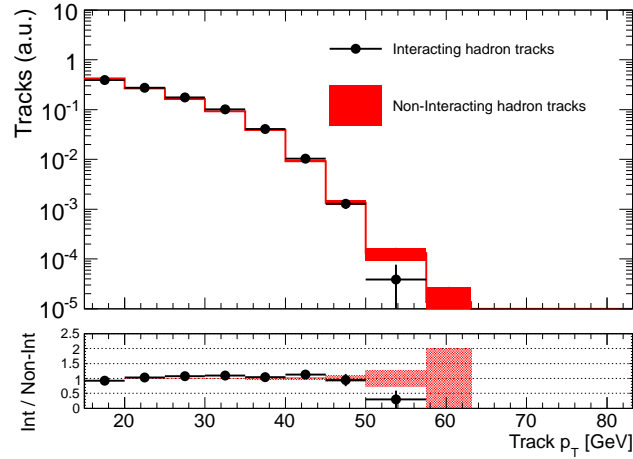
Figure 9.5: The p_T distribution of hadron tracks for $W \to \tau\nu$ MC samples with the requirement for the interacting-hadron tracks and non-interacting-hadron tracks.
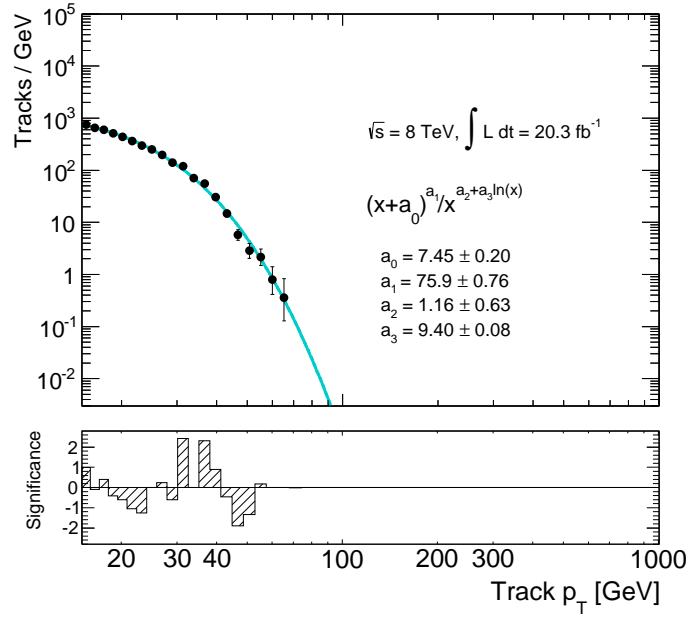
Figure 9.6: The p_T distribution of hadron track background control sample. The data and the fitted shape are shown by solid circles and a line with a error band, respectively. The significance of the data-model difference on a bin-by-bin basis is also shown at the bottom of the figure.

$$\text{cov}(a_i, a_j) = \begin{pmatrix} & 0 & 1 & 2 & 3 \\ \hline 0 & 3.84 \times 10^{-2} & 1.06 \times 10^{-2} & -6.97 \times 10^{-2} & 1.22 \times 10^{-3} \\ 1 & 1.06 \times 10^{-2} & 5.79 \times 10^{-1} & 2.19 \times 10^{-1} & 3.17 \times 10^{-2} \\ 2 & -6.97 \times 10^{-2} & 2.19 \times 10^{-1} & 3.97 \times 10^{-1} & -1.61 \times 10^{-2} \\ 3 & 1.22 \times 10^{-3} & 3.17 \times 10^{-2} & -1.61 \times 10^{-2} & 5.98 \times 10^{-3} \end{pmatrix}. \quad (9.3)$$

The values of the correlation coefficients between the parameters, $\rho_{ij} (\equiv \text{cov}(a_i, a_j)/\sigma_i \sigma_j$, where σ_i is the error on a_i), are also given as

$$\rho_{ij} = \begin{pmatrix} & 0 & 1 & 2 & 3 \\ \hline 0 & 1.000 & 0.071 & -0.565 & 0.080 \\ 1 & 0.071 & 1.000 & 0.456 & 0.539 \\ 2 & -0.565 & 0.456 & 1.000 & -0.330 \\ 3 & 0.080 & 0.539 & -0.330 & 1.000 \end{pmatrix}. \quad (9.4)$$

9.2 Leptons failing to satisfy identification criteria

A small fraction of charged leptons ($\ell \equiv e$ or μ) lose much of their momenta in the ID due to scattering by material or large bremsstrahlung. Such leptons are unlikely to be correctly identified and may be classified as disappearing tracks.

The contribution of unidentified electron tracks in the high-p_T region is negligibly small because they are reconstructed as jets and are rejected by resolving object overlaps. The effect of bremsstrahlung for muons is considerably small compared to that for electrons, but tiny detection inefficiencies lead to a fractional contribution to the background in the high-p_T region of the candidate tracks. These muon tracks can not be reconstructed as any other objects, therefore they can not be rejected by resolving object overlaps.

In order to estimate the track-p_T spectrum of lepton tracks, a control data sample is defined by adopting the kinematic selection identical to those for the signal search sample[1], while requiring one lepton that fulfills both its identification criteria and the isolated track selection criteria. The p_T spectrum of true leptons, without any identification requirements, is obtained by applying a correction for the identification efficiency. The p_T distribution of lepton background tracks is then estimated by multiplying this distribution by the probability ($\mathcal{P}_\ell^{\text{dis}}$) of failing to satisfy the lepton identification criteria (hence being retained in the signal search sample) and passing the disappearing-track selection criteria. To sum up, the track-p_T spectrum of lepton background tracks is estimated with the following equation;

---

[1]In order to mimic E_T^{miss} in the signal search sample, muons are treated like ν in the calculation of E_T^{miss}.

$$N_\ell^{\text{SR}}(p_{\text{T}}) = \frac{N_\ell^{\text{CR}}(p_{\text{T}})}{\epsilon(p_{\text{T}}, \eta, \phi)} \times \mathcal{P}_\ell^{\text{dis}}(p_{\text{T}}, \eta, \phi), \tag{9.5}$$

$$\mathcal{P}_\ell^{\text{dis}} \equiv \left(1 - \epsilon(p_{\text{T}}, \eta, \phi)\right) \times \mathcal{P}_{N_{\text{TRT}}<5}^\ell(p_{\text{T}}), \tag{9.6}$$

where $N_\ell^{\text{SR(CR)}}$, $\mathcal{P}_{N_{\text{TRT}}<5}^\ell$, and ϵ are the number of events in the signal search (control) sample, the probability of having $N_{\text{TRT}} < 5$, and the identification efficiency, respectively. Figure 9.7 shows the identification efficiencies of electrons and muons, and the average efficiencies for electrons and muons are $\sim 70\,\%$ and $\sim 94\,\%$, respectively. According to the MC simulation, the purity of electrons and muons in each control samples is close to 100% with these requirements.

(a) Electron   (b) Muon
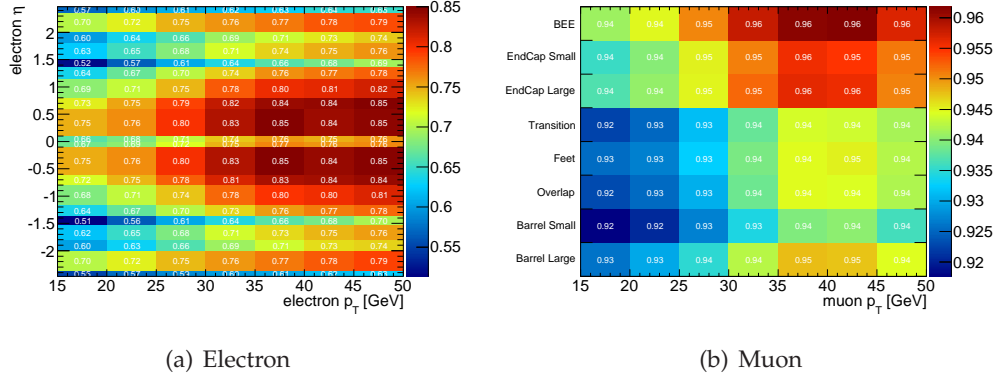
Figure 9.7: Two-dimensional identification efficiency map for electrons (a) and muons (b).

The following sections give details on the measurements of $\mathcal{P}_\ell^{\text{dis}}$.

9.2.1 Probability of identifying a lepton as a disappearing track

The probability of identifying a lepton as a disappearing track, $\mathcal{P}_\ell^{\text{dis}}$, is measured by the "tag and probe" method using $Z \to \ell\ell$ events. The object definitions for tag and probe leptons and the event selection criteria to enhance $Z \to \ell\ell$ events are summarized below. Tag leptons are required to be well isolated from jets and to fulfill the lepton identification criteria.

Definition of tag electrons

- $p_{\text{T}} > 25$ GeV and $|\eta| < 2.47$.

- Not pointing to the crack region ($1.37 < |\eta| < 1.52$).

- Satisfying the `Tight` identification criteria.

- $p_T^{cone40}/p_T < 0.1$, $| d_0 | < 1$ mm, and $| z_0 | < 2$ mm.

Definition of tag muons

- Satisfying the combined muon criteria.
- $p_T > 25$ GeV and $| \eta | < 2.4$.
- $p_T^{cone40}/p_T < 0.1$.

Definition of probe leptons

- Reconstructed tracks that fulfill the requirements on the high-p_T isolated tracks described in Sec. 8.2.5.

Event selection for $Z \rightarrow \ell\ell$ events

- Trigger (Electron): `EF_e24vhi_medium1` or `EF_e60_medium1`.
- Trigger (Muon): `EF_mu24i_tight` or `EF_mu36_tight`.
- Jet quality requirements.
- At least one reconstructed primary vertex with a minimum of five tracks with $p_T > 0.4$ GeV.
- No identified muons (electrons) for the $Z \rightarrow ee$ ($Z \rightarrow \mu\mu$) channel.
- At least one tag lepton and one isolated track.
- $|m_{\ell\ell} - m_Z| < 5$ GeV, where $m_{\ell\ell}$ and m_Z are the reconstructed invariant mass calculated using the tag lepton and the probe track momenta ($\vec{p}^{\,probe}$) and the mass of Z boson, respectively.

Figure 9.8 and 9.9 show the m_{ee} and $m_{\mu\mu}$ distributions for each p_T^{probe} range in comparison with the prediction based on $Z \rightarrow \ell\ell$ MC events, showing a reasonable agreement between each other in the region $|m_{\ell\ell} - m_Z| < 5$ GeV.

Since $\mathcal{P}_{dis}^{\mu}$ gives a very tiny value for muons, the interacting-hadron tracks (predominantly in $W \rightarrow \mu\nu$ + jets events) also contribute to the ensemble of probe tracks. Therefore, in order to suppress the interacting-hadron track contamination and ensure a pure sample of probe muons, an additional requirement of $E_T^{cone40}/p_T < 0.18$ is applied.

The probability $\mathcal{P}_{\ell}^{dis}$ is finally given by the fraction of events in which the probe lepton passes the disappearing-track selection criteria. Figure 9.10 shows the resulting probability of identifying an electron as a disappearing track as a function of p_T, showing a good agreement with the MC prediction. In the muon channel, there are no sufficient statistics of MC events to estimate the probability

for probe muons due to its tiny probability, therefore, it is estimated only using data as shown in Fig. 9.11. The probability ranges between 10^{-2}–10^{-4} for electrons and 10^{-4}–10^{-5} for muons. Since the unidentified muon background in the high-p_T region is led by the detection inefficiencies and $\mathcal{P}_{dis}^{\mu}$ is largely independent of p_T, one common value of $\mathcal{P}_{dis}^{\mu}$ is used for the p_T region above 50 GeV, which is validated by checking single-muon MC samples in which its truth p_T ranges up to 1000 GeV.

9.2.2 p_T spectrum of lepton background tracks

Figure 9.12 shows the resulting p_T spectrum of lepton background tracks derived by the data-driven method previously described. The systematic uncertainties, which are given in Sec. 9.2.3, are incorporated in the p_T spectrum. The numbers of electron and muon background tracks in the signal search sample are estimated to be 883 ± 35 and 22 ± 8, respectively. The complicated p_T spectrum of muon background track is caused by the kinematic selection in the signal search sample. In this analysis, leading jet and E_T^{miss} are required to be back-to-back in the ϕ-plane, and the unidentified muons make the large component of E_T^{miss}. Therefore, the p_T spectrum of muon background track is susceptible to the leading jet p_T spectrum, and resulting p_T spectrum has a sharp edge near the threshold of the requirement on the leading jet p_T.

9.2.3 Uncertainty of the lepton background yield

The systematic uncertainty mainly arises due to the rejection of the contamination of interacting-hadron tracks.

In the electron channel, the uncertainty is evaluated by comparing with the probability $\mathcal{P}_{dis}^{e}$ derived by changing the invariant mass window by 2.5 GeV that give two times larger or smaller contamination of QCD multi-jet events and W+jets processes. Figure 9.13 shows $\mathcal{P}_{dis}^{e}$ with three different invariant-mass selection requirements as a function of the probe electron track p_T, showing no significant difference and an agreement within the statistical uncertainty of 4%. Therefore, an overall uncertainty of ± 4% is assigned on the electron background yield.

In the muon channel, the uncertainty is evaluated by varying the cut value on E_T^{cone40}/p_T by ± 0.4. Figure 9.14 shows $\mathcal{P}_{dis}^{\mu}$ with different selection requirements of E_T^{cone40}/p_T as a function of p_T. The purity of muons in the probe tracks with higher p_T, which is of particular importance in this search, is quite high and the systematic effect in the high-p_T region of the estimated muon track spectrum is small.
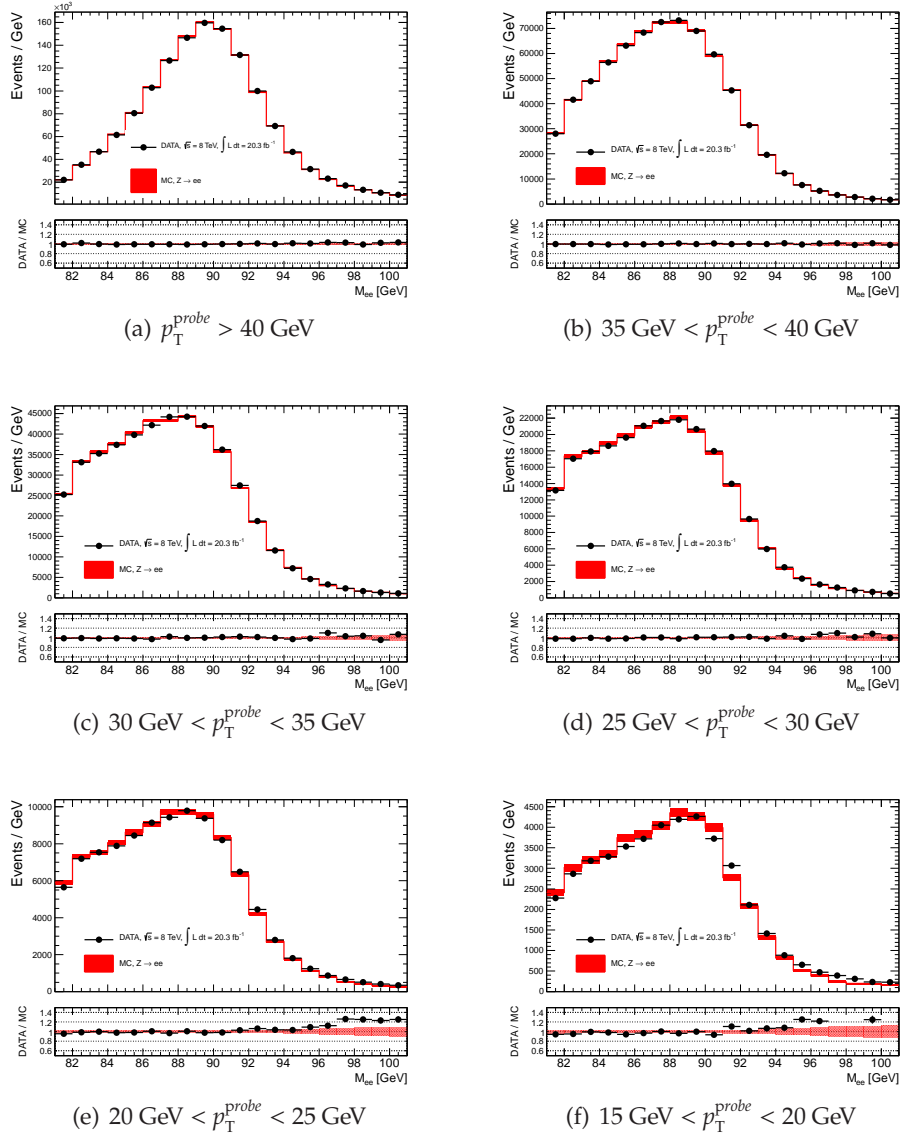
Figure 9.8: The m_{ee} distributions for various p_T-ranges of the probe electron. The MC events are normalized to the observed number of events.

(a) $p_T^{probe} > 40$ GeV

(b) 35 GeV $< p_T^{probe} < 40$ GeV

(c) 30 GeV $< p_T^{probe} < 35$ GeV

(d) 25 GeV $< p_T^{probe} < 30$ GeV

(e) 20 GeV $< p_T^{probe} < 25$ GeV

(f) 15 GeV $< p_T^{probe} < 20$ GeV
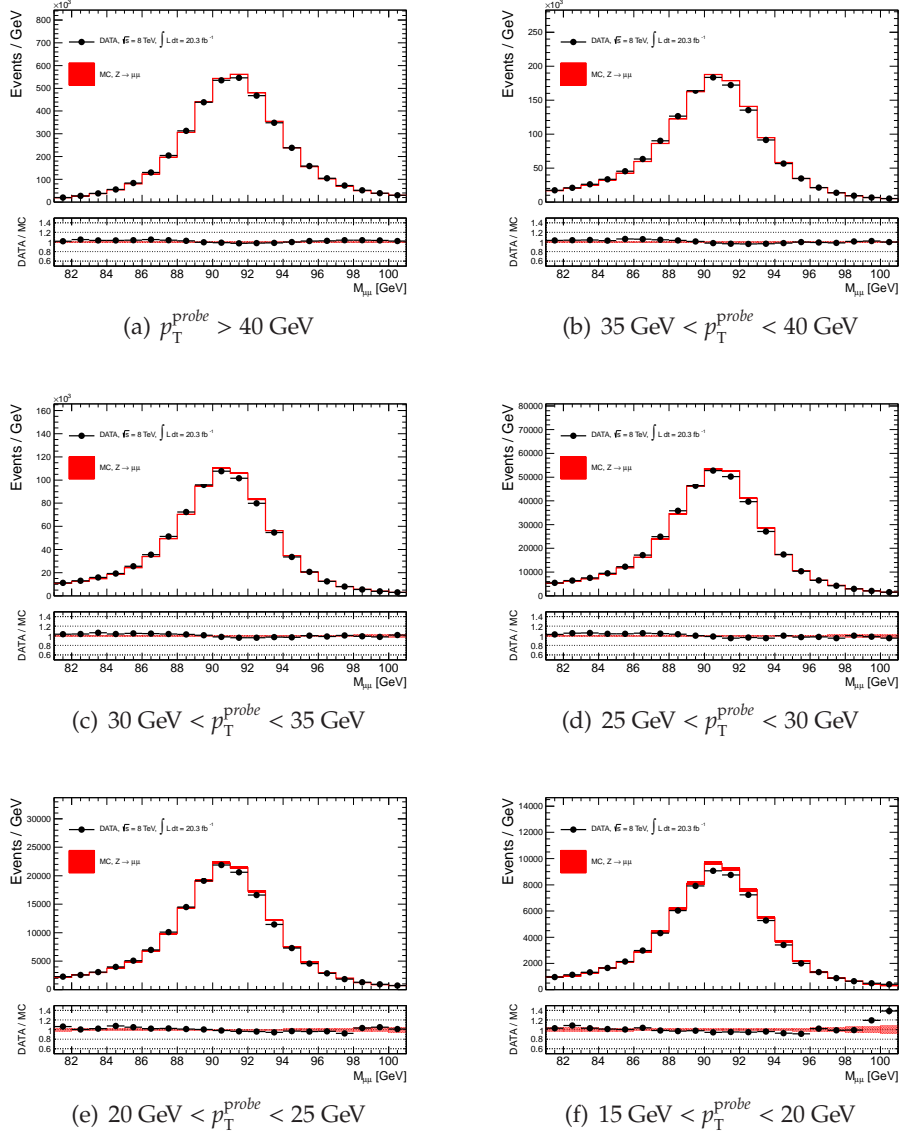
Figure 9.9: The $m_{\mu\mu}$ distributions for various p_T-ranges of the probe muon. The MC events are normalized to the observed number of events.
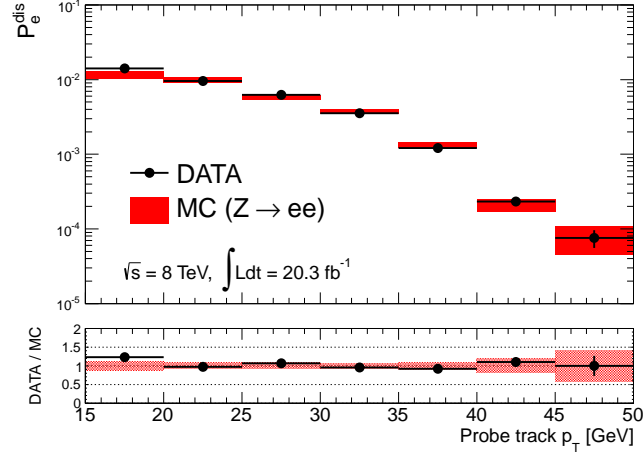
Figure 9.10: Probability of failing identification and satisfying disappearing-track selection criteria for electrons. The results derived by the tag-and-probe method based on the data and $Z \rightarrow ee$ MC events are indicated by black and red circles, respectively.
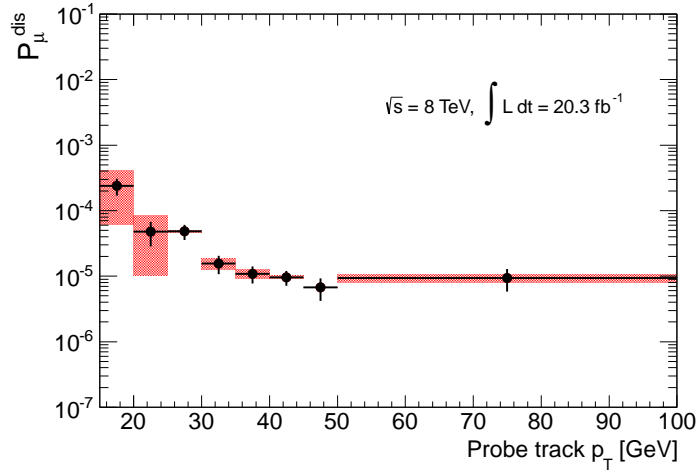
Figure 9.11: Probability of failing identification and satisfying disappearing-track selection criteria for muons. The shaded red band shows the systematic uncertainty related to the rejection of the interacting-hadron track contamination.
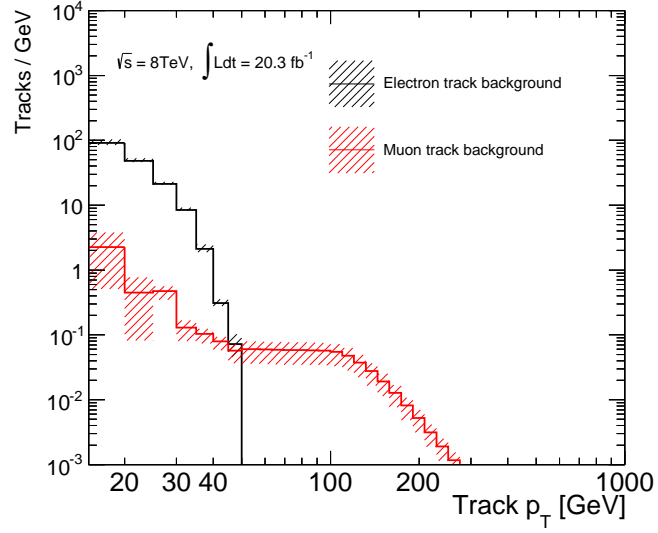
Figure 9.12: Estimated p_T distribution of residual lepton background tracks. The systematic uncertainties are incorporated in the p_T spectrum and indicated by hatched error bands.
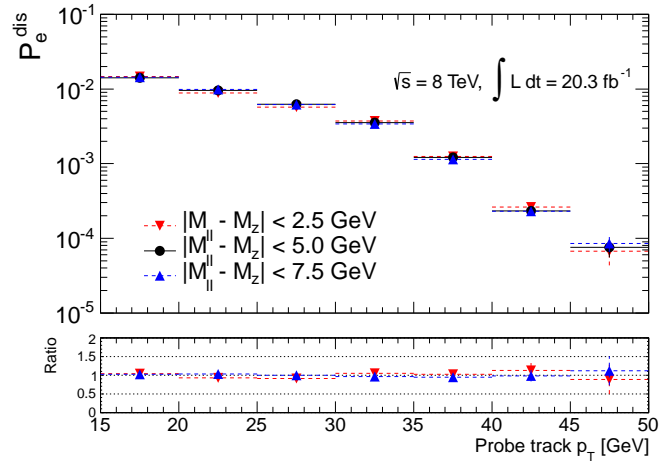
Figure 9.13: Probability $\mathcal{P}^e_{\mathrm{dis}}$ derived by three different invariant-mass selection requirements.
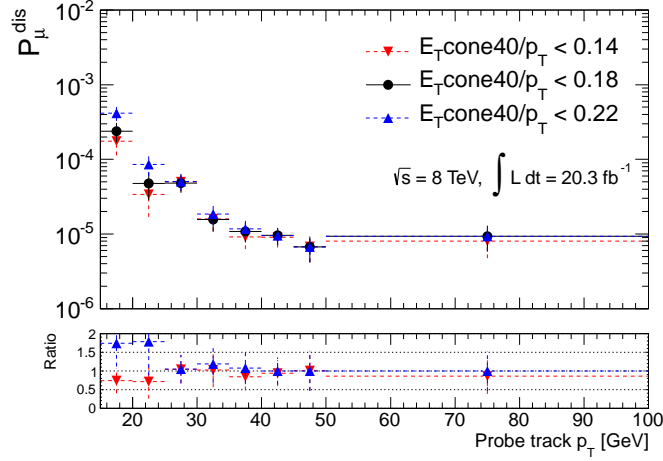
Figure 9.14: Probability $\mathcal{P}^{\mu}_{\mathrm{dis}}$ derived by varying the cut value on $E^{\mathrm{cone40}}_{\mathrm{T}}/p_{\mathrm{T}}$ by $\pm$ 0.4.

9.3 Tracks with mismeasured p_{T}

The background contribution to disappearing-track candidates with $p_{\mathrm{T}} > 100$ GeV originates primarily from p_{T}-mismeasured tracks. A high density of silicon hits, hadronic interactions and scattering can lead to combinations of wrong space-points in the procedure of track-seed finding or outward-extension of trajectories, resulting in anomalously high values of p_{T} especially for short-length tracks. The application of Re-tracking helps to increase the acceptance for the decaying chargino tracks at low radius but also leads to a non-negligible contribution of p_{T}-mismeasured tracks in the signal search sample. Figure 9.15 shows a MC event display of a p_{T}-mismeasured track formed by a hadronic interaction in the SCT detector. The p_{T}-mismeasured tracks could have anomalously high values of p_{T} and could mimic signal tracks, therefore, the understanding of their properties and a fair estimation of their background contribution based on the data are of particular importance.

Figure 9.16 shows the d_0 distributions for p_{T}-mismeasured tracks obtained by QCD multi-jet MC events and decaying chargino tracks. The p_{T}-mismeasured tracks in QCD multi-jet events most likely originate from a wrong combination of space-points, therefore their d_0 is broadly distributed. On the other hand, the high-p_{T} chargino tracks have a good pointing resolution and cluster around zero in the d_0 distribution. Therefore, by applying the tight requirement on the impact parameter for the candidate tracks as described in Sec. 8.2.5, the contribution of p_{T}-mismeasured tracks can be significantly suppressed. Furthermore, p_{T} and d_0 of p_{T}-mismeasured tracks are (most likely) randomly given since they arise from randomly combined space-points. On this assumption, the sample of tracks having large d_0 is used as a pure control sample of p_{T}-mismeasured tracks.
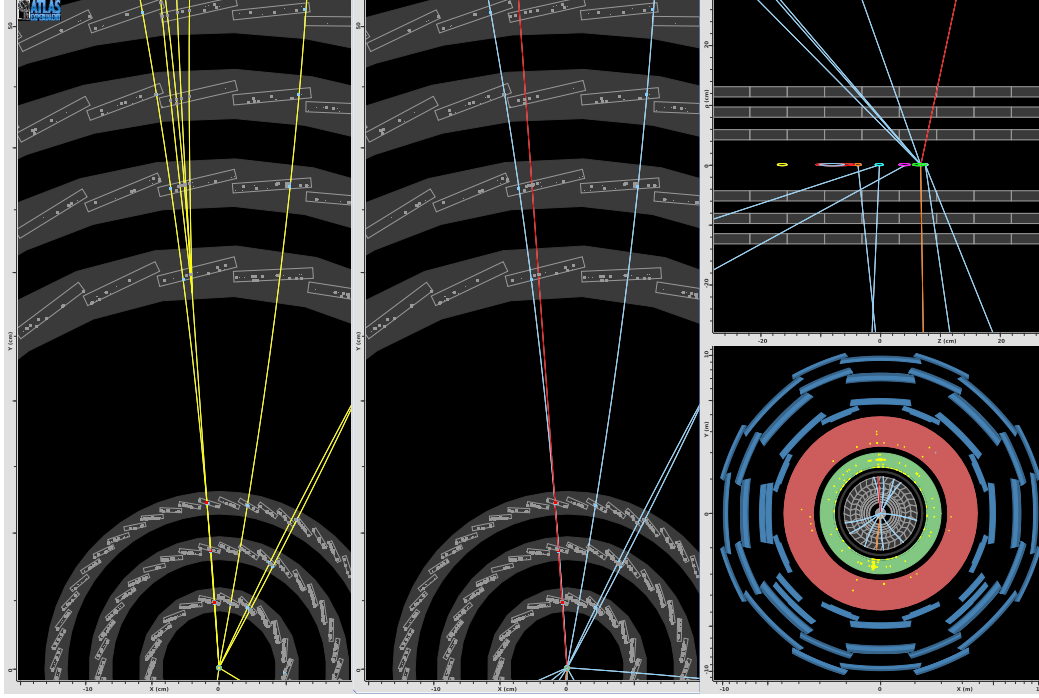
Figure 9.15: Event display of a MC event containing a p_T-mismeasured track. The figure on the left shows true charged tracks with $p_T > 1$ GeV. The corresponding reconstructed track is indicated by a red solid line in the middle figure.

9.3.1 Control data sample of p_T-mismeasured tracks

The pure control data sample of p_T-mismeasured tracks is obtained by inverting the requirement on the impact parameters as follows:

1. Apply the same kinematic selection requirements as for the signal search sample.

2. Apply an inverted cut on the impact parameter: 1.0 mm $< |d_0| < 10.0$ mm.

3. Apply the disappearing track selection criteria except for the d_0 requirement.

4. Require that the track must not have an associated calorimeter activity: $E_T^{cone40} < 7.5$ GeV and $\sum_{\Delta R < 0.4} E_T^{clus}/p_T^{track} < 0.4$. This removes the contamination of interacting-hadron tracks.

One important point is to ensure that the p_T shape of p_T-mismeasured tracks does not alter by the requirement on d_0. Figure 9.17 shows the p_T distribution of p_T-mismeasured tracks for small (close to the region $|d_0| < 0.1$ mm used in the candidate track selection) and large d_0 values in the data with the kinematic
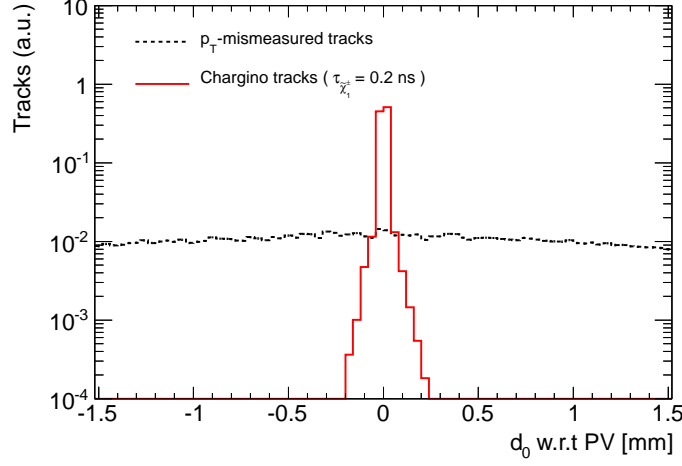
Figure 9.16: The d_0 distribution for p_T-mismeasured (black) and decaying chargino (red) tracks. The sample of p_T-mismeasured tracks is obtained in the QCD multi-jet MC events by requiring that the reconstructed p_T must have a significantly large value compared to that of the corresponding true charged particle.
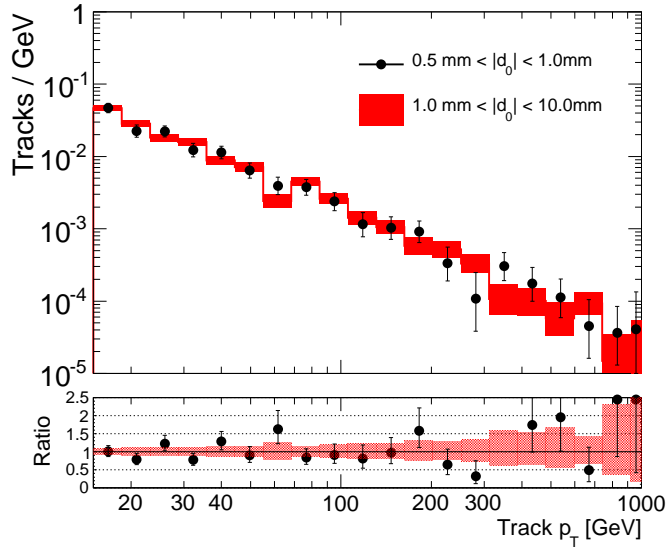
Figure 9.17: The p_T distribution of p_T-mismeasured tracks in the data with the requirements $0.5 < |d_0| < 1.0$ mm and $1.0 < |d_0| < 10$ mm. The same kinematic selection requirements as for the signal search sample are applied.

and disappearing-track selection requirements, showing no impact-parameter-cut dependence on the p_T shape.

The p_T shape of the p_T-mismeasured background tracks is then modeled by fitting an ansatz functional form

$$f(x) = x^{-b_0},\tag{9.7}$$

to the p_T spectrum observed in the p_T-mismeasured track control sample, where $x \equiv p_T^{\text{track}}$ and b_0 are fit parameters. Figure 9.18 shows the track-p_T distribution and the p_T shape derived by the maximum likelihood fit. The resulting parameter is

$$b_0 = 1.78 \pm 0.05.\tag{9.8}$$

The data is well-described by this functional form; χ^2 per degree of freedom of 55.2/60 is calculated from the difference between the data and the best-fit form.
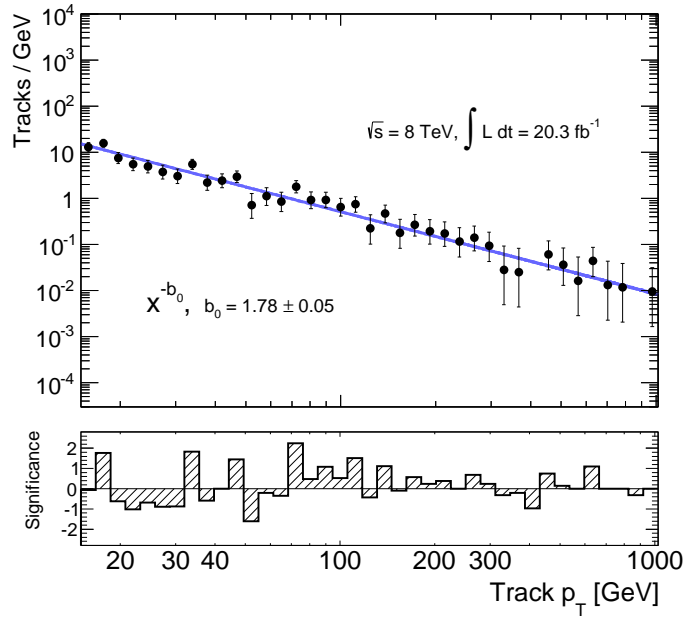
Figure 9.18: The p_T distribution of p_T-mismeasured tracks in the control sample. The data and the fitted shape are shown by solid circles and a line, respectively. The significance of the data-model difference on a bin-by-bin basis is also shown at the bottom of the figure.

9.3.2   Further check on the impact-parameter dependence

The p_T-mismeasured tracks remaining in the signal search sample have values of $|d_0| < 0.1$ mm and potentially associated to hits arising from charged particles

produced from hard-collision vertices. Therefore, validating the principle of "no impact-parameter-cut dependence" using tracks $|d_0| < 0.1$ mm is important to justify the background estimation technique. The validation is then performed by checking p_T distributions of p_T-mismeasured tracks in a QCD multi-jet enriched sample obtained by applying the following requirements:

- Dataset: QCD multi-jet enriched sample collected by single-jet triggers.

- Jet quality requirements.

- At least one reconstructed primary vertex with a minimum of five tracks with $p_T > 0.4$ GeV.

- No identified electrons and muons with $p_T > 10$ GeV.

- At least one jet with $p_T > 90$ GeV.

- $E_T^{\mathrm{miss}} < 90$ GeV, which is orthogonal to the event selection in the signal search sample.

- The high-p_T isolated track selection with the requirements of $p_T^{\mathrm{track}} > 50$ GeV and $|d_0| < 0.1$ mm.

The contamination from interacting-hadron and lepton tracks is expected to be very small in this sample.

Figure 9.19 shows the resulting track-p_T distribution in comparison with one obtained by requiring 1 mm $< |d_0| < 10$ mm. The distributions are also fitted with the functional form given in Eq. 9.7; the fitted parameters are summarized in Table 9.1. Two p_T shapes are consistent within the statical uncertainties and no impact-parameter-cut dependence is observed.

Parameter	$|d_0| < 0.1$ mm	1 mm $< |d_0| < 10$ mm
b_0	1.62 ± 0.07	1.69 ± 0.01

Table 9.1: Fitted b_0 parameters derived in the QCD multi-jet enriched sample.

9.3.3 Systematic uncertainty on the track-p_T shape

Figure 9.20 shows the d_0 distribution of the p_T-mismeasured tracks in $W \to \ell\nu$ MC events that dominate in the signal search sample. A large fraction of these p_T-mismeasured tracks have $d_0 \sim 0$, indicating that p_T of these tracks is wrongly determined most likely when extending their tracks outwards and combining incorrect space-points, while the control sample is expected to be dominated by tracks whose seeds are wrongly formed. Therefore, in order to take account of possible biases induced by the d_0 requirement, an additional uncertainty is assigned by taking the difference between the b_0 parameter given in Eq. 9.8 and
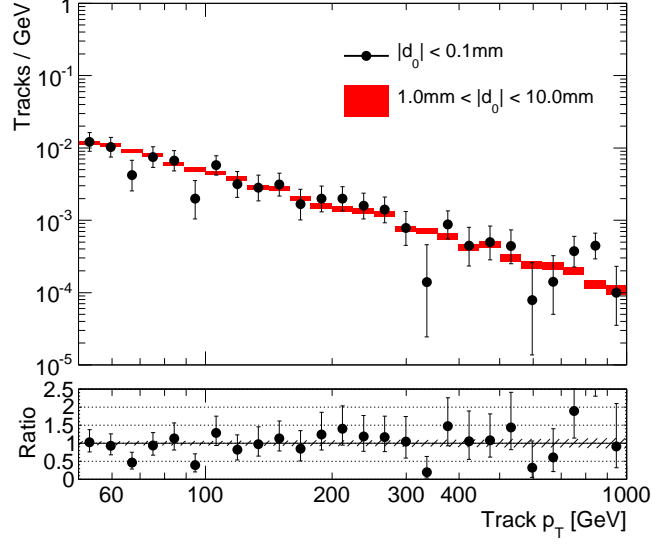
Figure 9.19: The p_T distributions of p_T-mismeasured tracks with $|d_0| < 0.1$ mm and 1 mm $< |d_0| < 10$ mm in the QCD multi-jet enriched sample.

the one derived by $W \rightarrow \tau\nu$ MC events. Figure 9.21 shows the p_T distributions of p_T-mismeasured tracks in the control sample and $W \rightarrow \tau\nu$ MC background events. The b_0 parameter for $W \rightarrow \tau\nu$ MC events is found to be 1.82 ± 0.07, showing that the track-p_T shapes of these two samples are consistent with each other within the statistical uncertainties. The difference of b_0 parameter between the control sample and $W \rightarrow \tau\nu$ MC events is assigned as a systematic uncertainty.
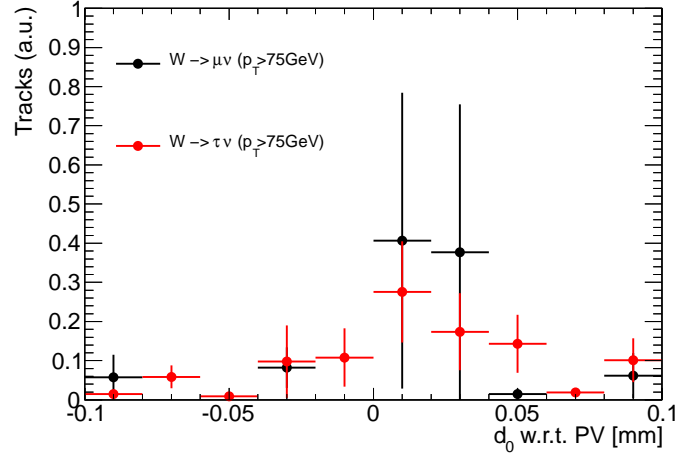
Figure 9.20: The d_0 distribution of p_T-mismeasured tracks that pass the disappearing track selection in $W \rightarrow \ell\nu$ MC events. The predictions for $W \rightarrow \mu\nu$ and $W \rightarrow \tau\nu$ background events are shown by black and red solid circles, respectively.
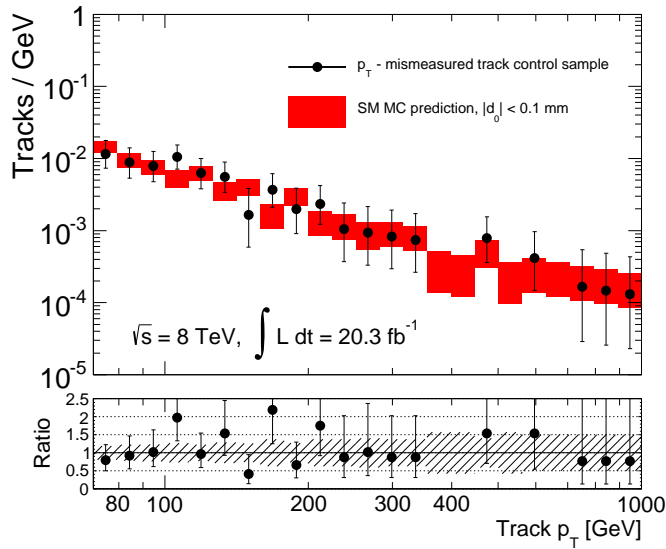
Figure 9.21: The p_T distribution of p_T-mismeasured tracks in the control sample and the SM MC background prediction ($W \rightarrow \tau\nu$ MC events). The error bars and band indicate the statistical uncertainties of each sample.

Chapter 10

Systematic Uncertainties

This section describes the uncertainties of signal normalization and the background track shapes to be incorporated in the fit and resulting signal yield.

10.1 Uncertainty on the signal events

The following sources of systematic uncertainties on the signal normalization have been considered:

- Uncertainties on the theoretical cross-section.

- Uncertainties on the initial and final state radiation (ISR/FSR).

- Uncertainties on the jet energy scale and resolution (JES/JER).

- Uncertainties on the trigger efficiency.

- Uncertainties on the pile-up modeling.

- Uncertainties on the track reconstruction efficiency and p_T resolution.

- Uncertainty on the integrated luminosity.

Theoretical uncertainties on the signal cross-section are evaluated by computing the changes in the cross-section when the renormalization and factorization scales, the choice of PDFs, and the strong coupling constant (α_s) are varied. Varying the scales with factors of 0.5 and 2, the uncertainties on the scales and α_s are estimated. The uncertainty arising from PDFs is evaluated by using the error sets of the PDF set as described in Sec. 4.2.1. Finally, by taking the maximum difference between 68% CL upper and lower limits on the cross-sections calculated using `CTEQ6.6` and `MSTW2008 NLO` PDFs.

High–p_T jets originating from ISR and FSR alter the signal acceptance. The uncertainties on ISR and FSR are estimated by varying generator tunes in the simulation as well as by generator-level studies carried out on samples produced

with an additional jet in the matrix-element method using `Madgraph5` [103] pro-
gram and `PYTHIA6` program. By adopting the PDF tunes that provide less and
more radiations and taking the maximum deviation from the nominal tune, the
uncertainty due to jet radiation is evaluated. The uncertainty arising from the
matching of matrix elements with parton showers is evaluated by doubling and
halving the default value of the matching parameter [104]. The resulting changes
are combined in quadrature and yield an uncertainty of 10–17% depending on
$m_{\tilde{\chi}_1^\pm}$.

The uncertainty on the JES and JER results in a variation of the signal selec-
tion efficiency, but does not directly affect the p_T distribution of chargino tracks
remaining after the selection cuts. In this analysis, the uncertainty of the overall
normalization arising from JES and JER is assessed according to Ref. [96] . The
uncertainty on E_T^{miss} due to JES is also taken into account in a coherent way. The
effect of JER are found to be much smaller than 1% and neglected.

An uncertainty of 4.5% on the trigger efficiency is assigned by taking the
difference between data and MC simulation in a W+jet sample in which W decays
into μ plus ν_μ, as described in Sec. 8.1.1.

The uncertainty originating from the pile-up modeling in the simulation is
evaluated by weighting simulated samples so that the average number of pile-up
interactions is increased or decreased by 10%, which yields a 0.5% uncertainty
on the signal efficiency. The impact on the selection efficiency, arising from the
increase of the noise occupancy in the TRT detector, is found to be negligible.

The modeling of the ID material alters the track reconstruction efficiency and
affects the signal selection efficiency. An uncertainty of 2% on the tracking effi-
ciency due to the material description in the MC simulation, especially for tracks
in the region of $|\eta| < 1.9$, is quoted as given in Ref. [100]. No evidence of the
difference of the track-p_T resolution between data and MC events is also found by
checking the interacting-hadron tracks especially having $N_{SCT} = 2$; the impact of
the p_T resolution on the broad distribution of high-p_T chargino tracks is negligibly
small.

The uncertainty on the integrated luminosity is estimated to be ±2.8%, as given
in Ref. [66,67].

Contributions of each systematic uncertainty in the signal expectations are
summarized in Table 10.1.

10.2 Uncertainty on the background events

Systematic uncertainties on the background p_T shapes and normalizations arising
from statistical uncertainties of the control data samples and uncertainties on the
lepton identification efficiencies are considered in deriving the results[1]. In order
to incorporate these uncertainties, the shape parameters are adopted as nuisance

---

[1]Details on each systematic uncertainty is described in Sec. 9

Source	Chargino mass (GeV)							
	80.5	98.9	124.5	149.8	201.0	225.6	250.0	274.4
(Theoretical uncertainty)								
Cross-section	±8.2	±7.6	±7.1	±6.8	±6.4	±6.4	±6.6	±6.5
(Uncertainties on the acceptance)								
ISR/FSR	±12.6	±13.2	±15.0	±14.5	±14.5	±15.0	±16.0	±16.2
JES/JER	$^{+3.6}_{-5.5}$	$^{+4.9}_{-3.9}$	$^{+5.8}_{-3.7}$	$^{+3.2}_{-3.9}$	$^{+3.8}_{-3.9}$	$^{+3.0}_{-2.3}$	$^{+2.9}_{-4.7}$	$^{+3.8}_{-1.3}$
Trigger efficiency	±4.5 %							
Pile-up modeling	±0.5 %							
Track reconstruction efficiency	±2.0 %							
Luminosity	±2.8 %							
Sub-total	±14.9	±15.2	±17.1	±16.1	±16.1	±16.3	±17.6	±17.6

Table 10.1: Summary of systematic uncertainties [%] in the expectation of signal events.

Source	Chargino mass (GeV)				
	300.0	351.1	399.1	449.5	499.6
(Theoretical uncertainty)					
Cross-section	±6.8	±7.0	±7.6	±8.0	±8.2
(Uncertainties on the acceptance)					
ISR/FSR	±16.4	±16.8	±17.9	±18.1	±17.8
JES/JER	$^{+2.3}_{-6.0}$	$^{+2.2}_{-3.3}$	$^{+5.7}_{-1.5}$	$^{+2.1}_{-2.1}$	$^{+3.6}_{-2.0}$
Trigger efficiency	±4.5 %				
Pile-up modeling	±0.5 %				
Track reconstruction efficiency	±2.0 %				
Luminosity	±2.8 %				
Sub-total	±18.4	±18.0	±19.6	±19.1	±19.0

Table 10.2: Summary of systematic uncertainties [%] in the expectation of signal events.

parameters in the fit and the correlations between them are taken into account. For the p_T shape of p_T-mismeasured tracks, in order to take account of possible biases induced by the d_0 requirement, an additional uncertainty is assigned by taking the difference of the fit result for p_T-mismeasured track control samples and SM background events as discussed in 9.3.3. Details of the statistical analysis procedure are given in the next section.

Chapter 11

Extraction of Signal Yield

The chargino tracks have high p_T, and all background tracks show distinctive p_T spectra. The signal hypothesis with given values of $m_{\tilde{\chi}_1^\pm}$ and $\tau_{\tilde{\chi}_1^\pm}$ is therefore tested based on an extended maximum likelihood fit to the p_T spectrum of the disappearing-track candidates. The likelihood function for the track p_T consists of one probability density function for the signal and four for the different background components. If multiple disappearing-track candidates appear in an event, the candidate with the highest p_T is used to define the likelihood function. In the fit, the yields of the signal, interacting-hadron, and p_T-mismeasured tracks are left free. The yields of electron and muon background tracks are constrained to their estimated values within the systematic uncertainties. The effects of systematic uncertainties on the yields and the parameters describing the p_T shapes of the background tracks are also incorporated into the likelihood function. The following sections describe the details of the fit procedure.

11.1   Unbinned extended maximum likelihood fit

In order to evaluate how well the observed data agree with a given signal model, a statistical test is performed based on an extended maximum likelihood. The likelihood function for the track p_T ($\mathcal{L}$) in a sample of observed events (n_{obs}) is defined as

$$
\begin{aligned}
\mathcal{L}(n_{\mathrm{s}}, n_{\mathrm{h}}, n_{\mathrm{e}}, n_{\mu}, n_{\mathrm{m}}) \quad &\equiv \quad \mathcal{L}_{\mathrm{shape}}(p_T; n_{\mathrm{s}}, n_{\mathrm{h}}, n_{\mathrm{e}}, n_{\mu}, n_{\mathrm{m}}, \vec{\theta}_{\mathrm{h}}, \vec{\theta}_{\mathrm{m}}) \\
&\quad \times \quad \mathcal{L}_{\mathrm{sys}}(\alpha_{\mathrm{s}}, \alpha_{\mathrm{e}}, \alpha_{\mu}, \vec{\theta}_{\mathrm{h}}, \vec{\theta}_{\mathrm{m}}), &(11.1) \\
n_{\mathrm{s}} \quad &\equiv \quad \mu(1 + \alpha_{\mathrm{s}}) n_{\mathrm{s}}^{\mathrm{exp}} = \mu L \sigma_s \epsilon_s (1 + \alpha_{\mathrm{s}}), &(11.2) \\
n_{\mathrm{e}} \quad &\equiv \quad (1 + \alpha_{\mathrm{e}}) n_{\mathrm{e}}^{\mathrm{exp}}, &(11.3) \\
n_{\mu} \quad &\equiv \quad (1 + \alpha_{\mu}) n_{\mu}^{\mathrm{exp}}, &(11.4)
\end{aligned}
$$

where

$n_s^{(\text{exp})}$: the (expected) number of signal events for a given model,

$n_{e,\mu}^{(\text{exp})}$: the (expected) number of electron and muon track events,

$n_{h,m}$: the number of interacting-hadron and p_T-mismeasured track events,

$\alpha_{s,e,\mu}$: the nuisance parameter representing the overall normalization of the signal, electron, and muon track yields,

$\vec{\theta}_h$: the nuisance parameters representing the p_T spectrum of the interacting-hadron tracks ($\vec{a} = (a_0, a_1, a_2, a_3)$),

$\vec{\theta}_m$: the nuisance parameter representing the p_T spectrum of the p_T-mismeasured tracks ($\vec{b} = (b_0)$),

μ : the signal strength,

σ_s : the signal cross-section,

ϵ_s : the signal selection efficiency,

L : the integrated luminosity (20.3fb^{-1}).

The formulations of $\mathcal{L}_{\text{shape}}$ and $\mathcal{L}_{\text{sys}}$ are given as

$$\mathcal{L}_{\text{shape}} = \prod^{n_{\text{obs}}} \frac{n_s \mathcal{F}_s(p_T; \alpha_s) + n_h \mathcal{F}_h(p_T; \vec{\theta}_h) + n_e \mathcal{F}_e(p_T; \alpha_e) + n_\mu \mathcal{F}_\mu(p_T; \alpha_\mu) + n_m \mathcal{F}_m(p_T; \vec{\theta}_m)}{n_s + n_h + n_e + n_\mu + n_m},$$
(11.5)

$$\mathcal{L}_{\text{sys}} = \mathcal{N}(\alpha_s; \Delta_s^2) \times \mathcal{N}(\alpha_e; \Delta_e^2) \times \mathcal{N}(\alpha_\mu; \Delta_\mu^2) \times \mathcal{M}(\vec{\theta}_h; C_h) \times \mathcal{M}(\vec{\theta}_m; C_m),$$
(11.6)

where $\mathcal{F}_s$, $\mathcal{F}_h$, $\mathcal{F}_e$, $\mathcal{F}_\mu$ and $\mathcal{F}_m$ are the probability density functions of signal, interacting-hadron, electron, muon, and p_T-mismeasured tracks. The functions of $\mathcal{N}$ and $\mathcal{M}$ represent the normal distribution and the multivariate normal distribution in which the variance $\Delta_{s(e,\mu)}^2$ represents the systematic uncertainty of the signal (electron and muon background) normalization that is summarized in Sec. 10, respectively. The resulting probability densities of the signal and background components on the track p_T are shown in Fig. 11.1. The selection efficiency and the expected number of events as a function of $\tau_{\tilde{\chi}_1^\pm}$ for various signal points are also shown in Fig. 11.2. The chargino p_T spectra for various values of lifetime and mass are shown in Fig. 11.3.

11.2 Validation of the signal extraction method

In order to validate the fit procedure and performance, an ensemble of pseudo-experiments of observing 3256 events with any compositions of signal and background events is prepared by using the model described in Eq. 11.1 with various

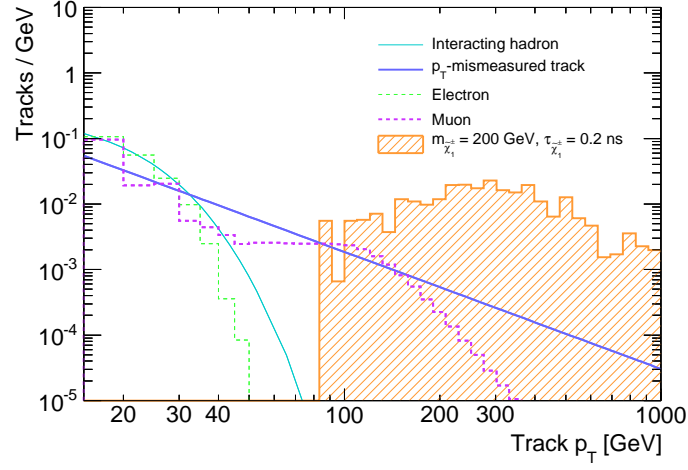Figure 11.1: Probability densities of the signal model with $m_{\tilde{\chi}_1^\pm} = 200$ GeV and $\tau_{\tilde{\chi}_1^\pm}$ = 0.2 ns and all background components on the track p_T.

(a) Efficiency (ϵ_s)
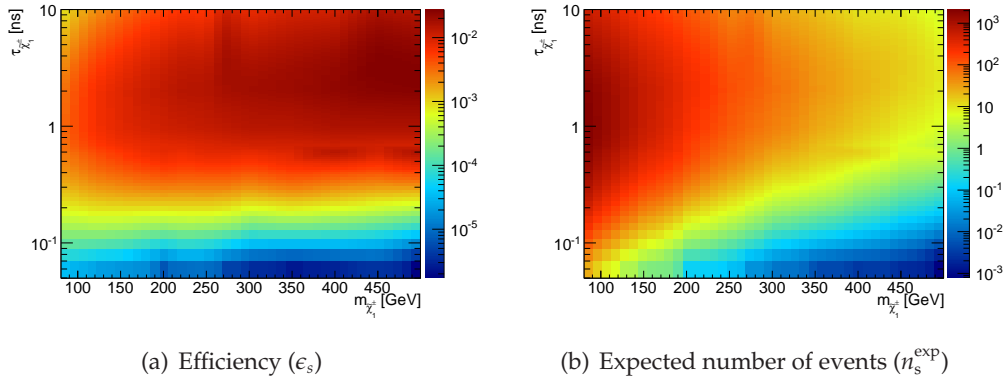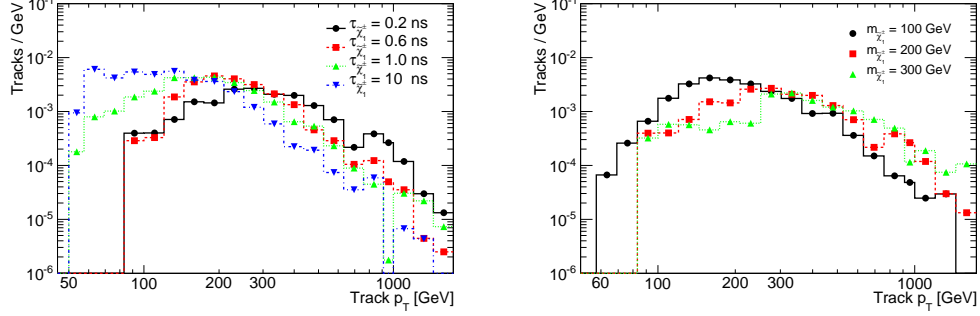
(b) Expected number of events ($n_s^{\exp}$)

Figure 11.2: Selection efficiency (a) and the expected number of signal events (b) as a function of the chargino lifetime and chargino mass.

(a) Chargino p_T spectra for $m_{\tilde{\chi}_1^\pm} = 200$ GeV and (b) Chargino p_T spectra for $\tau_{\tilde{\chi}_1^\pm} = 0.2$ ns and various lifetime values
ous masses

Figure 11.3: Chargino p_T spectra for various values of lifetime (a) and mass (b). The distributions are normalized to unity.

values of parameters. In this analysis, the yields of the electron and muon track backgrounds are estimated with finite systematic uncertainties. Therefore, the normalization of the electron and muon track backgrounds are fixed to their estimated values in this closure test, while the yields of the signal, interacting-hadron, and p_T-mismeasured tracks are left free. Figure 11.4 and 11.5 show fitted values of μ and the fraction of p_T-mismeasured tracks (f_m^{fitted}) as a function of f_m^{true} defined by

$$f_m^{\text{true}} \equiv \frac{n_m}{n_{\text{obs}} - (n_e^{(\text{exp})} + n_\mu^{(\text{exp})})}. \tag{11.7}$$

The signal strengths obtained by the pseudo-experiments with a signal sample ($m_{\tilde{\chi}_1^\pm} = 150$ GeV, $\tau_{\tilde{\chi}_1^\pm} = 0.2$ ns) peak around unity for any values of f_m^{true} in Fig. 11.5 (b). The fitted value f_m^{fitted} is determined within an uncertainty $\sigma(f_m) \sim 0.03$ as shown in Fig 11.5 (c). In the case of no signal injection, the signal strengths peak around zero for any values of f_m^{true} as shown in Fig. 11.4 (b). The fitted value f_m^{fitted} is determined within an uncertainty $\sigma(f_m) \sim 0.03$ as shown in Fig. 11.4 (c), which is consistent with the error expected from the statistical uncertainty. These results indicate that the fit procedure works as expected, and it can correctly extract the yields of the signal, interacting-hadron, and p_T-mismeasured tracks.

11.3 Null-hypothesis testing in the high-p_T region

The high-p_T signal region provides significant signal-to-background ratios for any signal models, therefore, the agreement between the observation and the prediction on the null hypothesis in the high-p_T region is assessed with p-values in counting experiments; higher-p_T regions give sensitivities on decaying charged particles with shorter lifetimes because large boost factors are required to fulfill the track selection requirements for such signals. Table 11.1 summarizes the
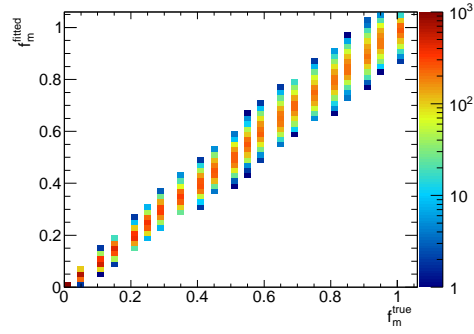
(a) f_m^{true} vs f_m^{fitted}
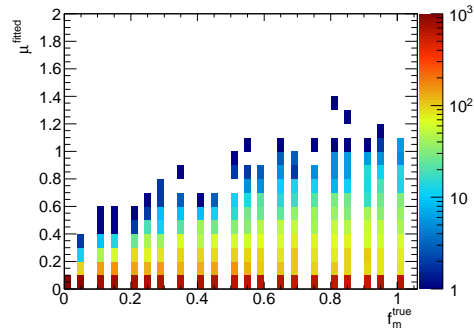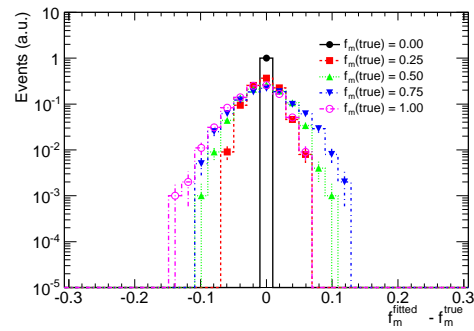
(b) f_m^{true} vs μ

(c) f_m^{true} - f_m^{fitted}

Figure 11.4: The f_m^{fitted} (a) and μ (b) as a function of f_m^{true} derived by each pseudo-experiment with the only backgrounds. The pull distributions, f_m^{true} - f_m^{fitted}, are also shown.

(a) f_m^{true} vs f_m^{fitted}

(b) f_m^{true} vs μ

(c) f_m^{true} - f_m^{fitted}

Figure 11.5: The f_m^{fitted} (a) and μ (b) as a function of f_m^{true} derived by each pseudo-experiment with a signal sample. The pull distributions, f_m^{true} - f_m^{fitted}, are also shown.
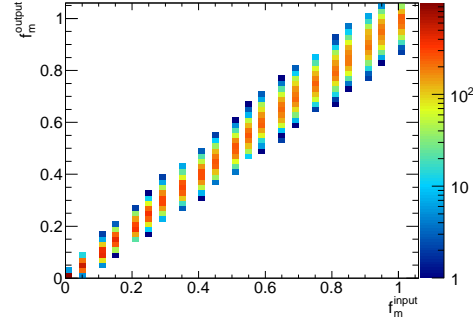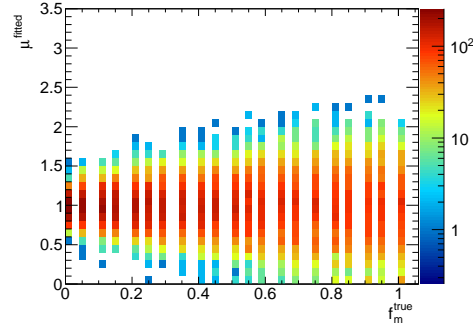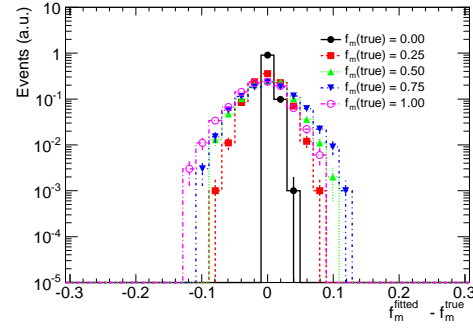
observed and expected numbers of tracks with $p_T > p_T^{thr}$ for four values of p_T^{thr}. The probability (p_0 value) that a background-only experiment is more signal-like than the observation and the model-independent upper limit on the visible cross-section ($\sigma_{vis}^{95\%}$) at 95% CL are also given in the table. Details on the limit setting are summarized in Appendix A. The expected numbers of background tracks for each region are derived by extrapolating the result of the background-only fit in the p_T region below 75 GeV. No significant excess is observed.

	$p_T^{track} > 75$ GeV	> 100 GeV	> 150 GeV	> 200 GeV
Observed events	59	36	19	13
Expected events	48.5 ± 12.3	37.1 ± 9.4	24.6 ± 6.3	18.0 ± 4.6
p_0 value	0.17	0.41	0.46	0.44
Observed $\sigma_{vis}^{95\%}$ [fb]	1.76	1.02	0.62	0.44
Expected $\sigma_{vis}^{95\%}$ [fb]	$1.42^{+0.50}_{-0.39}$	$1.05^{+0.37}_{-0.28}$	$0.67^{+0.27}_{-0.19}$	$0.56^{+0.23}_{-0.16}$

Table 11.1: Numbers of observed and expected background events as well as the probability that a background-only experiment is more signal-like than observed and the model-independent upper limit on the visible cross-section $\sigma_{vis}^{95\%}$ at 95% CL.

11.4   Full p_T-range fit

Figure 11.6 shows the p_T distribution for disappearing-track candidates compared to the background model derived by the background-only fit in the full p_T range: the best-fit values for the yields of interacting-hadron, electron, muon, and p_T-mismeasured tracks are 2187 ± 71, 852 ± 35, 23 ± 8, and 212 ± 33, respectively. The predictions for three selected signal samples are also indicated in the figure.

Although the resulting background-only spectrum well describes the data, an excess with a corresponding significance of $\sim 2\sigma$ is seen at p_T around 90 GeV. Properties of the events in this region are fully addressed and discussed in Sec. 11.5, which shows no peculiarities or significant differences in event kinematics or track properties compared to candidates in nearby track-p_T regions.

Table 11.2 shows the values of fit parameters before and after the background-only fit. The parameter that describes the shape of the p_T-mismeasured tracks, which is most important to this analysis, is slightly shifted by the fit due to the existence of this excess. However, its value is close to the center value of p_T-mismeasured tracks for systematic samples described in Sec. 9.3.3.

The upper limit on the production cross-section for a given $m_{\tilde{\chi}_1^\pm}$ and $\tau_{\tilde{\chi}_1^\pm}$ or $\Delta m_{\tilde{\chi}_1}$ at 95% CL is then set along various values of signal strength. The expected limit is set by the median of the distribution of the 95% CL limits derived by the pseudo-experiments with the expected background and no signal. The systematic parameters are also varied according to their systematic uncertainties when performing the pseudo-experiments.
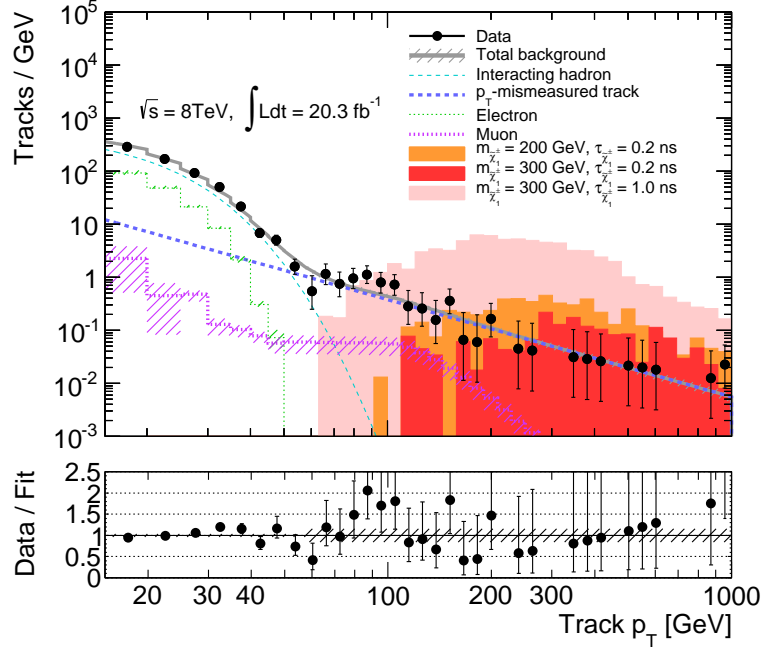
Figure 11.6: The p_T distribution of disappearing-track candidates. The solid circles show data and lines show each background track-p_T spectrum obtained by the background-only fit. The resulting uncertainties on the p_T spectrum for each background are indicated by the error bands. The signal expectations are also shown. The ratio of the data to the background track-p_T spectrum is shown at the bottom of the figure.

Parameter	Before fit	After fit
α_e	1.00 ± 0.04	0.96 ± 0.04
α_μ	1.00 ± 0.35	1.05 ± 0.37
$[\vec{\theta}_m]$		
b_0	1.78 ± 0.09	1.83 ± 0.08
$[\vec{\theta}_h]$		
a_0	7.45 ± 0.20	7.51 ± 0.20
a_1	75.9 ± 0.76	75.9 ± 0.78
a_2	1.16 ± 0.63	1.12 ± 0.67
a_3	9.40 ± 0.08	9.39 ± 0.08

Table 11.2: Values of fit parameters before and after the background-only fit.

11.5 Properties of the excess in the track-p_T spectrum

This section addresses the excess observed in Fig. 11.6. The followings could result in such an excess especially in the p_T region 75–120 GeV:

- Instrumental background.

- Underestimate of the muon background.

- Signature as decaying charged massive particles.

On the assumption that the excess is originating from charginos, p_T shapes of signal points with longer lifetimes and lower masses are preferred as shown in Fig. 11.3.

11.5.1 Instrumental background

Instrumental effects that could mimic disappearing tracks have been already taken into account in the background estimation. However, there might be missing detector issues that lead to this excess. Such background tracks might cluster in specific detector regions or appear in certain data-taking periods. Fig. 11.7 and 11.8 show the η–ϕ distribution of the candidate tracks and its projections. No spots are found especially in the p_T region where the excess is observed, and the events are randomly distributed during the period. No indication of the instrumental background effect is found.
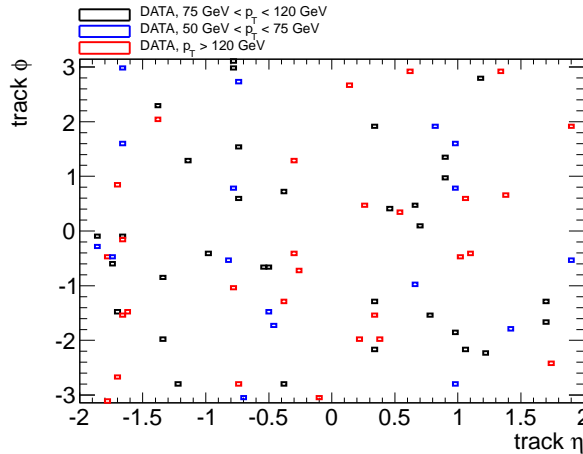

Figure 11.7: The η–ϕ distribution of the candidate tracks.
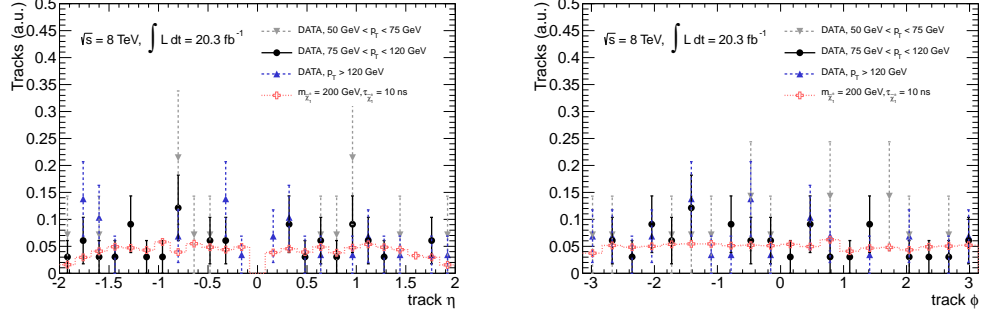
(a) The η distribution of the candidate tracks.   (b) The ϕ distribution of the candidate tracks.

Figure 11.8: The η and ϕ distribution of the candidate tracks.

11.5.2   Possibility of underestimating the muon background

Unidentified muons cannot be rejected by resolving object overlaps and they could have high p_T. If the excess is caused by the underestimate of $W \to \mu\nu$ background, the transverse mass reconstructed using the track momentum and E_T^{miss} should have a peak around 80 GeV. Fig. 11.9 shows the m_T distribution of the candidate tracks in the excess region. The m_T distributions of sideband track-p_T region and signal tracks are also shown. One event that has m_T of ~ 80 GeV is observed in this region, which is consistent with the estimated muon background yield. The excess is therefore not likely arising from the underestimate of $W \to \mu\nu$ background.

Figure 11.9: The m_T distribution of the candidate tracks with 75 GeV $< p_T <$ 120 GeV.

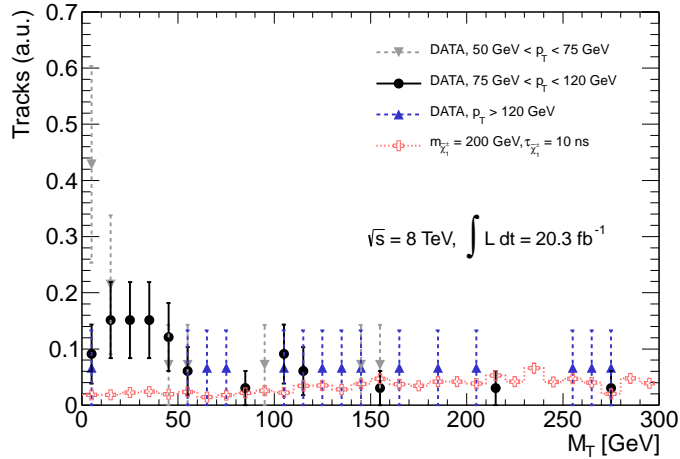### 11.5.3 Signature of decaying charged massive particles

Figure 11.10 shows the best-fit signal strengths in the $\tau_{\tilde{\chi}_1^\pm}$–$m_{\tilde{\chi}_1^\pm}$ plane. No signal model explaining the yield and shape of the excess simultaneously is found; the shape of the excess is compatible with a signal point with a lower mass (~ 80 GeV) and a longer mean lifetime (~ 10 ns) as shown in Fig. 11.11, although, its expected yield is too large with respect to the observation.
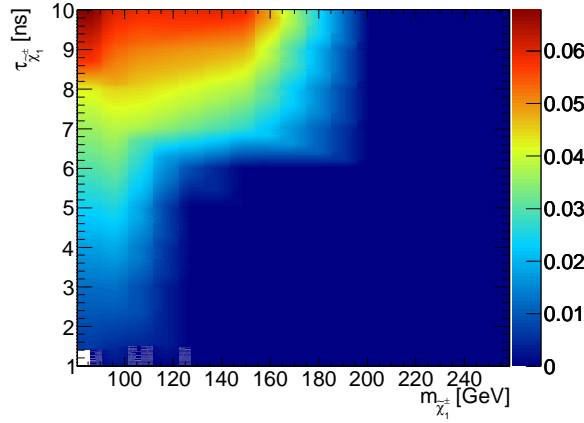
Figure 11.10: Best-fit signal strengths in the $\tau_{\tilde{\chi}_1^\pm}$–$m_{\tilde{\chi}_1^\pm}$ plane.
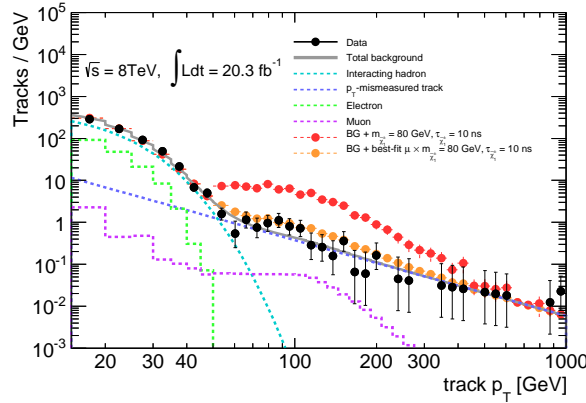
Figure 11.11: The p_T spectrum of the candidate tracks and the best-fit signal+background model with $m_{\tilde{\chi}_1^\pm} = 80$ GeV and $\tau_{\tilde{\chi}_1^\pm} = 10$ ns. The predicted p_T spectrum by setting the signal strength to unity is also shown.

Data-data comparisons could also provide meaningful information: p_T-mismeasured tracks dominate the background in the high-p_T region and the comparisons of kinematic distributions and track properties with those in sideband track-p_T regions,

where p_{T}-mismeasured tracks still dominate, could give any hints on the origin of the excess. Figure 11.12–11.14 show various kinematic distributions and track properties for the candidate tracks with p_{T} regions 50–75, 75–120 and >120 GeV. No significant differences are observed between each other. If the mean lifetime is relatively short ($<\sim 1$ ns), the signal events are likely to cluster at $N_{\mathrm{SCT}} = 2$. In the case of longer mean lifetimes ($>\sim 10$ ns), a sizable fraction of signal particles decay in the TRT detector and the number of TRT outliers could have a peak with an intermediate values as a result of a kinked-track signature.

In conclusion, the excess is consistent with neither any of AMSB signal points nor signatures of decaying charged massive particles, and most likely due to a statistical fluctuation of the background.

(a) Number of SCT hits

(b) Number of TRT outliers

(c) $E_{\mathrm{T}}^{\mathrm{cone40}}$

(d) $\sum_{\Delta R < 0.4} E_{\mathrm{T}}^{\mathrm{clus}}$
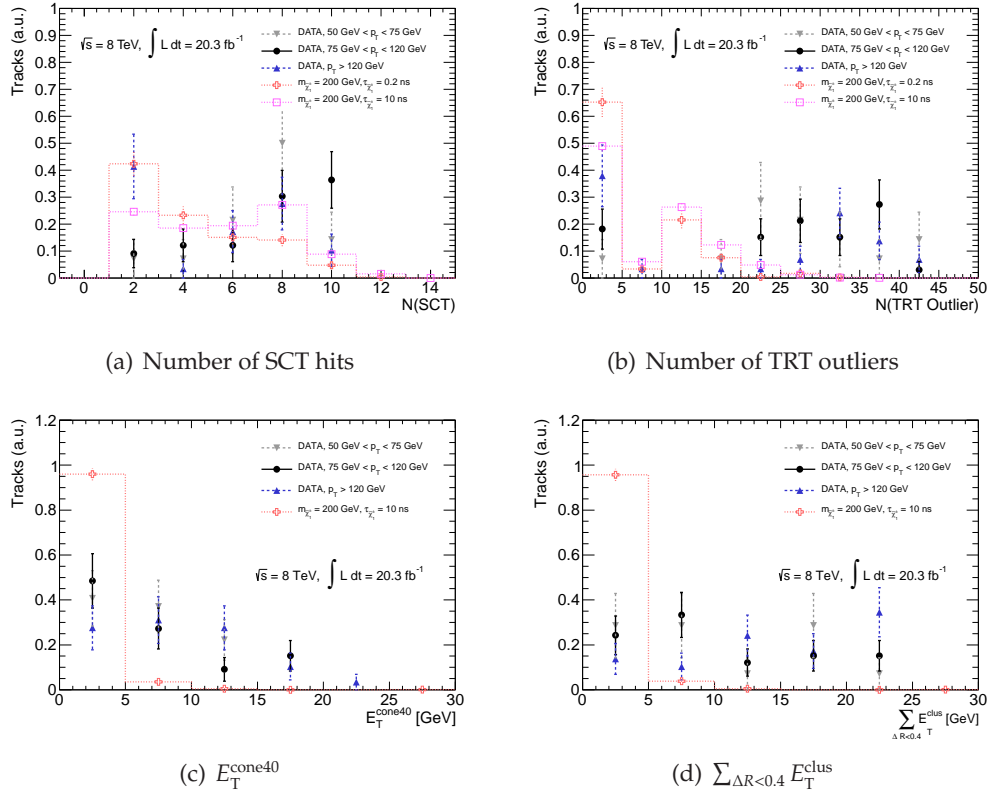
Figure 11.12: The N_{SCT}, number of TRT outliers and calorimeter isolation variables for the candidate tracks.

(a) d_0

(b) d_0 significance

(c) $z_0 \sin\theta$
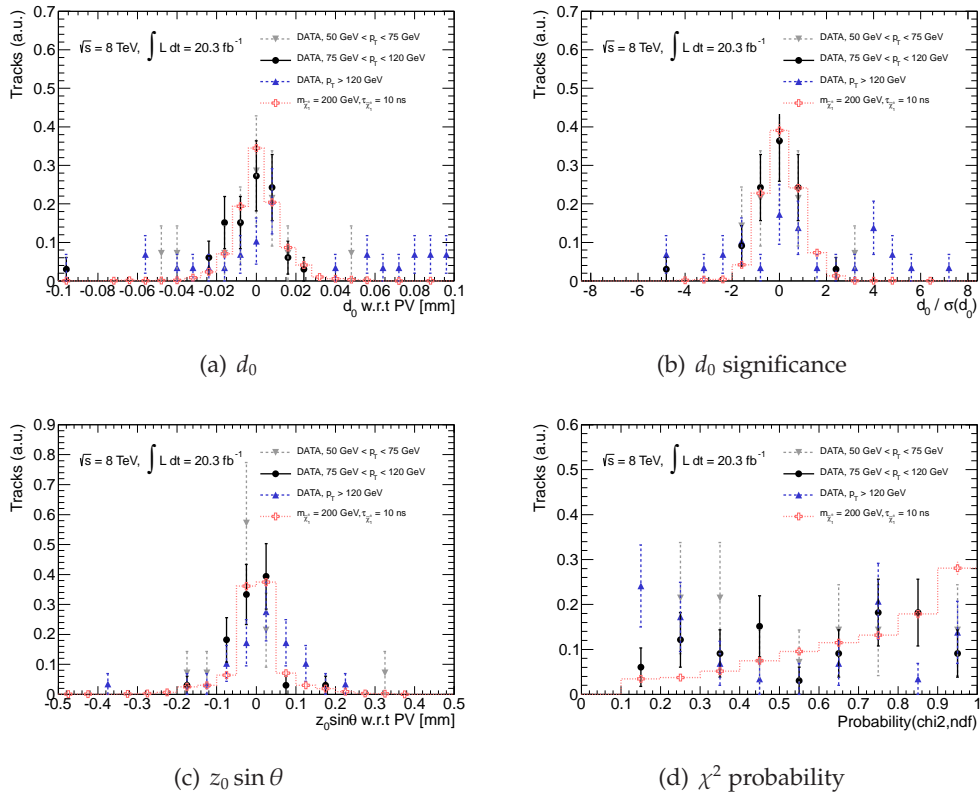
(d) χ^2 probability

Figure 11.13: Impact parameter variables and the χ^2 probability for the candidate tracks.

(a) Leading jet p_T

(b) E_T^{miss}

(c) $\Delta\phi_{min}^{jet-E_T^{miss}}$

(d) $\Delta\phi(track, E_T^{miss})$

(e) Number of jets with $p_T > 45$ GeV

(f) Number of reconstructed vertices

Figure 11.14: Kinematic distributions and reconstructed vertices for the candidate tracks.

Chapter 12

Interpretations and Discussion

12.1 Constraints on the AMSB model

In the absence of a signal, constraints are set on $m_{\tilde{\chi}_1^\pm}$ and $\tau_{\tilde{\chi}_1^\pm}$. The upper limit on the production cross-section for a given $m_{\tilde{\chi}_1^\pm}$ and $\tau_{\tilde{\chi}_1^\pm}$ at 95% CL is set at the point where the CL of the "signal+background" hypothesis, based on the profile likelihood ratio [105] and the *CLs* prescription [106], falls below 5% when scanning the CL along various values of signal strength. The constraint on the allowed $\tau_{\tilde{\chi}_1^\pm}$–$m_{\tilde{\chi}_1^\pm}$ parameter space is shown in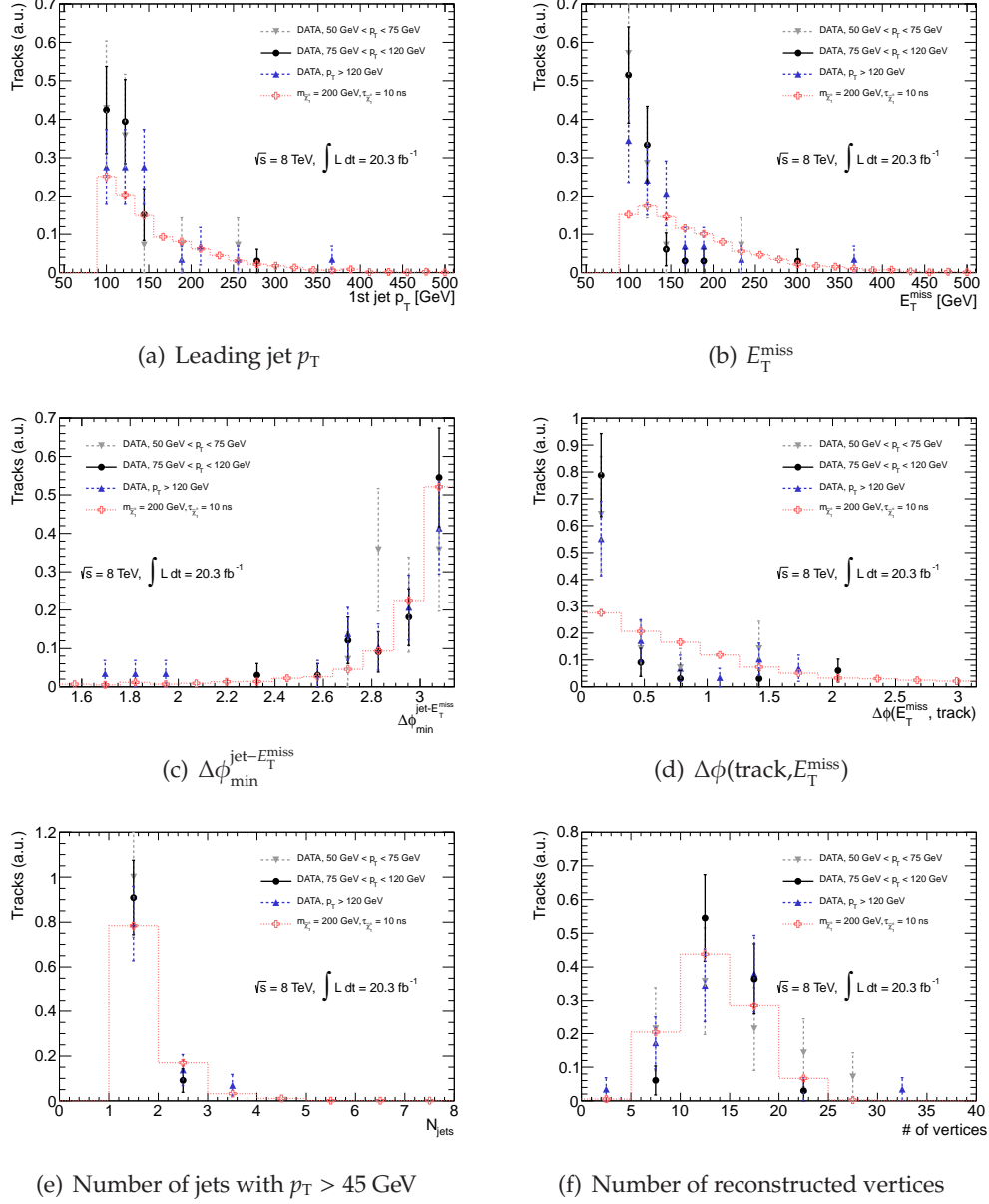 Fig. 12.1. The expected limit is set by the median of the distribution of 95% CL limits derived by pseudo-experiments with the expected background and no signal, where the systematic parameters are varied according to their systematic uncertainties. The regions excluded by the previous ATLAS search [13] and the LEP2 searches are also indicated: the example of the exclusion reached by the ALEPH experiment [28] of 88 GeV at 95% CL that is derived for the chargino mass in the case of heavy sfermions, irrespective of the chargino-neutralino mass difference is shown as LEP2 result.

The analysis is not performed for signals having $\tau_{\tilde{\chi}_1} > 10$ ns (corresponding $\Delta m_{\tilde{\chi}_1}$ being below the charged pion mass) because a significant fraction of charginos would traverse the ID before decaying, thereby reducing the event selection efficiency. In these scenarios, the charginos are considered as stable particles and the main search tool would be to look for tracks with anomalous ionization energy loss. In comparison with the previous result, the sensitivity to charginos having $\tau_{\tilde{\chi}_1^\pm} < 1$ ns is significantly improved and the exclusion reach is extended by ~ 200 GeV.

Figure 12.2 shows the constraint on the allowed $\Delta m_{\tilde{\chi}_1}$–$m_{\tilde{\chi}_1^\pm}$ parameter space of the AMSB model; the expected 95% CL exclusion reaches $m_{\tilde{\chi}_1^\pm} = 245^{+25}_{-30}$ GeV for $\Delta m_{\tilde{\chi}_1} \sim 160$ MeV. The limits on $\tau_{\tilde{\chi}_1^\pm}$ are converted onto $\Delta m_{\tilde{\chi}_1}$ following Ref. [107]. The theoretical prediction of $\Delta m_{\tilde{\chi}_1}$ for wino-like lightest chargino and neutralino states at two-loop level [25] is also indicated in the figure. A new limit that excludes charginos of $m_{\tilde{\chi}_1^\pm} < 270$ GeV (corresponding $\Delta m_{\tilde{\chi}_1}$ and $\tau_{\tilde{\chi}_1^\pm}$ being ~ 160 MeV and ~ 0.2 ns, respectively) at 95% CL is set in the AMSB model.

Figure 12.3 shows the constraint on the allowed $m_{3/2} - m_0$ parameter space of the AMSB model. The limit on the gravitino mass $m_{3/2}$ is calculated by Eq. 2.12. The shaded gray region is excluded theoretically because sleptons become tachyons due to small m_0. The shaded light blue region is also excluded due to no electroweak symmetry breaking. The gravitino with $m_{3/2} < 96$ TeV is excluded at 95% CL in the AMSB model.
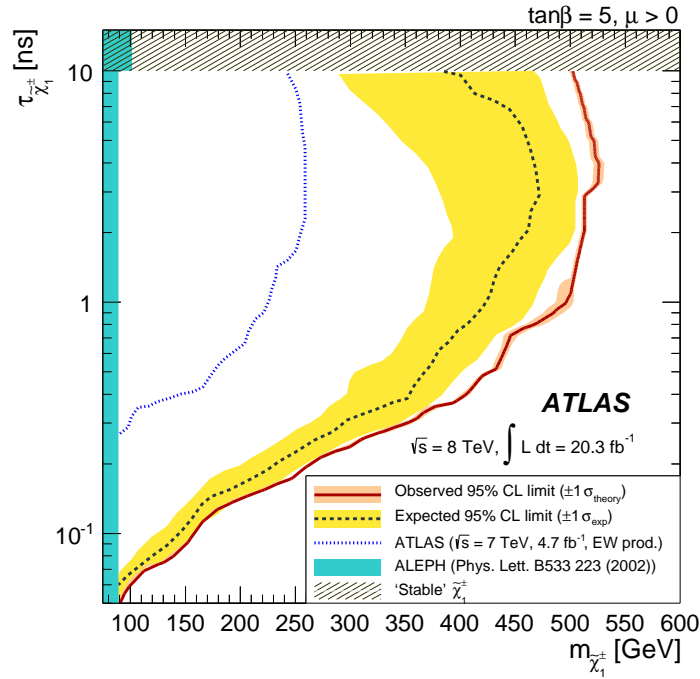
Figure 12.1: Constraint on the allowed $\tau_{\tilde{\chi}_1^\pm} - m_{\tilde{\chi}_1^\pm}$ space for $\tan\beta = 5$ and $\mu_H > 0$. The black dashed line shows the expected limits at 95% CL, with the surrounding shaded band indicating the 1σ exclusions due to experimental uncertainties. Observed limits are indicated by the solid bold contour representing the nominal limit and the narrow surrounding shaded band is obtained by varying the cross-section by the theoretical scale and PDF uncertainties. The previous result from Ref. [13] and an example of the limits achieved at LEP2 by the ALEPH experiment [28] are also shown on the left by the dotted line and the shaded region, respectively. The search for charginos with long lifetimes, as indicated by the upper shaded region, is not covered by this analysis. The limits achieved at LEP2 by the ALEPH experiment of 101 GeV for long-lived charginos is taken from [28].
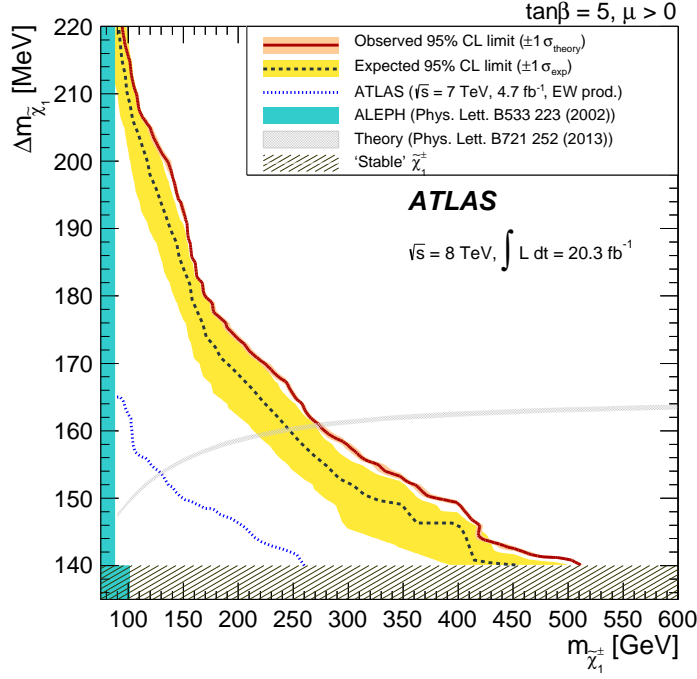
Figure 12.2: Constraint on the allowed $\Delta m_{\tilde{\chi}_1}$–$m_{\tilde{\chi}_1^\pm}$ space of the AMSB model for $\tan\beta = 5$ and $\mu_H > 0$. The dashed line shows the expected limits at 95% CL, with the surrounding shaded band indicating the 1σ exclusions due to experimental uncertainties. Observed limits are indicated by the solid bold contour representing the nominal limit and the narrow surrounding shaded band is obtained by varying the cross-section by the theoretical scale and PDF uncertainties. The previous result from Ref. [13] and an example of the limits achieved at LEP2 by the ALEPH experiment [28] are also shown on the left by the dotted line and the shaded region, respectively. Charginos in the lower shaded region could have significantly longer lifetime values for which this analysis has no sensitivity as the chargino does not decay within the tracking volume. For this region of long-lived charginos, the limits achieved at LEP2 by the ALEPH experiment is 101 GeV [28].

12.2 Constraints on the Pure Gravity Mediation model

The result is interpreted in the framework of the PGM model. The difference between the AMSB and PGM models is that the gauginos in the PGM model obtain their masses from additional contributions from threshold effects of the heavy Higgsinos. The gluino mass is about eight times higher than the wino mass for L = 0 as in the AMSB model, while the mass ratio of gluino to wino not differ in the PGM model. Therefore, the results set by this analysis can be interpreted in the framework of the PGM model.
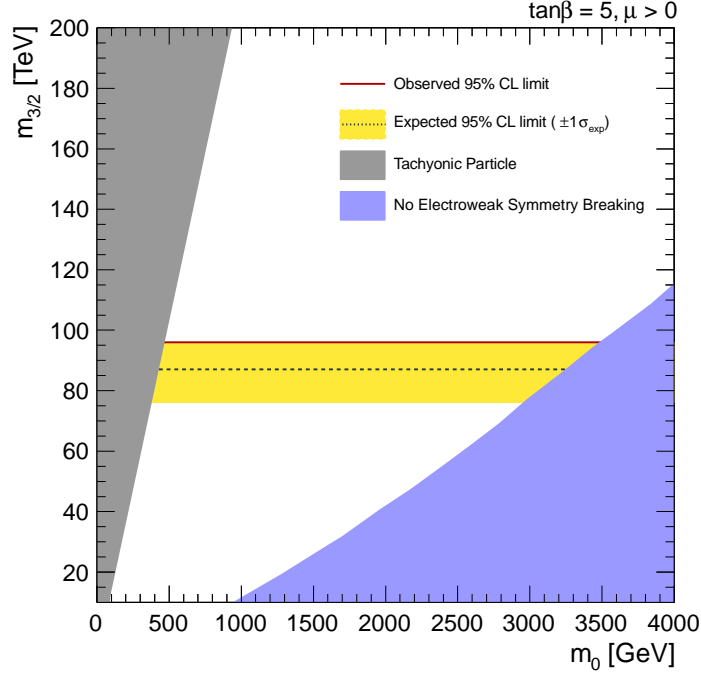
Figure 12.3: Constraint on the allowed $m_{3/2}$–m_0 space of the AMSB model for $\tan\beta = 5$ and $\mu_{\mathrm{H}} > 0$. The dashed line shows the expected limits at 95% CL, with the surrounding shaded band indicating the 1σ exclusions due to experimental uncertainties. Observed limits are indicated by the solid red line. The shaded gray region is theoretically excluded because sleptons become tachyons due to small m_0. The shaded light blue region is also theoletically excluded due to no electroweak symmetry breaking.

Figure 12.4 shows the relation between $m_{\tilde{\chi}_1^0}$ and $m_{\tilde{g}}$ in the PGM model for a given L. The red lines show the predictions for $L/m_{3/2} = 0$, 1 and 2. The gray shaded region is not favored because the gluino becomes LSP ($m_{\tilde{g}} < m_{\tilde{\chi}_1^0}$), and the light violet shaded regions are excluded at 95 % CL by this analysis. The constraint obtained by the search via the gluino pair production process [108] is also shown. This analysis excludes the gluino having a mass up to 2240, 1200 and 840 GeV for $L/m_{3/2} = 0$, 1 and 2, respectively. A limit on the gluino mass of 2.2 TeV in the AMSB model ($L/m_{3/2} = 0$), achieved by this analysis, is more stringent than that obtained by the search for the gluino pair production process giving a limit of $\sim$ 1.4 TeV [108].
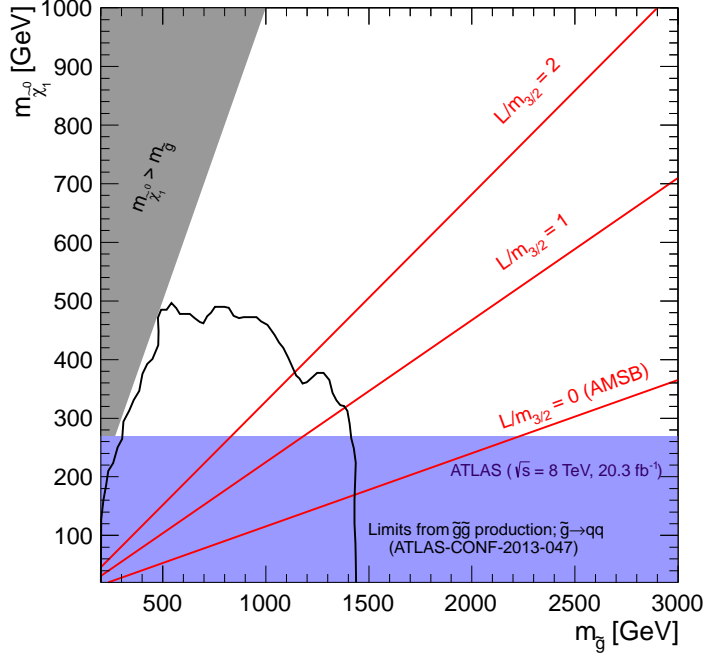
Figure 12.4: Relation between $m_{\tilde{\chi}_1^0}$ and $m_{\tilde{g}}$ in the PGM model for a given L. The red lines show the predictions with $L/m_{3/2} = 0$, 1 and 2, respectively. The gray shaded region is not favored because gluino becomes LSP ($m_{\tilde{g}} < m_{\tilde{\chi}_1^0}$), and the light violet shaded region is excluded by this analysis. The constraint obtained by the search for the gluino pair production process [108] is also shown.

12.3 Constraints on wino dark matter

The result is also interpreted in the framework of wino dark matter scenarios, and the limit on the annihilation cross-section is set. As stated in Sec. 2.3.5, the wino annihilation cross-section in the thermal scenario is less constrained by the indirect searches especially in the low mass region. Figure 12.5 shows the constraints on the annihilation cross-section as a function of the wino mass [32] on top of Fig. 2.11. A new limit on the wino dark matter with $m_{\tilde{\chi}_1^0} < 270$ GeV is set. In the thermal scenario, the collider experiments have better sensitivity than that of indirect searches in the low mass region. The constraint on the wino annihilation cross-section in the non-thermal scenario is also shown in Fig. 12.6.

12.4 Discussion

This analysis, based on 20.3 fb^{-1} of 8 TeV *pp* collision data, has increased the sensitivity compared to the previous ATLAS searches [9, 13] due to analysis im-

Figure 12.5: Constraints on the annihilation cross-section as a function of the wino mass [32]. The theoretical cross-section of annihilation into W^+ W^-, γ γ and γ Z final states are also indicated by the dashed red line and the solid blue line, respectively. The shaded green region is excluded by this result. The excluded regions by the Fermi and H.E.S.S. observations are indicated by the shaded red region and the shaded blue region, respectively. These exclusion contours are obtained on the assumption that the wino abundance is set by thermal freeze-out. The shaded yellow region between the dotted lines corresponds to $\Omega h^2 = 0.12 \pm 0.06$. In the black shaded region, a thermal wino exceeds the observed relic density.

provements and increases in the beam energy and luminosity. The most significant improvement is achieved by enhancing the track reconstruction efficiency for charginos having short decay length and the trigger efficiency by adopting a dedicated topological trigger. In particular, the efficiency for charginos with $\tau_{\tilde{\chi}_1^\pm} \sim 0.2$ ns, predicted for $\Delta m_{\tilde{\chi}_1} \sim 160$ MeV, is around 100 times larger than in the previous searches. This analysis significantly surpasses the reach of the LEP experiments, and a chargino mass below 270 GeV is excluded at 95% CL, which also directly constrains the mass of wino dark matter..

The center-of-mass energy will be increased to 14 TeV in 2015 with a peak instantaneous luminosity of $\sim 10^{34}$cm^{2}s^{-1}. In order to estimate the expected sensitivity with $\sqrt{s} = 14$ TeV data, two benchmark values of integrated luminosity are
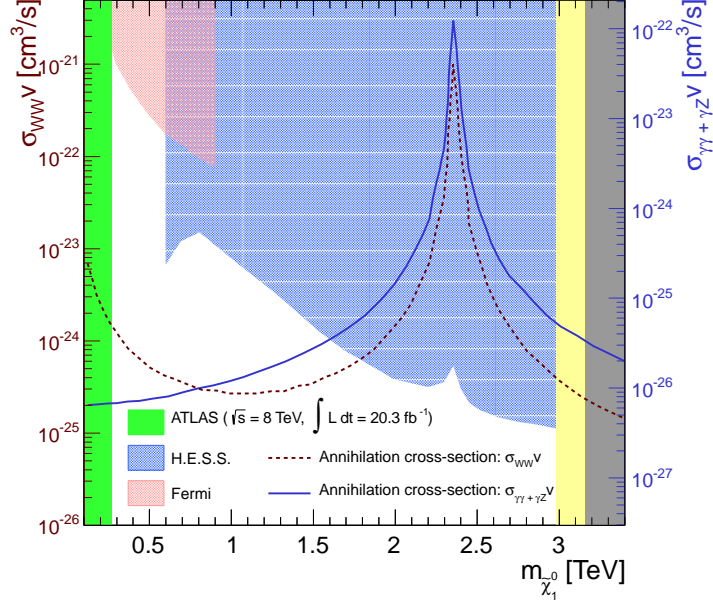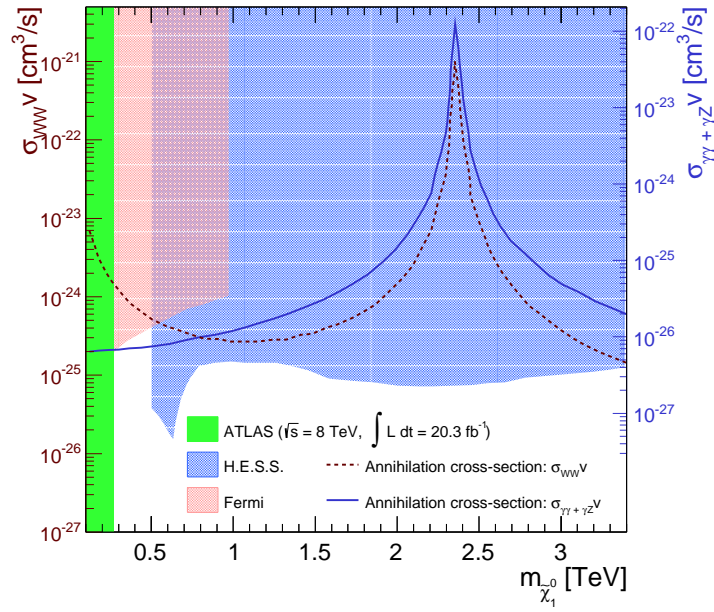
Figure 12.6: Constraints on the annihilation cross-section as a function of the wino mass [32]. The theoretical cross-section of annihilation into W^+ W^-, γ γ and γ Z final states are also indicated by the dashed red line and the solid blue line, respectively. The shaded green region is excluded by this result. The excluded regions by the Fermi and H.E.S.S. observations are indicated by the shaded red region and the shaded blue region, respectively. These exclusion contours are obtained on the assumption that the wino comprises all dark matter due to a non-thermal history.

considered: the integrated luminosity of 20 (100) fb^{-1} will be achieved by the end of 2016 (2018). Figure 12.7 shows the expected 5 σ discovery reach in the $\tau_{\tilde{\chi}_1^\pm}-m_{\tilde{\chi}_1^\pm}$ space using 20 fb^{-1} and 100 fb^{-1} data at $\sqrt{s} = 14$ TeV. These are calculated on the assumption that the same signal selection efficiency and signal-to-background ratio achieved in the 8 TeV analysis. A chargino mass up to 500 GeV can be explored with the early $\sqrt{s} = 14$ TeV data.
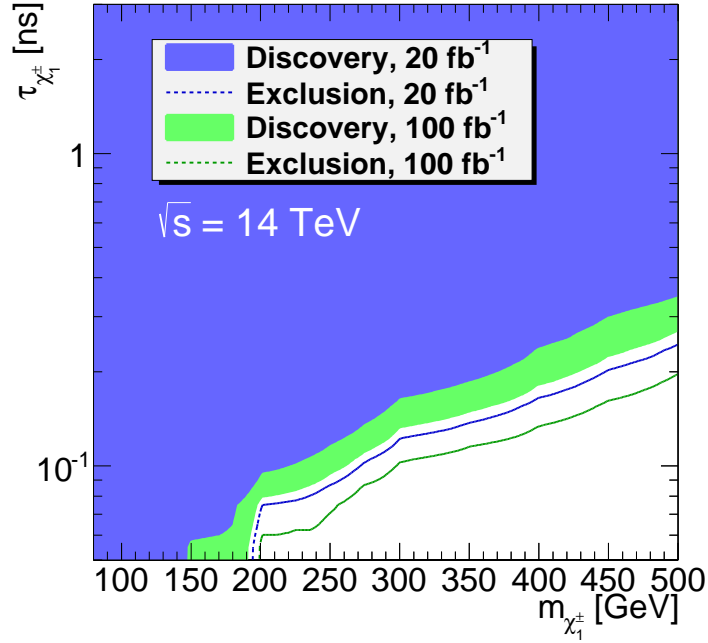
Figure 12.7: Expected 5 σ discovery reach at $\sqrt{s} = 14$ TeV with 20fb^{-1} (light blue) and 100fb^{-1} (green) data in the $\tau_{\tilde{\chi}_1^\pm}-m_{\tilde{\chi}_1^\pm}$ space.

In 14 TeV *pp* collisions, a fourth pixel layer [109] will be installed between a new beryllium beam-pipe and the current b-layer, which enhances the tracking performance in a high-luminosity. This additional layer of pixel detector may help to reconstruct the chargino tracks that decay before reaching the SCT detector. The signal track reconstruction efficiency in the 14 TeV run is therefore expected to be much larger than that in the 8 TeV run, which provides a capability of exploring a chargino being much heavier and having a smaller production cross-section.

Chapter 13

Conclusions

A search is presented for direct chargino production based on a disappearing-track signature using 20.3 fb^{-1} of pp collisions at $\sqrt{s} = 8$ TeV collected with the ATLAS experiment at the LHC.

Anomaly-Mediated Supersymmetry Breaking model, where the SUSY breaking is caused by loop effects, provides a constrained mass spectrum of SUSY particles. One prominent feature of these models is that the LSP is the nearly pure neutral wino that is mass-degenerate with the charged wino. The lightest chargino is slightly heavier than the lightest neutralino due to radiative corrections involving electroweak gauge bosons. The typical mass splitting between $\tilde{\chi}_1^{\pm}$ and $\tilde{\chi}_1^0$ is ~ 160 MeV, which implies that $\tilde{\chi}_1^{\pm}$ has a significant lifetime and predominantly decays into $\tilde{\chi}_1^0$ plus a low-momentum $\pi^{\pm}$. The mean lifetime of $\tilde{\chi}_1^{\pm}$ is expected to be typically a fraction of a nanosecond. Therefore, some charginos could have decay length exceeding a few tens of centimeters at the LHC. When decaying in the sensitive volume, they are expected to be observed as "disappearing tracks" that have no more than a few associated hits in the outer region of the tracking system, and the softly emitted $\pi^{\pm}$ is not reconstructed. This dissertation explores AMSB scenarios by searching for charginos with their subsequent decays that result in such disappearing tracks.

A new method to detect charginos that decay before reaching the SCT detector called "Re-tracking" has been developed in this dissertation. In the search based on the 7 TeV dataset, the Re-tracking was not adopted and the sensitivity to charginos having a fraction of a nanosecond was limited. The Re-tracking requires a minimum of three pixel hits and provides a fully efficient tracking capability for charginos traversing the pixel detector. The efficiency for charginos with $\tau_{\tilde{\chi}_1^{\pm}} \sim 0.2$ ns, is around 100 times larger than that in the previous searches.

The signal topology is characterized by a high p_T jet, large E_T^{miss}, and a high-p_T disappearing track. The SM processes can result in final-state kinematics similar to that of the signal, therefore, the signal events can not be enhanced by any kinematic selection requirements. In this dissertation, a dedicated topological trigger is developed to attain a higher signal efficiency.

There are three types of background tracks: interacting-hadron tracks, charged leptons failing to satisfy their identification criteria, and p_T-mismeasured tracks. A background estimation based on the MC simulation suffers from large uncertainties due to the poor statistics and has difficulty simulating the properties of background tracks. Therefore, a data-driven approach has been developed to estimate the background track-p_T spectrum.

No significant excess above the background expectation is observed for candidate tracks with large p_T, and constraints on the AMSB model are obtained. In the AMSB model, a chargino mass below 270 GeV is excluded at 95% CL. Given the ratio M_3/M_2 of ~ 8, a gluino mass below 2240 GeV is excluded at 95% CL, which is more stringent than that obtained via inclusive searches for squark and gluino production giving a limit of ~ 1.4 TeV on a gluino mass. The results are also interpreted in the framework of the Pure Gravity Mediation model. In the PGM model, the gluino having a mass up to 2240, 1200, and 840 GeV for $L/m_{3/2} = 0$, 1, and 2 is excluded at 95% CL, respectively. Finally, the results are interpreted in the context of the wino dark matter scenario. A wino dark matter with a mass below 270 GeV is excluded at 95% CL.

Acknowledgments

I hereby would like to acknowledge the help and support I have received from many people throughout my Ph.D studies.

First of all, I would like to sincerely thank my supervisor, Prof. Tomio Kobayashi for giving me the opportunity to perform my Ph.D studies within the ATLAS group of the University of Tokyo. I am very grateful for the encouragement, guidance, and dedicated support that I have received from him.

I would like to express my great appreciation to Prof. Shoji Asai for his continuous assistance and guidance. He taught me the basics of high energy physics and guided me to the world of elementary particle physics, especially the world of supersymmetry.

My deepest gratitude goes to Prof. Shimpei Yamamoto for his passionate guidance, sincere advice, and great encouragement. Whenever I was confronted with a difficulty in my study, he helped me a lot and guided the work to the right direction with his experience. Without his help, my dissertation would never have completed.

I would like to thank Dr. Frederic Brochu for teaching me the tracking software. The significant improvements that were achieved in my study would never have realized without his help.

I would like to thank Dr. Toshio Namba for teaching me experimental techniques when I was a master's student.

I am very grateful to all the members of the University of Tokyo and ATLAS Japan group at CERN, Prof. Tatsuo Kawamoto, Prof. Junichi Tanaka, Prof. Naoko Kanaya, Prof. Ikuo Ueda, Prof. Koji Terashi, Prof. Yuji Enari , Prof. Koji Nakamura, Prof. Yousuke Kataoka, Dr. Tatsuya Masubuchi, Dr. Takashi Yamanaka, Dr. Keita Hanawa, Mr. Takuya Nobe, Mr. Ryo Nagai, Mr. Masahiro Morinaga, and Mr. Yuto Minami for their guidance, advice, and help throughout my time at CERN. I would like to thank Prof. Tetsuro Mashimo, Prof. Yoshizumi Inoue, Prof. Tomoaki Nakamura, and Mr. Nagataka Matsui for providing me an excellent computing environment for data analysis at Tokyo.

I appreciate the conveners and the collaborators of the SUSY working group; Prof. Pascal Pralavorio, Prof. Andreas Hoecker, Dr. Monica D'Onofrio, Dr. Nick Barlow, Dr. David Miller, Prof. Christoph Rembser, Prof. Andy Haas, and Prof. Claudia Gemme gave me useful advice and excellent suggestions to my study.

157

I am very happy to have many friends in the same period; Mr. Yuichi Sasaki, Mr. Akira Miyazaki, Mr. Yohei Yamaguchi, Mr. Yutaro Iiyama, Mr. Keisuke Yoshihara, Mr. Yoichi Ninomiya, Mr. Yuki Fujii, and Mr. Kim Siang Khaw. It is my great honor that I was able to work with them, and I am looking forward to working together in the near future.

A big thank you goes of course to all the other members from the University of Tokyo for providing a very friendly, collaborative, and productive working atmosphere: Prof. Akira Ishida, Dr. Takayuki Yamazaki, Mr. Ginga Akimoto, Mr. Inada Toshiaki, Ms. Aine Kobayashi, Ms. Maya Okawa, Mr. Yuki Kawanishi, Mr. Chikuma Kato, Mr. Syunsuke Adachi, Mr. Tomohiro Yamaji, Mr. Shingo Terao, Mr. Shingo Hisajima, and Mr. Yuji Minegishi.

I would like to thank all the members of my choir, scatola di voce. Whenever I came back to Japan from CERN, they warmly welcomed me and encouraged me by their excellent performances.

Last but not least, I would like to thank my family for supporting my decision to study physics and their constant encouragement.

Bibliography

[1] G. F. Giudice, M. A. Luty, H. Murayama, and R. Rattazzi, *Gaugino Mass without Singlets*, JHEP **12** (1998) 027, `arXiv:hep-ph/9810442`.

[2] L. Randall and R. Sundrum, *Out of this world supersymmetry breaking*, Nucl. Phys. **B557** (1999) 79, `arXiv:hep-th/9810155`.

[3] M. Ibe, S. Matsumoto, and T. T. Yanagida, *Pure Gravity Mediation with $m_{3/2}$ = 10-100 TeV*, Phys. Rev. **D85** (2012) 095011, `arXiv:1202.2253 [hep-ph]`.

[4] L. J. Hall, Y. Nomura, and S. Shirai, *Spread Supersymmetry with Wino LSP: Gluino and Dark Matter Signals*, JHEP **1301** (2013) 036, `arXiv:1210.2395 [hep-ph]`.

[5] A. Arvanitaki, N. Craig, S. Dimopoulos, and G. Villadoro, *Mini-Split*, JHEP **1302** (2013) 126, `arXiv:1210.0555 [hep-ph]`.

[6] N. Arkani-Hamed, A. Gupta, D. E. Kaplan, N. Weiner, and T. Zorawski, *Simply Unnatural Supersymmetry*, `arXiv:1212.6971 [hep-ph]`.

[7] J. Hisano, S. Matsumoto, M. Nagai, O. Saito, and M. Senami, *Non-perturbative Effect on Thermal Relic Abundance of Dark Matter*, Phys. Lett. **B646** (2007) 34–38, `arXiv:0610249 [hep-ph]`.

[8] T. Moroi and L. Randall, *Wino cold dark matter from anomaly mediated SUSY breaking*, Nucl. Phys. **B570** (2000) 455–472, `arXiv:hep-ph/9906527`.

[9] ATLAS Collaboration, *Search for anomaly-mediated supersymmetry breaking with the ATLAS detector based on a disappearing-track signature in pp collisions at $\sqrt{s}$ = 7 TeV*, Eur.Phys.J. **C72** (2012) 1993, `arXiv:1202.4847 [hep-ex]`.

[10] ATLAS Collaboration, *Search for long-lived charginos in anomaly-mediated supersymmetry breaking scenarios with the ATLAS detector using 4.7 fb^{-1} data of pp collisions at $\sqrt{s}$ = 7 TeV*, Tech. Rep. ATLAS-CONF-2012-034, CERN, Geneva, Mar, 2012.

[11] Y. Azuma, *Search for Long-lived Chargino with Anomaly-Mediated Supersymmetry Breaking Scenarios in pp Collisions at $\sqrt{s}$ = 7 TeV*. PhD thesis, The University of Tokyo, 2012.

[12] ATLAS Collaboration, *Search for squarks and gluinos with the ATLAS detector in final states with jets and missing transverse momentum and 20.3 fb^{-1} of $\sqrt{s} = 8$ TeV proton-proton collision data*, Tech. Rep. ATLAS-CONF-2013-047, CERN, Geneva, May, 2013.

[13] ATLAS Collaboration, *Search for direct chargino production in anomaly-mediated supersymmetry breaking models based on a disappearing-track signature in pp collisions at $\sqrt{s} = 7$ TeV with the ATLAS detector*, JHEP **1301** (2013) 131, `arXiv:1210.2852 [hep-ex]`.

[14] F. Englert and R. Brout, *Broken symmetry and the mass of gauge vector meson*, Phys. Rev. Lett. **13** (1964) 321.

[15] P. W. Higgs, *Broken symmetry, massless particles and gauge field*, Phys. Lett. **12** (1964) 132.

[16] ATLAS Collaboration, *Observation of a new particle in the search for the Standard Model Higgs boson with the ATLAS detector at the LHC*, Phys. Lett. **B716** (2012) 1–29, `arXiv:1207.7214 [hep-ex]`.

[17] C. Collaboration, *Observation of a new boson at a mass of 125 GeV with the CMS experiment at the LHC*, Phys. Lett. **B716** (2012) 30–61, `arXiv:1207.7235 [hep-ex]`.

[18] `http://en.wikipedia.org/wiki/Standard_Model`.

[19] J. L. Feng, *Naturalness and the Status of Supersymmetry*, `http://arxiv.org/abs/1302.6587`, 2013. `arXiv:1302.6587 [hep-ph]`.

[20] S. P. Martin, *A Supersymmetry Primer*, `http://arxiv.org/abs/hep-ph/9709356`, 1997. `arXiv:hep-ph/9709356`.

[21] Particle Data Group Collaboration, K. Nakamura et al., *Review of particle physics*, J. Phys. **G37** (2010) 075021 (398–399).

[22] G.D. Coughlan *et al.*, *Cosmological problems for the polonyi potential*, Phys. Lett. **B131** (1983) 59.

[23] M. Ibe, Y. Shinbara, and T.T. Yanagida, *The Polonyi Problem and Upper bound on Inflation Scale in Supergravity*, Phys. Lett. **B639** (2006) 534, `arXiv:0605252 [hep-ph]`.

[24] K. Huitu, J. Laamanen, and P. N. Pandita, *Sparticle spectrum and constraints in anomaly mediated supersymmetry breaking models*, Phys. Rev. D **65** (2010) 115003–1.

[25] M. Ibe, S. Matsumoto, and R. Sato, *Mass Splitting between Charged and Neutral Winos at Two-Loop Level*, Phys.Lett. **B721** (2013) 252–260, `arXiv:1212.5989 [hep-ph]`.

[26] O. Yasuhiro, Y. Masahiro, and Y. Tsutomu, *Upper Bound of the Lightest Higgs Boson Mass in the Minimal Supersymmetric Standard Model*, Prog. Theor. Phys. **85 (1)** (1991) 1–5.

[27] F. Gabbiani, E. Gabrielli, A. Masiero, and L. Silvestrini, *A complete analysis of FCNC and CP constraints in general SUSY extensions of the standard model*, Nucl. Phys. **B477** (1996) 321–352, arXiv:hep-ph/9604387.

[28] ALEPH Collaboration, *Search for charginos nearly mass degenerate with the lightest neutralino in e+ e- collisions at center-of-mass energies up to 209-GeV*, Phys.Lett. **B533** (2002) 223–236, arXiv:hep-ex/0203020 [hep-ex].

[29] OPAL Collaboration, *Search for nearly mass degenerate charginos and neutralinos at LEP*, Eur.Phys.J. **C29** (2003) 479–489, arXiv:hep-ex/0210043 [hep-ex].

[30] DELPHI Collaboration, *Search for SUSY in the AMSB scenario with the DELPHI detector*, Eur.Phys.J. **C34** (2004) 145–156, arXiv:hep-ex/0403047 [hep-ex].

[31] http://lepsusy.web.cern.ch/lepsusy/www/inoslowdmsummer02/ charginolowdm_pub.html.

[32] T. Cohen, M. Lisanti, A. Pierce, and T.R. Slatyer, *Wino Dark Matter Under Siege*, http://arxiv.org/abs/1307.4082, 2013. arXiv:1307.4082 [hep-ph].

[33] J. Fan and M. Reece, *In Wino Veritas? Indirect Searches Shed Light on Neutralino Dark Matter*, http://arxiv.org/abs/1307.4400, 2013. arXiv:1307.4400 [hep-ph].

[34] Fermi-LAT Collaboration, *Constraining Dark Matter Models from a Combined Analysis of Milky Way Satellites with the Fermi Large Area Telescope*, Phys. Rev. Lett. **107** (2011) 241302, arXiv:1108.3546 [astro-ph].

[35] H.E.S.S. Collaboration, *Search for photon line-like signatures from Dark Matter annihilations with H.E.S.S*, Phys. Rev. Lett. **110** (2013) 041301, arXiv:1301.1173 [astro-ph].

[36] PAMELA Collaboration, *PAMELA results on the cosmic-ray antiproton flux from 60 MeV to 180 GeV in kinetic energy*, Phys. Rev. Lett. **105** (2010) 121101, arXiv:1007.0821 [astro-ph].

[37] J. Hisano, K. Ishiwata, and N. Nagata, *A complete calculation for direct detection of Wino dark matter*, Phys.Lett. **B706** (2011) 208, arXiv:hep-ph/1004.4090.

[38] J. Hisano, K. Ishiwata, N. Nagata, and T. Takesako, *Direct Detection of Electroweak-Interacting Dark Matter*, JHEP **1107** (2011) 005, arXiv:hep-ph/1104.0228.

[39] XENON100 Collaboration, *Dark Matter Results from 225 Live Days of XENON100 Data*, Phys. Rev. Lett. **109** (2012) 181301, arXiv:1207.5988 [hep-ex].

[40] ATLAS Collaboration, *ATLAS detector and physics performance : Technical Design Report, 1*, tech. rep., CERN, 1999. ATLAS-TDR-014, CERN-LHCC-99-014.

[41] ATLAS Collaboration, *ATLAS detector and physics performance : Technical Design Report, 2*, tech. rep., CERN, 1999. ATLAS-TDR-015, CERN-LHCC-99-015.

[42] ATLAS Collaboration, *ATLAS Experiment at the CERN Large Hadron Collider*, JINST **3** (2008) S08003.

[43] CMS Collaboration, *CMS technical proposal*, tech. rep., CERN, 1994. CERN-LHCC-894-38.

[44] LHCb Collaboration, *LHCb technical proposal*, tech. rep., CERN, 1998. CERN-LHCC-98-004.

[45] ALICE Collaboration, *ALICE: Technical proposal for a Large Ion collider Experiment at the CERN LHC*, tech. rep., CERN, 1997. CERN-LHCC-95-71.

[46] A. Yamamoto *et al.*, *Progress in ATLAS Central Solenoid Magnet*, IEEE Trans. Appl. Supercond. **10** (2000) 353.

[47] P. Védrine *et al.*, *Manufacturing and integration progress of the ATLAS barrel toroid magnet at CERN*, IEEE Trans. Appl. Supercond. **16** (2006) 553.

[48] ATLAS Collaboration, *ATLAS inner detector: Technical Design Report, 1*, tech. rep., CERN, Geneva, 1997. CERN-LHCC-97-016.

[49] ATLAS Collaboration, *ATLAS inner detector: Technical Design Report, 2*, tech. rep., CERN, Geneva, 1997. CERN-LHCC-97-017.

[50] ATLAS Pixel Collaboration, *ATLAS pixel detector electronics and sensors*, JINST **3** (2008) P07007.

[51] ATLAS SCT Collaboration, *The barrel modules of the ATLAS semiconductor tracker*, Nucl. Instrum. Meth. **A568** (2006) 642–671.

[52] ATLAS SCT Collaboration, *The ATLAS semiconductor tracker end-cap module*, Nucl. Instrum. Meth. **A575** (2007) 353–389.

[53] ATLAS SCT Collaboration, *The silicon microstrip sensors of the ATLAS semiconductor tracker*, Nucl. Instrum. Meth. **A578** (2007) 98–118.

[54] ATLAS TRT Collaboration, *The ATLAS Transition Radiation Tracker (TRT) proportional drift tube: design and performance*, JINST **3** (2008) P02013.

[55] ATLAS TRT Collaboration, *The ATLAS TRT Barrel Detector*, JINST **3** (2008) P02014.

[56] ATLAS TRT Collaboration, *The ATLAS TRT end-cap detectors*, JINST **3** (2008) P10003.

[57] ATLAS Collaboration, *ATLAS calorimeter performance : Technical Design Report*, tech. rep., CERN, 1996. ATLAS-TDR-1, CERN-LHCC-96-040.

[58] ATLAS Collaboration, *ATLAS liquid-argon calorimeter : Technical Design Report*, tech. rep., CERN, 1996. ATLAS-TDR-2, CERN-LHCC-96-041, CERN/LHCC 96-41.

[59] ATLAS Collaboration, *ATLAS tile calorimeter : Technical Design Report*, tech. rep., CERN, 1996. ATLAS-TDR-3, CERN-LHCC-96-042.

[60] D.M. Gingrich *et al.*, *Construction, Assembly and Testing of the ATLAS Hadronic End-cap Calorimeter* , JINST **2** (2007) P05005.

[61] A. Artamonov *et al.*, *The ATLAS Forward Calorimeter*, JINST **3** (2008) P02010.

[62] ATLAS Collaboration, *ATLAS muon spectrometer : Technical Design Report*, tech. rep., CERN, 1997. ATLAS-TDR-10 ; CERN-LHCC-97-022.

[63] ATLAS Collaboration, *ATLAS Forward Detectors for Measurement of Elastic Scattering and Luminosity*, tech. rep., CERN, 2008. ATLAS-TDR-18 ; CERN-LHCC-2008-004.

[64] ATLAS Collaboration, *ATLAS level-1 trigger : Technical Design Report*, tech. rep., CERN, 1998. ATLAS-TDR-12 ; CERN-LHCC-98-014.

[65] ATLAS Collaboration, *ATLAS high-level trigger, data-acquisition and controls : Technical Design Report*, tech. rep., CERN, 2003. ATLAS-TDR-16 ; CERN-LHCC-2003-022.

[66] ATLAS Collaboration, *Luminosity Determination in pp Collisions at sqrts=7 TeV Using the ATLAS Detector at the LHC*, Eur.Phys.J. **C71** (2011) 1630, arXiv:1101.2185 [hep-ex].

[67] ATLAS Collaboration, *Improved luminosity determination in pp collisions at $\sqrt{s}$ = 7 TeV using the ATLAS detector at the LHC*, arXiv:1302.4393 [hep-ex].

[68] J. Pumplin et al., *New generation of parton distributions with uncertainties from global QCD analysis*, JHEP **07** (2002) 012, `arXiv:hep-ph/0201195`.

[69] A. Martin, W. Stirling, R. Thorne, and G. Watt, *Parton distributions for the LHC*, Eur. Phys. J. **C63** (2009) 189, `arXiv:0901.0002 [hep-ph]`.

[70] M. Guzzi *et al.*, *CT10 parton distributions and other developments in the global QCD analysis*, `arXiv:1101.0561 [hep-ph]`.

[71] T. Sjostrand, S. Mrenna, and P. Z. Skands, *A Brief Introduction to PYTHIA 8.1*, Comput. Phys. Commun. **178** (2008) 852–867, `arXiv:0710.3820`.

[72] ATLAS Collaboration, *Further ATLAS tunes of PYTHIA 6 and Pythia 8*, 2011. ATL-PHYS-PUB-2011-014.

[73] GEANT4 Collaboration, S. Agostinelli et al., *GEANT4: A simulation toolkit*, Nucl. Instrum. Meth. **A506** (2003) 250–303.

[74] ATLAS Collaboration, *The ATLAS Simulation Infrastructure*, Eur. Phys. J. **C70** (2010) 823–874, `arXiv:1005.4568 [physics.ins-det]`.

[75] F. E. Paige, S. D. Protopopescu, H. Baer, and X. Tata, *ISAJET 7.69: A Monte Carlo event generator for pp, anti-p p, and e+e- reactions*, `arXiv:hep-ph/0312045 [hep-ph]`.

[76] M. Bahr et al., *Herwig++ Physics and Manual*, Eur.Phys.J. **C58** (2008) 639–707, `arXiv:0803.0883 [hep-ph]`.

[77] W. Beenakker, R. Hopker, M. Spira, and P. Zerwas, *Squark and gluino production at hadron colliders*, Nucl.Phys. **B492** (1997) 51–103, `arXiv:hep-ph/9610490 [hep-ph]`.

[78] P. M. Nadolski *et al.*, *Implications of CTEQ global analysis for collider observation*, Phys. Rev. **D78** (2008) 013004, `arXiv:0802.0007 [hep-ph]`.

[79] M. Botje *et al.*, *The PDF4LHC Working Group Interim Recommendations*, `arXiv:1101.0538 [hep-ph]`.

[80] M. L. Mangano *et al.*, *ALPGEN, a generator for hard multiparton processes in hadronic collisions*, JHEP **0307** (2003) 001, `arXiv:hep-ph/0206293 [hep-ph]`.

[81] G. Corcella *et al.*, *HERWIG 6.5: an event generator for Hadron Emission Reactions With Interfering Gluons (including supersymmetric processes)*, JHEP **01** (2001) 010.

[82] J. M. Butterworth, J. R. Forshaw and M. H. Seymour, *Multiparton interactions in photoproduction at HERA*, Z. Phys C **72** (1996) 637–646. `arXiv:hep-ph/9601371`.

[83] J. Alwall *et al.*, *Comparative study of various algorithms for the merging of parton showers and matrix elements in hadronic collisions*, Eur. Phys. J. C **53** (2008) 473. `arXiv:0706.2569 [hep-ph]`.

[84] P. Nason, *A New Method for Combining NLO QCD with Shower Monte Carlo Algorithms*, JHEP **11** (2004) 040. `arXiv:hep-ph/0409146`.

[85] S. Frixione and B. R. Webber, *The MC@NLO 3.3 event generator*, `arXiv:hep-ph/0612272`.

[86] B. P. Kersevan and E. Richter-Was, *The Monte Carlo event generator AcerMC version 2.0 with interfaces to PYTHiA 6.2 and HERWIG 6.5*, JHEP **06** (2010) 043. `arXiv:hep-ph/0405247`.

[87] T. Sjostrand, S. Mrenna, and P. Z. Skands, *PYTHIA 6.4 Physics and Manual*, JHEP **0605** (2006) 026, `arXiv:hep-ph/0603175`.

[88] S. Catani, L. Cieri, G. Ferrera, D. de Florian, and M. Grazzini, *Vector Boson Production at Hadron Colliders: A Fully Exclusive QCD Calculation at Next-to-Next-to-Leading Order*, Phys. Rev. Lett. **103** (2009) 082001.

[89] T. Cornelisen *et al.*, *The new ATLAS track reconstruction (NEWT)*, J. Phys. Conf. Ser **119** (2008) 032014.

[90] R. Fruhwirth, *Application of Kalman filtering to track and vertex fitting*, Nucl. Instrum. Meth. **A262** (1987) 444–450.

[91] R. Duda and P. Hart, *Use of the Hough Transformation to Detect Lines and Curves in Pictures*, Comm. ACM **15** (1972) 11–15, `1212.5989`.

[92] ATLAS Collaboration, *Performance of primary vertex reconstruction in proton-proton collisions at $\sqrt{s} = 7$ TeV in the ATLAS experiment*, Tech. Rep. ATLAS-CONF-2010-069, CERN, Geneva, Jul, 2010.

[93] ATLAS Collaboration, *Performance of the ATLAS Inner Detector Track and Vertex Reconstruction in the High Pile-Up LHC Environment*, Tech. Rep. ATLAS-CONF-2012-042, CERN, Geneva, Mar, 2012.

[94] M. Cacciari, G. P. Salam, and G. Soyez, *The anti-k_t jet clustering algorithm*, JHEP **04** (2008) 063, `arXiv:0802.1189 [hep-ph]`.

[95] M. Aleksa *et al.*, *ATLAS Combined Testbeam: Computation and Validation of the Electronic Calibration Constatns for the Electromagnetic Calorimeter*, Tech. Rep. ATL-LARG-PUB-2006-003, CERN, Geneva, Jul, 2006.

[96] ATLAS Collaboration, *Jet energy scale and its systematic uncertainty for jets produced in proton-proton collisions at $\sqrt{s} = 7$ TeV and measured with the ATLAS detector*, Tech. Rep. Tech. Rep. ATL-CONF-2010-056, CERN, Geneva, July, 2010.

[97] W. L. *et al.*, *Calorimeter Clustering Algorithms: Description and Performance*, Tech. Rep. ATL-LARG-PUB-2008-002, CERN, Geneva, 2008.

[98] ATLAS Collaboration, *Improved electron reconstruction in ATLAS using the Gaussian Sum Filter-based model for bremsstrahlung*, Tech. Rep. Tech. Rep. ATL-CONF-2012-047, CERN, Geneva, May, 2012.

[99] ATLAS Collaboration, *Muon reconstruction efficiency in reprocessed 2010 LHC proton-proton collision data recorded with the ATLAS detector*, Tech. Rep. Tech. Rep. ATL-CONF-2011-063, CERN, Geneva, 2011.

[100] ATLAS Collaboration, *Measurements of underlying-event properties using neutral and charged particles in pp collisions at 900 GeV and 7 TeV with the ATLAS detector at the LHC*, Eur.Phys.J. **C71** (2011) 1636, arXiv:1103.1816 [hep-ex].

[101] ATLAS Collaboration, *Search for direct third-generation squark pair production in final states with missing transverse momentum and two b-jets in $\sqrt{s} = 8$ TeV pp collisions with the ATLAS detector*, JHEP **1310** (2013) 189, arXiv:1308.2631 [hep-ex].

[102] ATLAS Collaboration, *Jet energy measurement with the ATLAS detector in proton-proton collisions at $\sqrt{s} = 7$ TeV*, Eur.Phys.J. **C73** (2013) 2304, arXiv:1112.6426 [hep-ex].

[103] J. Alwall, M. Herquet, F. Maltoni, O. Mattelaer, and T. Stelzer, *MadGraph 5 : Going Beyond*, JHEP **1106** (2011) 128, arXiv:1106.0522 [hep-ph].

[104] J. Alwall, S. Hoche, F. Krauss, N. Lavesson, L. Lonnblad, et al., *Comparative study of various algorithms for the merging of parton showers and matrix elements in hadronic collisions*, Eur. Phys. J. **C53** (2008) 473, arXiv:0706.2569 [hep-ph].

[105] G. Cowan, K. Cranmer, E. Gross, and O. Vitells, *Asymptotic formulae for likelihood-based tests of new physics*, Eur. Phys. J. **C71** (2011) 1554, arXiv:1007.1727 [physics.data-an].

[106] A. L. Read, *Presentation of search results: The CL(s) technique*, J. Phys. **G28** (2002) 2693–2704.

[107] C. Chen, M. Drees, and J. Gunion, *Addendum/erratum for 'searching for invisible and almost invisible particles at e^+e^- colliders' [hep-ph/9512230] and 'a nonstandard string/SUSY scenario and its phenomenological implications' [hep-ph/9607421]*, arXiv:hep-ph/9902309 [hep-ph].

[108] ATLAS Collaboration, *Search for squarks and gluinos with the ATLAS detector in final states with jets and missing transverse momentum and 20.3 fb^{-1} of*

$\sqrt{s} = 8$ *TeV proton-proton collision data*, tech. rep., CERN, 2013. ATLAS-CONF-2013-047.

[109] ATLAS Collaboration, *ATLAS Insertable B-Layer Technical Design Report*, tech. rep., CERN, Geneva, 2010. CERN-LHCC-2010-013.

Appendix A

Profile Likelihood and CL$_{\text{S}}$

A.1   Profile likelihood ratio

The profile likelihood ratio is used for the hypothesis test to determine the background and signal yields. In order to test a hypothesized value of μ, the profile likelihood ratio is defined by,

$$\lambda(\mu) = \frac{L(\mu, \hat{\hat{\theta}})}{L(\hat{\mu}, \hat{\theta})} \tag{A.1}$$

where L is the likelihood function that represents the probability for the measurement, and θ represents the parameters characterizing the shape of the probability density function. The quantity $\hat{\hat{\theta}}$ denotes the value of θ that maximizes L for specified μ, and the quantities $\hat{\mu}$ and $\hat{\theta}$ refer to the values that give the unconditional maximum of the likelihood.

For the purpose of establishing a one-sided upper limit, the test statistic is defined by

$$q_\mu = \begin{cases} -2\ln \lambda(\mu) & \text{for} \hat{\mu} \leq \mu, \\ 0 & \text{for} \hat{\mu} > \mu. \end{cases} \tag{A.2}$$

The ratio $\lambda(\mu)$ is expected to be close to unity if the observed data are in good agreement with the hypothesized value of μ.

To quantify the degree of agreement between the observed data and hypothesized μ, the p-value defined by

$$p = \int_{q_{\mu,\text{obs}}}^{\infty} f(q_\mu|\mu) dq_\mu, \tag{A.3}$$

is calculated, where $q_{\mu,\text{obs}}$ is the value of the statistic q_μ observed from the data and $f(q_\mu|\mu)$ is the probability density function (pdf) of q_μ.

In high energy physics, the p-value is often translated into an equivalent quantity called the significance, Z. The Z is defined such that a Gaussian distributed

1

variable found Z standard deviations above its mean has an upper-tail probability equal to the p-value. That is, the significance Z is related to the p-value by

$$p = \int_Z^\infty \frac{1}{\sqrt{2\pi}} e^{-x^2/2} dx = 1 - \Phi(Z),$$ (A.4)

where Φ is the cumulative standard Gaussian distribution.

The relation between the p-value and the observed q_μ and also the significance Z are shown in Fig. A.1. For the purpose of a discovery, a threshold p-value of 2.87×10^{-7} on the background-only hypothesis is used, which corresponds to Z = 5. For the purpose of excluding a signal hypothesis, a threshold p-value of 0.05 on the signal plus background hypothesis is used, which corresponds to Z = 1.64.
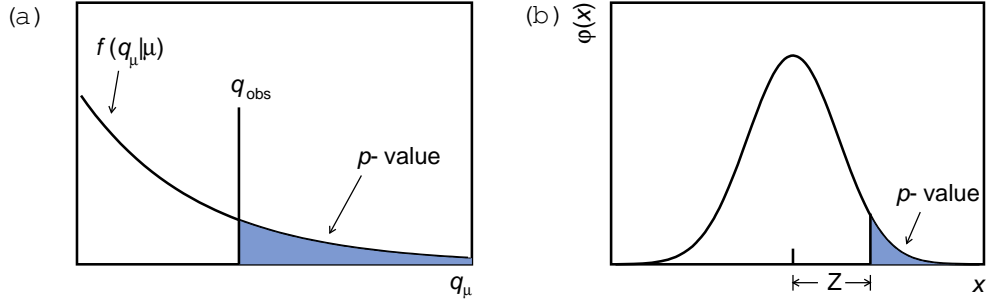A.1.

Figure A.1: (a) Illustration of the relation between the p-value obtained from an observed value of the test statistic q_μ. (b) The standard normal distribution $\phi(x) = (1/\sqrt{2\pi}) \exp(-x^2/2)$ showing the relation between the significance Z and the p-value.

A.2   Confidence level

In order to determine the statistical significance of the observation, CL$_{s+b}$ that is defined as the probability to obtain a result that is less compatible with the signal than the observed result assuming the signal hypothesis is used: i.e. CL$_{s+b}$ is calculated by

$$CL_{s+b} = \int_{q_{\mu,\text{obs}}}^\infty f(q_\mu|\mu) dq_\mu,$$ (A.5)

The signal model is regarded as excluded at a confidence level (CL) of $1-\alpha$ if CL$_{s+b} \leq \alpha$. However, if too few candidates are observed to account for the estimated background, any signal models and even the background itself might be excluded.

In order to solve this problem, the CL$_s$ method [106] is often used. In the CL$_s$ method, the signal plus background hypothesis is rejected if

$$CL_s \equiv \frac{CL_{s+b}}{1 - CL_b} = \frac{\int_{q_{\mu,\text{obs}}}^{\infty} f(q_\mu|\mu)dq_\mu}{\int_{q_{\mu,\text{obs}}}^{\infty} f(q_\mu|0)dq_\mu} \leq \alpha, \qquad (A.6)$$

where 1 - CL$_b$ is the probability to obtain a result that is less compatible with the background-only hypothesis than the observed result. A value of 95 % CL is commonly used to set an exclusion limit on signal models.